Spectral measurements and carcinogenic effects modeling of secondary neutrons in radiation therapy

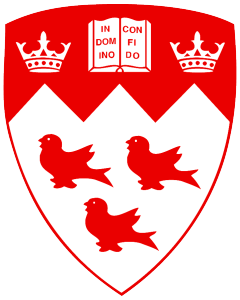

Logan Montgomery

Department of Physics
McGill University, Montreal
November 2021

A thesis submitted to McGill University in partial fulfillment of the requirements of the degree of
Doctor of Philosophy

Acknowledgements

This research would not have been possible without the guidance, expertise, and support of many extraordinary individuals.

I would first like to extend my utmost gratitude to my supervisor Dr. John Kildea. I have had the privilege of working as a member of John's research group, the NICE ROKS team, during both my MSc and PhD. John has been a genuine source of insight and inspiration throughout the entirety of my time as a graduate student and I owe him a great deal for shaping me into the scientist I am today.

I would also like to share my sincere appreciation for my co-supervisor Dr. Anthony Landry. Tony graciously stepped into this supervisory role when I relocated from Montreal to PEI early in my PhD. Since then, he has imparted upon me a trove of knowledge and anecdotes pertaining to science, lifestyle, and everything in between. I am truly fortunate to have received his wisdom.

My time as a member of the NICE ROKS team has been extremely formative in terms of both scholarly pursuits and friendships forged. Thank you Felix Mathew and Chris Lund for your camaraderie in establishing much of what the NICE team has become. I have found great comfort in our friendship over the years and will always look forward to our next encounter. Thank you Haley Patrick for learning and laughing alongside me the longest in our team and for your aid in keeping me connected while working remotely. Thank you Luc Galarneau for your expertise in the French translation of my abstract. And thank you to all of the other team members who have come and gone during my tenure; it was an absolute pleasure to work alongside you.

Similarly, my time as a graduate student in the McGill Medical Physics Unit was made enjoyable and enthralling by many individuals. Special thanks are owed to Marc-André Renaud and Judy Wang for their friendship and for hosting me on my many stays in Montreal. I would also like to thank my friend André Diamant for years of laughs and for answering many of my

questions about his experience preparing and submitting his thesis. Several other of my fellow students are owed special thanks for their companionship, so thank you Véronique Fortier, Joel Mullins, Gabriel Famulari, Hossein Naseri, Ackeem Joseph, and Ali Toltz. Additionally, the administrative efficiency and kindness of Margery Knewstubb and Tatjana Nisic must be recognized. Thank you both. Finally, to Dr. Jan Seuntjens, Dr. Shirin Enger, and Dr. Ives Levesque: thank you for fostering a culture of scientific repute, inclusivity, and fun in the MPU.

The fine folks of the PEI Cancer Treatment Centre must be acknowledged for warmly welcoming into their midst. Special shout out to Grant MacNevin, Cindy Tam, Eric Reynard, and especially Judy Hale for accommodating me onsite.

I would like to extend my appreciation to any individual who has contributed to any of the open-source software that I have used at any point during my research. Great science is built on the backs of individuals who take the extra step to document and share their work.

I owe my parents Debbie and Gary, as well as my brother Curtis, a lifetime of gratitude for all of their love, laughter, and support throughout my academic endeavours and elsewhere.

Finally, no amount of thanks is sufficient to express my gratitude for my wife Kathleen, who has intimately shared in all of the highs and lows along every step of this journey. Every moment shared with you is a treasure.

Abstract

During high-energy radiation therapy, patients are exposed to a spectrum of secondary neutrons that pose an iatrogenic cancer risk. This risk is qualitatively encapsulated by quantities such as the International Commission on Radiological Protection's neutron weighting factors. These factors convey neutron relative biological effectiveness (RBE) for inducing stochastic radiobiological effects and are characterized by a marked energy dependence. However, there is lack of direct evidence as to the biophysical mechanisms underlying this energy dependence.

The overall goal of this thesis was to advance our understanding of the carcinogenic risk posed by secondary neutrons to radiation therapy patients. This goal required knowledge of both the neutron spectra encountered in radiation therapy and how those spectra cause radiobiological effects. Therefore, two objectives were set:

1. Demonstrate the ability to accurately measure neutron spectra produced in clinically-relevant scenarios.

2. Develop a Monte Carlo model to investigate the biophysical mechanisms underlying the energy dependence of neutron RBE for stochastic effects.

Two studies were conducted pertaining to objective #1. In the first study, a Nested Neutron Spectrometer (NNS) was used to measure and compare the neutron spectra produced by a 10 MV flattening-filter-free (FFF) beam and a conventional, flattened 10 MV beam. It was found that the FFF beam reduced the neutron fluence by 30-40% per monitor unit (MU) without appreciable change to the spectral shape. The primary cause of this reduction was found to be a decrease in the number of electrons striking the linac bremsstrahlung target per MU, rather than the removal of a source of neutrons in the flattening filter itself.

The second study was designed to address a lack of objectivity in the process of unfolding raw NNS measurements into neutron spectra. The maximum-likelihood expectation–maximization (MLEM) algorithm that is used to unfold NNS measurements is an iterative

process that requires a stopping criterion. Previously, the MLEM algorithm was terminated after a fixed number of iterations based on subjective user input, resulting in both intra-user and inter-user variations. In this study, an objective stopping criterion was developed that terminates unfolding at an optimal number of iterations without user input.

Finally, a third study was conducted with regards to objective #2. The propensity of radiation to induce clusters of DNA damage is widely believed to be the primary initiating event for radiation-induced mutagenesis and subsequent carcinogenesis because clustered lesions are difficult to repair and rarely occur endogenously. Thus, a Monte Carlo application was developed to simulate the irradiation of nuclear DNA and score the resulting yields of clustered DNA damage. Simulations were performed for neutron energies between 1 and 10 MeV and a reference 250 keV x-ray radiation. The resulting neutron RBE for inducing clustered DNA damage exhibited qualitatively similar energy dependence to the published neutron weighting factors. This result was robust to a variety of simulation parameters, including low dose irradiation, and thus provides fundamental biophysical evidence towards explaining the energy dependence of neutron RBE for inducing stochastic radiobiological effects.

The spectral measurements and Monte Carlo modeling described in this body of work represent marked advancements towards understanding and characterizing the relative carcinogenic risk posed by secondary neutrons to radiation therapy patients. This research was conducted in the spirit of open science and, as such, the unfolding algorithm and Monte Carlo application developed in this work were released under open-source licenses.

Résumé

Au cours des traitements de radiothérapie à haute énergie, les patients sont exposés à un spectre de neutrons secondaires qui présentent un risque de cancer iatrogène. Ce risque est défini par des quantités comme les facteurs de pondération des neutrons publié par la commission internationale de protection radiologique (ICRP). Ces quantités décrivent l'efficacité biologique relative (EBR) des neutrons provoquant des effets stochastiques et sont caractérisées par une dépendance énergétique. Cependant, les évidences manquent pour expliquer les mécanismes biophysiques sous-jacent de cette dépendance énergétique.

Le but de cette thèse était de faire progresser notre compréhension du risque cancérigène posé par les neutrons pour les patients en radiothérapie. Ce but demande des connaissances du spectre des neutrons rencontrés en radiothérapie et comment ces spectres causent les effets radiobiologiques. Ainsi, deux objectifs ont été fixés.

1. Démontrer notre capacité à mesurer les spectres de neutrons qui sont produits dans des scénarios pertinents en clinique de radiothérapie.

2. Développer des simulations de Monte Carlo pour étudier les mécanismes biophysiques sous-jacents la dépendance énergétique de l'EBR des neutrons pour les effets stochastiques.

Deux études ont été menées concernant le premier objectif. Dans la première étude, le Nested Neutron Spectrometer (NNS) a été utilisé pour comparer les spectre de neutrons produits par un faisceau de radiothérapie de 10 MV sans filtre égalisateur (FFF) et par un faisceau conventionnel de 10 MV. Nous avons observé que le faisceau FFF réduit la fluence de neutrons de 30 à 40% par unité moniteur (UM) sans modifier de manière significative la forme spectrale. La principale cause de cette réduction est la diminution du nombre d'électrons incidents sur la cible de bremsstrahlung du linac par UM.

La deuxième étude a été conçue pour aborder la subjectivité dans le processus de déploiement des mesures NNS en spectres neutroniques. L'algorithme vraisemblance maximale

d'espérance-maximisation VMEM que nous utilisons pour déconvoluer les mesures NNS est un processus itératif qui nécessite un critère d'arrêt. Dans le passé, nous arrêtions l'algorithme VMEM après un nombre fixe d'itérations en fonction de l'avis subjectif de l'utilisateur, ce qui entraînait un manque de reproductibilité. Dans la présente étude, nous avons mis au point un critère d'arrêt objectif qui met fin au déploiement après un nombre optimal d'itérations et qui ne nécessite pas l'intervention subjective de l'utilisateur.

Enfin, une troisième étude a été menée pour atteindre notre deuxième objectif. On pense généralement que les dommages groupés à l'ADN causés par les rayonnements sont des précurseurs de la mutagenèse et de la cancérogenèse, car ils sont difficiles à réparer et se produisent rarement de façon endogène. Nous avons donc développé une application de Monte Carlo pour simuler l'irradiation de l'ADN nucléaire et analysé les rendements des dommages groupés à l'ADN induits par les rayonnements. Nous avons effectués des simulations avec des neutrons ayant des énergies multiples entre 1 et 10 MeV ainsi que des photons de 250 keV pour. Nous avons observé que l'EBR des neutrons pour l'induction de dommages groupés à l'ADN présentait une dépendance énergétique qualitativement similaire aux facteurs de pondération des neutrons de la ICRP. Ce résultat s'est montré robuste pour une variété de paramètres de simulation et a donc fourni des preuves biophysiques fondamentales expliquant la dépendance énergétique de l'EBR des neutrons induisant des effets stochastiques.

Les études décrites dans cette thèse constituent une avancée significative dans la caractérisation du risque cancérigène relatif posé par les neutrons secondaires aux patients en radiothérapie. Nous reconnaissons l'importance du mouvement de la science ouverte et avons donc publié notre algorithme MLEM et notre application Monte Carlo sous des licences code source ouvertes.

Contents

List of Figures

List of Tables

List of Abbreviations

ALARA	As Low As Reasonably Achievable
AP Site	Apurinic or Apyrimidinic Site
BEIR	Committee on the Biological Effects of Ionizing Radiation
BER	Base Excision Repair
BP	DNA Base Pair
BSS	Bonner Sphere Spectrometer
CCS	Canadian Cancer Society
CHMC	Condensed-History Monte Carlo
CPD	Cumulative Probability Distribution Function
CPS	Counts Per Second
DNA	Deoxyribonucleic Acid
DSB	Double Strand Break
EBRT	External Beam Radiation Therapy
FFF	Flattening-Filter-Free
Geant4	Geometry And Tracking 4
HDPE	High-Density Polyethylene
HGP	Human Genome Project

HRR	Homologous Recombination Repair
ICRP	International Commission on Radiological Protection
IMRT	Intensity-Modulated Radiation Therapy
LET	Linear Energy Transfer
LNT	Linear Non-Threshold
LSS	Life Span Study
MC	Monte Carlo
MD	Mean Deviation
MLC	Multileaf Collimator
MLEM	Maximum-Likelihood Expectation–Maximization
MSD	Mean Square Deviation
MU	Monitor Unit
NHEJ	Non-Homologous End Joining
NNS	Nested Neutron Spectrometer
NTE	Non-Targeted Effect
OARs	Organs At Risk
PDF	Probability Distribution Function
PET	Positron Emission Tomography
RBE	Relative Biological Effectiveness
RER	Radiation Effects Ratio
RF	Radiofrequency
RIBE	Radiation-Induced Bystander Effects

RIGI	Radiation-Induced Genomic Instability
RMSE	Root Mean Square Error
RNG	Random Number Generator
SB	Strand Break
SSB	Single Strand Break
TOPAS	Tool For Particle Simulation
TSMC	Track-Structure Monte Carlo
US NRC	United States Nuclear Regulatory Commission
VRT	Variance Reduction Technique

Preface

Contributions to original knowledge

This thesis contains three original manuscripts, two of which are published and one that has been submitted to a journal. Each manuscript constitutes an original contribution to the field that may be summarized as:

1. An experimental investigation of the relative photoneutron production by 10 MV and 10 MV FFF (flattening-filter-free) beams using the Nested Neutron Spectrometer (NNS).

2. The development of a novel stopping criterion that is applied when unfolding NNS measurements with the iterative Maximum-Likelihood Expectation–Maximization (MLEM) algorithm.

3. A computational investigation of neutron relative biological effectiveness (RBE) for the direct induction of clustered DNA damage in order to model the energy dependence of neutron RBE for stochastic effects.

Author contributions

Chapters 1-3, 6, 7, and 9 comprise the introduction, theory, and conclusion of this thesis. I was the sole author of these chapters and they were edited by John Kildea and Anthony Landry. Luc Galarneau edited the French translation of the abstract. The author contributions for the original manuscripts contained in Chapters 4, 5, and 8 are summarized as follows:

1. Chapter 4: *Logan Montgomery, Michael Evans, Liheng Liang, Robert Maglieri, and John Kildea. The effect of the flattening filter on photoneutron production at 10 MV in the Varian TrueBeam linear accelerator. Medical Physics, 45(10):4711-4719, 2018.*

This study was designed by John Kildea and I. I acquired the measurements with the NNS, processed the data using MLEM, analyzed the data, and wrote the manuscript. Michael Evans and Liheng Liang provided clinical expertise in the measurement process. Robert Maglieri conducted much of the foundational work upon which this study was based. John Kildea provided guidance on all aspects of the study. All authors reviewed the manuscript.

2. Chapter 5: *Logan Montgomery, Anthony Landry, Georges Al Makdessi, Felix Mathew, and John Kildea. A novel MLEM stopping criterion for unfolding neutron fluence spectra in radiation therapy. Nuclear Instruments and Methods in Physics Research Section A: Accelerators, Spectrometers, Detectors and Associated Equipment, 957:163400, 2020.*
   This study was designed by John Kildea and I. I designed and developed the novel stopping criterion, acquired some of the measured data, processed the data using MLEM, analyzed the data, and wrote the manuscript. Anthony Landry provided guidance on all aspects of the study. Georges Al Makdessi coded a C++ prototype of the core MLEM algorithm on which our novel implementation was based. Felix Mathew acquired some of the measured data. John Kildea provided guidance on all aspects of the study. All authors reviewed the manuscript.

3. Chapter 8: *Logan Montgomery, Chritopher M Lund, Anthony Landry, and John Kildea. Towards the characterization of neutron carcinogenesis through direct action simulations of clustered DNA damage. Submitted to Physics in Medicine and Biology, July 2021.*
   This study was designed by John Kildea and I. I developed the novel track-structure Monte Carlo application used to conduct the study, ran the simulations, processed the data using Python, analyzed the data, and wrote the manuscript. Christopher M Lund previously developed and ran simulations to generate the secondary particle data that we input into my simulations and provided expert insight on the data analysis. Anthony Landry and John Kildea provided guidance on all aspects of the study. All authors reviewed the manuscript.

Chapter 1

Introduction

1.1 Cancer

Cancer refers to a diverse class of diseases that can arise anywhere in the body and in humans of all ages. Although cancer manifests itself in many forms, its physiology is characterized by many distinct features known as the "hallmarks of cancer" [1, 2]. These hallmark features give rise to malignant cancer cells that proliferate uncontrollably, can metastasize (i.e. spread to other parts of the body), and ultimately act to disrupt healthy bodily functions. For many types of cancer, the accumulation of cancer cells and associated physiological features (such as dedicated vasculature) results in a solid mass called a tumour.

Cancer is responsible for the death of approximately 30% of all Canadians, making it the leading cause of death in Canada [3]. The Canadian Cancer Society (CCS) projected there would be 225,800 new cancer cases and 83,300 cancer deaths in Canada in 2020. Fortunately, the mortality rates associated with cancer are declining. The current estimate based on data from 2012 to 2014, suggests that the five-year survival rate among Canadians diagnosed with all types of cancer is approximately 63% [3]. This result is up from 55% in the early 1990s and from 25% in the 1940s [3]. These improvements in cancer survival rates are attributed to both the earlier detection and diagnosis of cancer as well as advancements in treatment techniques [4].

There are many cancer treatment modalities, which reflects the diversity in both the disease itself and the individuals in which the disease presents. Systemic therapies such as chemotherapy and hormonal therapy act on the entire body, whereas localized therapies like surgery and radiation therapy are confined to a limited area of the body around the disease [5]. These

four modalities are the most commonly used in cancer treatment. Chemotherapy involves the use of drugs that traverse the bloodstream and preferentially attack rapidly-dividing cells like cancer cells. Hormonal therapy encompasses various treatments designed to impact hormone production in order to obstruct the development of cancers that require these hormones. Surgery is used to resect a cancerous tumour and nearby tissue that may contain microscopic disease. Finally, radiation therapy involves the use of ionizing radiation to kill cancer cells in a targeted manner.

This thesis, and the studies contained herein, focus on radiation therapy. The remainder of this chapter presents a broad discussion on radiation therapy as a cancer treatment modality and builds towards a discussion of the challenges associated with secondary neutron radiation produced during high-energy ($\gtrsim 8$ MeV) radiation therapy. The chapter concludes with a summary of the motivation and objectives of this work, as well as an overview of the remaining chapters of this thesis.

1.2 Radiation therapy

It is estimated that radiation therapy is medically indicated for approximately 50% of cancer patients [6]. Radiation therapy may be used concurrently with another form of treatment, as part of a sequence of treatments, or on its own. If the intent of radiation therapy is to completely eradicate the disease, it is said to be curative. Otherwise, radiation therapy may be used to palliate symptoms of the disease, such as pain, in order to improve a terminal patient's quality of life.

Radiation therapy involves the use of ionizing radiation, which is any form of radiation with sufficiently high energy to ionize atoms and molecules in an absorbing medium [7]. Charged particles like electrons and protons are said to be directly ionizing radiation because they directly deposit their energy in the absorber via Coulomb interactions. Neutral particles like photons and neutrons, however, are considered indirectly ionizing radiation because they must first transfer their energy to charged particles that subsequently deposit their energy in the absorber. All of these types of ionizing radiation are encountered in radiation therapy.

The purpose of radiation therapy is to use ionizing radiation to selectively damage and kill cancer cells. This is achieved by delivering a large amount of radiation, quantified using a concept called absorbed dose (Section 2.4.3), to the site of the disease (i.e. the target volume).

However, the fundamental challenge associated with radiation therapy is that radiation can also cause biological damage to the healthy tissue surrounding the disease.

The biological effects of radiation are classified as deterministic or stochastic depending on the number of cells that are damaged and thus on the dose of the exposure [8]. Deterministic effects are characterized by a relatively large threshold dose, below which the probability of occurrence is 0% and above which the probability rapidly increases to 100%. For example, acute radiation syndrome occurs if the whole body receives more than a few gray of dose, whereas organ-specific toxicities like xerostomia or pneumonitis occur when specific organs are exposed to a dose above a particular threshold. An additional characteristic of deterministic effects is that their severity increases with dose above the threshold.

Stochastic effects, such as carcinogenesis and other genetic effects, are considered late effects because they may not physically manifest for a long time after exposure. These stochastic effects are not associated with a threshold dose and do not increase in severity with increasing dose. Rather, the probability of stochastic effects increases with increasing dose. In terms of radiation protection, it is conservatively assumed that even damage to a single cell from a low dose of radiation can result in a stochastic effect [8]. This is the underlying motivation for the radiation protection paradigm to keep radiation exposure to healthy tissues As Low as Reasonably Achievable (ALARA).

In consideration of the potential for adverse biological effects, the objectives of radiation therapy are thus (i) to deliver a sufficiently high dose to the target volume and (ii) to minimize the dose to healthy tissues (i.e. nontarget dose). A sophisticated workflow has evolved in radiation therapy in order to achieve these two incongruous objectives, which is summarized in Figure 1.1. The workflow begins by acquiring medical images of the relevant internal patient anatomy while the patient is positioned in the same position that they will be in during treatment. This treatment simulation process is typically performed using a CT simulator. The target volume and organs at risk (OARs) near the target are then delineated on the acquired images in a process known as contouring. Next, the contoured images are used to develop a radiation treatment plan, typically using software that models the delivery of radiation to the patient's body by means of a radiation emitting device. This treatment planning step usually involves an optimization process to develop a plan that optimally satisfies the treatment objectives. The patient is then setup for treatment and imaged in order to verify and align their current position with respect to their reference position at the time of simulation. Finally, the patient is treated by delivering the treatment as planned.

Figure 1.1 Overview of the radiation therapy workflow.

There are many different treatment delivery techniques applied in radiation therapy. The two categories of treatment that are utilized for most radiation therapy patients are external beam radiation therapy (EBRT) and brachytherapy. With EBRT, the patient is treated using one or more beams of radiation produced by a radiation source external to the body. In brachytherapy, one or more radioactive sources are inserted into the body in close proximity to the target either permanently or for a short duration. EBRT typically delivers a larger nontarget dose than brachytherapy because the radiation beam must pass through healthy tissue both before and after reaching the target. Brachytherapy, however, is an invasive medical procedure that requires considerably more time and personnel to deliver. This thesis is primarily concerned with EBRT owing to the fact that neutron production only becomes relevant at radiation energies exceeding $\sim$8 MeV [7], which is predominantly the domain of EBRT.

1.3 External beam radiation therapy

In the past, EBRT beams were typically produced by a naturally radioactive source such as ^{60}Co. Nowadays, the majority of EBRT treatments are delivered using one or more beams of radiation generated by a particle accelerator. The most common particle accelerator used in EBRT is the medical linear accelerator (linac), which is depicted schematically in Figure 1.2. The process of generating a high-energy radiation beam with a linac begins with an electron gun that emits low-energy electrons from a heated cathode [9]. These electrons are passed through a waveguide that accelerates the electrons to high energies ($\sim$ MeV) using high power radiofrequency (RF) fields. The resulting high energy electrons are transported to the linac treatment head wherein a viable clinical beam of radiation is generated.

Most linacs are capable of generating either photon beams or electron beams. To generate a photon beam, the high energy electrons are directed onto a metallic bremsstrahlung target in which the electrons interact and generate a broad photon beam (the bremsstrahlung process

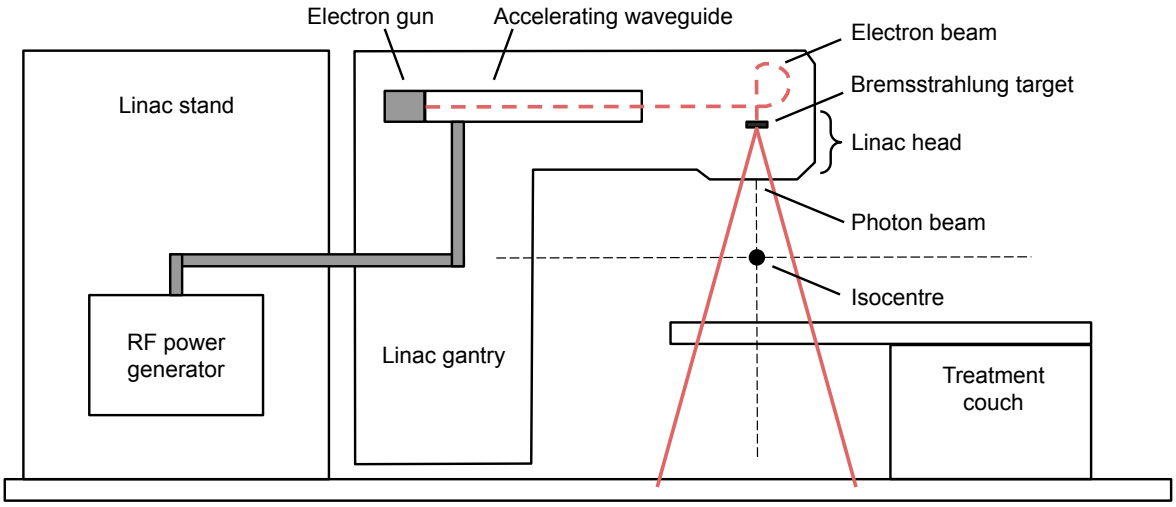

Figure 1.2 Simplified schematic of a medical linear accelerator (linac). Figure adapted from Podgoršak [9].

is described in Section 2.1.2). A variety of metallic components called collimators are then used to reshape the beam profile to the desired shape and fluence. First, the primary collimator establishes a circular radiation field. The profile of the beam is then made uniform (i.e. flattened) using a flattening filter in order to facilitate accurate dose calculations in the treatment planning process. The rectangular size and shape of the beam (i.e. the treatment field) are then defined by using two large sets of orthogonal jaws. Finally, the shape of the beam is fine-tuned using a multileaf collimator (MLC) that is comprised of a motorized array of small, metallic "leaves" before exiting through the field opening. To generate an electron beam, the bremsstrahlung target is removed from the beam path and the flattening filter is replaced with a scattering foil that converts the incoming narrow electron beam into a broad beam. Additionally, the MLC is replaced by a cutout collimator placed in close proximity to the patient. A schematic of the linac treatment head components that are used to generate a photon beam is shown in Figure 1.3.

Linacs are typically able to generate beams with several different energy profiles by varying the frequency of the RF fields in the waveguide. A typical range of electron energies that can be produced by a linac spans from 4 to 25 MeV. Nominally, electron beams are denoted by the maximum energy in the beam (e.g. an 18 MeV beam) but they always contain a spectrum of energies due to the scattering foil and collimators. This is similarly true for photon beams,

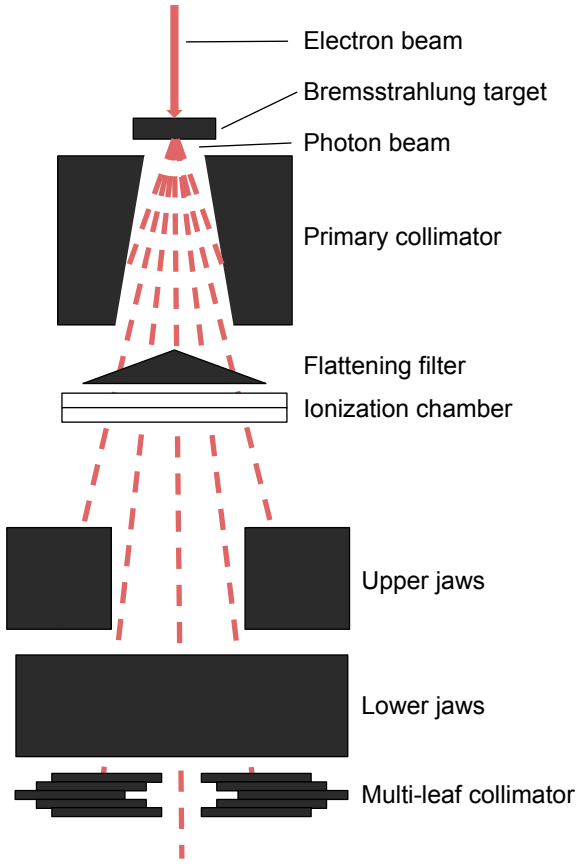

Figure 1.3 Simplified schematic of the head of medical linear accelerator.

although they are denoted as megavoltage beams (e.g. an 18 MV beam) to reflect the underlying bremsstrahlung spectrum.

The linac gantry is connected to a ring to enable 360° rotation around the patient. The geometric point at which the axis of gantry rotation intersects with the axis of the beam is called the isocentre. In a typical treatment the target volume is placed at isocentre and multiple radiation beams are delivered from a variety of gantry angles. The shape of the beam is adjusted at each gantry angle by adjusting the position of the jaws and MLC leaves in order to match the projection of the target. This multi-angled delivery allows the nontarget dose to be spread over the body and thereby avoid delivering a particularly high dose to any one region of healthy tissue.

It is instructive to consider two distinct categories of nontarget dose: (i) in-field nontarget dose and (ii) out-of-field nontarget dose [10]. In-field nontarget dose is the dose to healthy tissue that lies within the treatment field, i.e. within the path of the beam. Out-of-field nontarget dose is the dose to healthy tissue that does not lie within the treatment field.

Technological advancements like the ability to rotate the linac gantry and produce highly collimated radiation beams have enabled significant reductions in the in-field nontarget dose for modern radiation therapy treatments [10]. This improved treatment conformality has made it easier to achieve the treatment objectives of delivering sufficiently high dose to the target volume while minimizing OAR toxicities. However, these advancements have done little to address the issue of out-of-field nontarget dose. In fact, the increased beam modulation associated with modern intensity-modulated radiation therapy (IMRT) techniques leads to an increase in head leakage and out-of-field nontarget dose.

1.4 Secondary radiation

Out-of-field nontarget dose to the patient from linac-based EBRT is caused by the following three sources of non-therapeutic "secondary" radiation [10].

1. Leakage radiation: radiation originating in the treatment head that penetrates through the linac shielding.

2. Collimator scatter: radiation that exits the linac via the field opening but does not fall within the treatment field.

3. Patient scatter: radiation from the primary beam that scatters out of the treatment field from inside the patient.

Staff and the general public are shielded from secondary (and primary) radiation by installing linacs in specialized treatment rooms called bunkers. Bunkers are generally constructed from thick concrete walls known as barriers that attenuate the primary and secondary radiation produced during radiation therapy to safe levels. A radiation therapy bunker also often includes a specially-designed corridor called a maze that connects the treatment room to the console area where the linac is remotely operated by staff. This maze serves to reduce the levels of secondary radiation without requiring a massive door to attenuate the secondary radiation. A schematic of the layout of a typical radiation therapy bunker is shown in Figure 1.4.

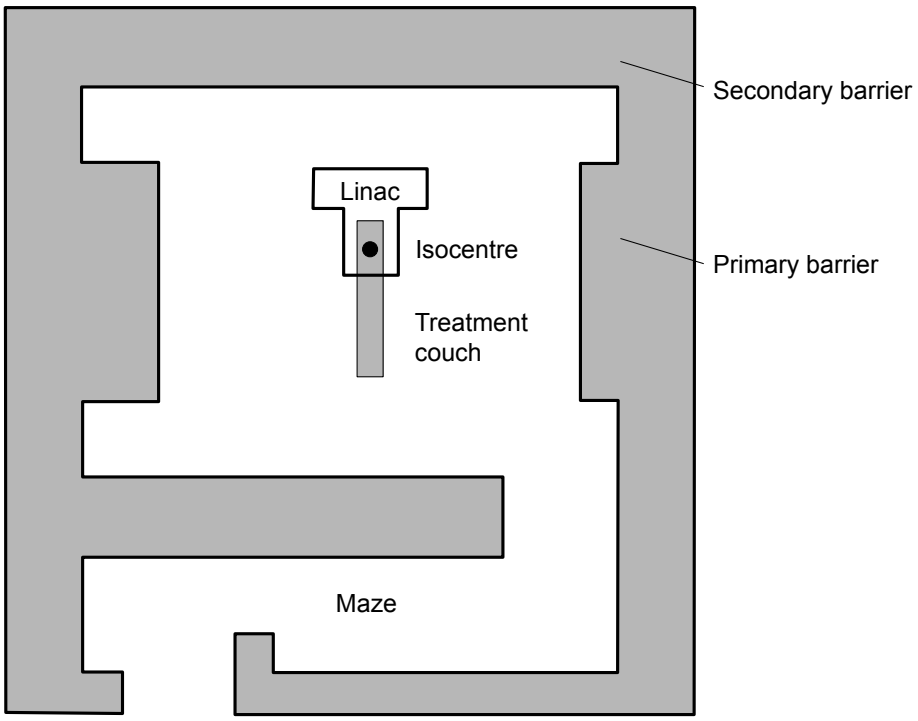

Figure 1.4 Overhead schematic of a radiation therapy bunker.

Unfortunately, radiation therapy bunkers do not shield the patient from secondary radiation. The out-of-field nontarget dose delivered to the patient is typically on the order of 0.01–1% of the target dose and is dependent on the distance from the treatment field [10]. The amount of secondary radiation reaching the patient varies considerably with treatment technique, beam type, beam energy, and many other factors.

The out-of-field nontarget dose poses a concern for a variety of undesirable effects. Some of these effects are deterministic effects with low threshold doses, such as cardiac toxicities and cataractogenesis [10]. The focus of this thesis, however, is on the risk for stochastic effects such as carcinogenesis. Historically, the risk of a patient developing a second cancer later in life as a result of their radiation therapy treatment has been of relatively low importance compared to achieving the primary treatment objectives. However, this risk is becoming increasingly important because, as previously mentioned, cancer patients are living longer post-treatment [3, 10]. This iatrogenic carcinogenic risk is of particular concern for paediatric patients.

1.5 Secondary neutrons

When the maximum energy of the primary beam exceeds ∼8 MeV, photonuclear and electronuclear reactions between the beam and the components of the linac head result in the generation of high energy (i.e. fast) neutrons. Neutrons are a highly penetrating form of ionizing radiation and because many of them are able to escape the linac head, they comprise an important component of the leakage radiation. The spectrum of neutrons to which the patient is exposed is characterized by the following features [11–13]:

1. A fast neutron peak centred around 1 MeV that results from photoneutron production in the head of the linac.

2. A thermal neutron peak centred around 0.025 eV that results from thermalization of fast neutrons by the linac, patient, bunker walls, and treatment room furnishings.

3. An intermediate energy tail that connects these two peaks and comprises neutrons produced at lower energies in the linac via compound nucleus formation, as well as faster neutrons that have been slowed down but not yet thermalized.

Figure 1.5 shows an example of a photoneutron fluence spectrum produced by the 10 MV beam of a Varian TrueBeam linac at 100 cm from isocentre on the treatment couch.

There are two unique challenges pertaining to the secondary neutrons produced in radiation therapy:

- **Challenge #1**: The carcinogenic risk associated with neutrons is both energy-dependent and larger in magnitude than most other forms of ionizing radiation.

- **Challenge #2**: Detecting neutrons with a wide range of energies is challenging and requires specialized devices called neutron spectrometers.

The remainder of this section expands on these challenges and broadly describes how our research group aims to mitigate them. The specific objectives of this thesis research that were designed within the context of the goals of our research group are presented in the following section.

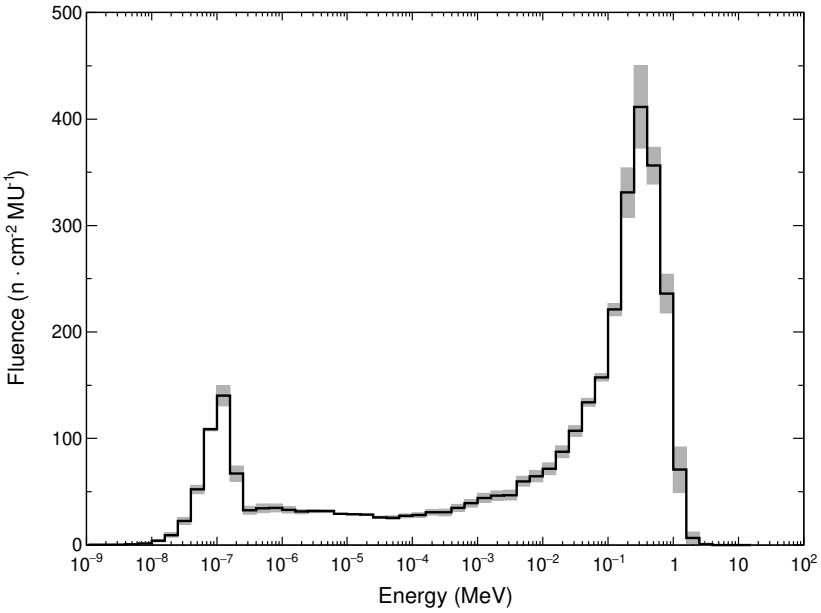

Figure 1.5 Neutron fluence spectrum produced by the 10 MV beam of a Varian TrueBeam linac at 100 cm from isocentre (away from the gantry). The plotted fluence is normalized per monitor unit (MU) of dose delivered.

1.5.1 Challenge #1 - Neutron carcinogenic risk

The energy dependence of neutron relative biological effectiveness (RBE) for stochastic effects is currently encapsulated by both (i) the neutron weighting factors published by the International Commission on Radiological Protection (ICRP) [14] and (ii) the neutron quality factors published by the United States Nuclear Regulatory Commission (US NRC) [15]. These factors are plotted as a function of neutron energy in Figure 1.6. Both factors exhibit a marked energy dependence with a peak value around 1 MeV, which coincides with the fast peak in the neutron fluence spectrum experienced by patients. Thus, secondary neutrons pose a prominent concern for second iatrogenic cancers caused by high energy radiation therapy.

The neutron weighting factors and neutron quality factors are based on aggregate RBE data for a variety of stochastic radiobiological endpoints in animals. As shown in Figure 1.6, there are substantial quantitative differences between these factors. These discrepancies highlight the need for a fundamental model that explains the marked energy dependence of neutron RBE for stochastic effects. Our research group aims to develop such a model by using Monte

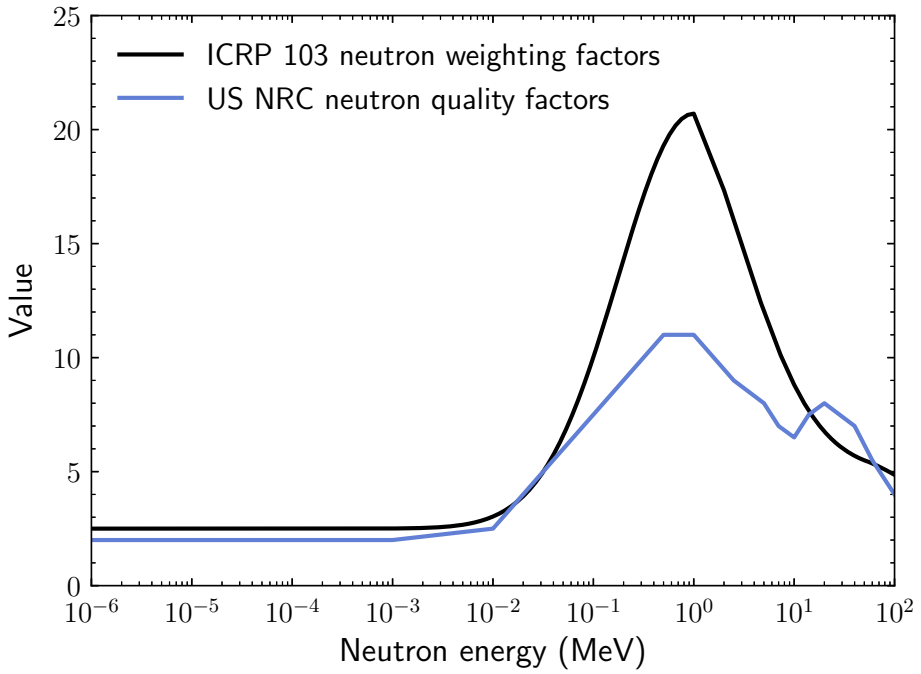

Figure 1.6 Quantities used to describe neutron relative biological effectiveness for inducing stochastic biological effects [14, 15].

Carlo methods to simulate how neutrons and their secondary particles interact with and damage nuclear DNA.

1.5.2 Challenge #2 - Neutron spectra

Due to the marked energy dependence of neutron RBE, accurate determination of the neutron fluence spectrum produced by any radiation therapy treatment is required in order to assess the associated neutron-induced carcinogenic risk. Measuring neutron spectra requires specialized detectors called neutron spectrometers because of the unique ways by which neutrons interact with matter. Conventional neutron spectrometers like the Bonner Sphere Spectrometer [16], which often incorporate a passive neutron detector, are an effective albeit slow and cumbersome means of measuring neutron spectra. Our research group has recently validated a novel, active neutron spectrometer called the Nested Neutron Spectrometer (NNS) [17] for use in radiation

therapy [13, 18]. An ongoing objective in our research group is to use the NNS to characterize neutron fluence spectra for a variety of clinically-relevant scenarios.

The raw measurements obtained with a neutron spectrometer also present a challenge as they must be unfolded in order to obtain the underlying neutron fluence spectrum. This unfolding process is prone to many sources of uncertainty and subjectivity [19]. Thus, our research group is also interested in developing unfolding techniques that diminish these challenges.

1.6 Thesis goal and objectives

In consideration of the aforementioned challenges pertaining to secondary neutrons in radiation therapy and the broad goals of our research group, the overall goal of this thesis is stated as follows:

To advance our understanding of the carcinogenic risk that is posed to radiation therapy patients by secondary neutrons through the measurement of neutron spectra and the development of a model to explain the energy dependence of their carcinogenic effects.

The following specific objectives were set in order to achieve this goal:

1. Use the NNS to accurately measure and compare neutron spectra produced in clinically-relevant radiation therapy scenarios.
    (a) Perform a case study using the NNS to measure and compare the neutron fluence spectra produced by modern flattening-filter-free (FFF) beams compared to conventional flattened beams.
    (b) Develop an objective algorithm for unfolding NNS measurements that does not require subjective user input.
2. Model the energy dependence of neutron RBE for stochastic effects by using Monte Carlo methods to simulate neutron-induced clustered DNA damage as a function of energy.

To complement these scientific objectives, an additional objective was to support and contribute to the open science movement through the development of open-source software. Many aspects of this thesis research benefited from access to a variety of open-source software that was either used or built upon. In other cases, however, progress was impeded by a lack of available software. It was thus crucial to provide the software tools that were developed in the

course of conducting this research to the community under open-source licenses. In doing so, other researchers are enabled to independently validate this research, and to expand upon it.

1.7 Thesis outline

This thesis is divided into two parts to reflect the distinct nature of the objectives.

Part I contains the theory and original manuscripts pertaining to objective #1 and is titled: "On the measurement of neutron spectra in radiation therapy". Part I begins with Chapter 2, which contains an overview of radiation interactions as well as relevant physical and dosimetric concepts, with the focus on neutrons. Chapter 3 summarizes the principles of detecting neutrons, presents the most relevant neutron spectrometers, and concludes with a review of published neutron spectral investigations in radiation therapy. Chapter 4 is a published manuscript that describes a case study using the NNS to compare neutron spectra produced by clinically commissioned FFF and conventional flattened beams. Finally, Chapter 5 is another published manuscript that details a novel algorithm for unfolding NNS measurements in an objective manner.

Part II contains the theory and an original manuscript pertaining to objective #2 and is titled: "Using Monte Carlo methods to model the energy dependence of neutron RBE for stochastic effects". Part II starts with Chapter 6 that provides an overview of radiation carcinogenesis with an emphasis on the means by which radiation-induced clustered DNA damage can lead to mutagenesis and subsequent carcinogenesis. Chapter 7 presents an introduction to the principles of Monte Carlo methods as applied to radiation transport, highlights the difference between condensed-history and track-structure techniques, and concludes with a review of published Monte Carlo investigations of neutron RBE. Chapter 8 is the aforementioned submitted manuscript that describes a Monte Carlo study to determine neutron RBE for the direct induction of clustered DNA damage and compares the results with neutron RBE for stochastic effects. Finally, Chapter 9 provides a summary of the thesis and concludes with an outlook for future work.

References

[1] D. Hanahan and R. A. Weinberg. The Hallmarks of Cancer. *Cell*, 100:57–70, 2000. 10.1016/S0092-8674(00)81683-9.

[2] D. Hanahan and R. A. Weinberg. Hallmarks of cancer: The next generation. *Cell*, 144(5): 646–674, 2011. 10.1016/j.cell.2011.02.013.

[3] Canadian Cancer Society. Cancer statistics at a glance, 2020. https://action.cancer.ca/en/research/cancer-statistics/cancer-statistics-at-a-glance.

[4] H. Ritchie. Cancer death rates are falling; five-year survival rates are rising, 2019. https://ourworldindata.org/cancer-death-rates-are-falling-five-year-survival-rates-are-rising.

[5] American Cancer Society. Cancer Treatment & Survivorship Facts & Figures 2019-2021. Technical report, American Cancer Society, Atlanta, 2019.

[6] M. B. Barton, et al. Estimating the demand for radiotherapy from the evidence: A review of changes from 2003 to 2012. *Radiotherapy and Oncology*, 112(1):140–144, 2014. 10.1016/j.radonc.2014.03.024.

[7] E. B. Podgoršak. *Radiation Physics for Medical Physicists*. Springer International Publishing Switzerland, Swizterland, third edition, 2016.

[8] E. J. Hall and A. J. Giaccia. *Radiobiology for the radiologist: Seventh edition*. Lippincott Williams & Wilkins, Philadelphia, seventh edition, 2012.

[9] E. B. Podgoršak. Treatment Machines for External Beam Radiotherapy. In E. B. Podgoršak, editor, *Radiation Oncology Physics: A Handbook for Teachers and Students*, chapter 5, pages 123–160. Vienna, 2005.

[10] S. F. Kry, et al. AAPM TG 158: Measurement and calculation of doses outside the treated volume from external-beam radiation therapy. *Medical Physics*, 44(10):e391–e429, 2017. 10.1002/mp.12462.

[11] D. J. Thomas, A. G. Bardell, and E. M. Macaulay. Characterisation of a gold foil-based Bonner sphere set and measurements of neutron spectra at a medical accelerator. *Nuclear Instruments and Methods in Physics Research, Section A: Accelerators, Spectrometers, Detectors and Associated Equipment*, 476(1-2):31–35, 2002. 10.1016/S0168-9002(01)01384-5.

[12] R. M. Howell, S. F. Kry, E. Burgett, N. E. Hertel, and D. S. Followill. Secondary neutron spectra from modern Varian, Siemens, and Elekta linacs with multileaf collimators. *Medical Physics*, 36(9):4027–4038, 2009. 10.1118/1.3159300.

[13] R. Maglieri, A. Licea, M. Evans, J. Seuntjens, and J. Kildea. Measuring neutron spectra in radiotherapy using the nested neutron spectrometer. *Medical Physics*, 42(11):6162–6169, 2015. 10.1118/1.4931963.

[14] ICRP. ICRP 103: The 2007 Recommendations of the ICRP. *Annals of the ICRP*, 37(2-4), 2007.

[15] US NRC. Units of Radiation Dose. *Code of Federal Regulations*, 10(20.1004):298–300, 2021.

[16] R. L. Bramblett, R. I. Ewing, and T. W. Bonner. A new type of neutron spectrometer. *Nuclear Instruments and Methods*, 9(1):1–12, 1960. 10.1016/0029-554X(60)90043-4.

[17] J. Dubeau, S. S. Hakmana Witharana, J. Atanackovic, A. Yonkeu, and J. P. Archambault. A neutron spectrometer using nested moderators. *Radiation Protection Dosimetry*, 150(2): 217–222, 2012. 10.1093/rpd/ncr381.

[18] F. Mathew, C. Chilian, L. Montgomery, and J. Kildea. Development of a passive gold-foil Nested Neutron Spectrometer to validate the active current-mode He-3 measurements in a high neutron fluence rate radiotherapy environment. *Nuclear Instruments and Methods in Physics Research, Section A: Accelerators, Spectrometers, Detectors and Associated Equipment*, 985:164662, 2021. 10.1016/j.nima.2020.164662.

[19] D. J. Thomas and A. V. Alevra. Bonner sphere spectrometers - A critical review. *Nuclear Instruments and Methods in Physics Research, Section A: Accelerators, Spectrometers, Detectors and Associated Equipment*, 476(1-2):12–20, 2002. 10.1016/S0168-9002(01)01379-1.

Part I

On the measurement of neutron spectra in radiation therapy

Chapter 2

Radiation physics and dosimetry

The transport of radiation in an absorbing medium is a stochastic process that is governed by many different types of interactions between the incoming particle and the medium. Every type of interaction has an associated probability that is expressed as a cross section. The concept of the interaction cross section comes from quantum mechanics and is expressed in units of area, often using the quantity known as a barn (1 b $= 10^{-28}$ m^2). Interaction cross sections depend on a variety of factors, including the energy of the particle as well as the atomic number and density of the absorber material with which the particle is interacting. This chapter presents an overview of the mechanisms by which various types of ionizing radiation interact with matter, with a focus on neutrons. A summary of the physical quantities and dosimetric concepts that are required for understanding the remainder of this thesis is also provided.

2.1 Charged particles

2.1.1 Classification of charged particles

Charged particles are any particles with an electric charge, which interact via Coulomb interactions. The charged particle species of interest in this thesis are electrons, positrons, protons, alpha particles, and heavier ions.

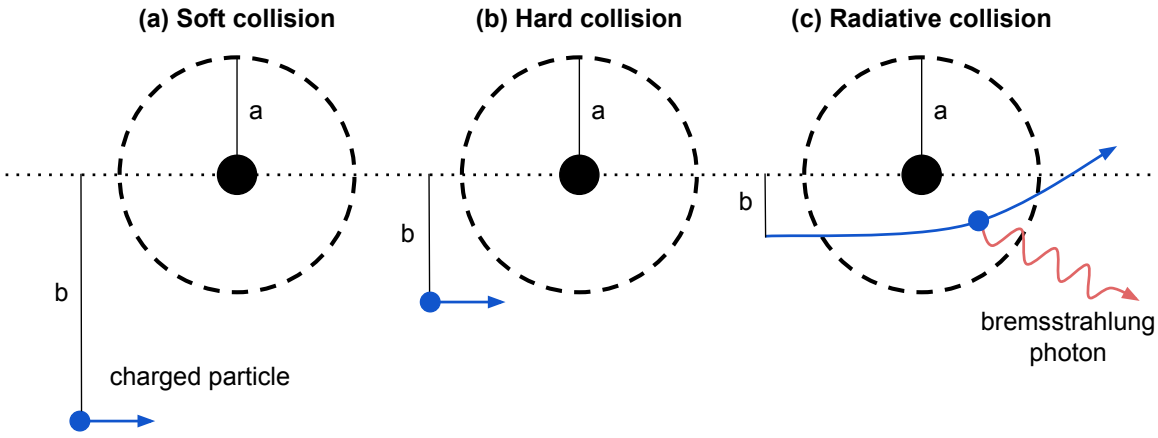

Figure 2.1 Charged particle interactions with the atoms of an absorbing material categorized by the relative magnitude of the impact parameter b and the atomic radius a in three ways: (a) soft collisions wherein $b >> a$, (b) hard collisions wherein $b \approx a$, and (c) radiative collisions wherein $b << a$. Figure adapted from Podgoršak [1].

2.1.2 Charged particle interaction mechanisms

When charged particles traverse an absorbing medium they undergo many Coulomb interactions with both the orbital electrons and the nuclei of the atoms that they encounter. These interactions are classified according to the magnitude of the impact parameter b, which is the perpendicular distance between the particle's trajectory and the centre of the target atom, relative to the classical atomic radius a. Three categories of charged particle interactions are shown schematically in Figure 2.1 and are described as follows [1]:

Soft collisions

A soft collision occurs between a charged particle and an entire atom (including all of its bound electrons) when $b >> a$. Although the energy transferred to an atom via a soft collision is quite small, it can be sufficient to cause atomic polarization, excitation, or ionization. These interactions have a high cross section compared to other charged particle interactions and account for approximately 50% of the energy transferred by a charged particle.

Hard collisions

A hard collision between a charged particle and a single atomically-bound electron occurs when $b \approx a$. In this case, a considerable amount of energy is transferred to the orbital electron that results in its ejection from the atom. The ejected electron is referred to as δ-ray and is sufficiently energetic to undergo Coulomb interactions with other atoms. Although the probability of a charged particle undergoing a hard collision is much lower than a soft collision, the energy transfer is much larger. Thus, these interactions also account for approximately 50% of the energy transferred by a charged particle.

Radiative collisions

A radiative collision between a charged particle and the nucleus of an atom can occur when $b << a$. Most of these interactions are elastic collisions with negligible energy loss and may involve a deflection. However, it is possible for the charged particle to undergo an inelastic collision, otherwise referred to as a bremsstrahlung collision, which results in considerable energy loss and the corresponding emission of an x-ray photon. The probability of inelastic radiative collisions is inversely proportional to the square of the mass of the charged particle, meaning that these interactions typically only occur for charged particles with relatively low mass (e.g. electrons and positrons).

2.2 Photons

2.2.1 Classification of photons

Photons are massless, uncharged particles that are the quanta of electromagnetic radiation. Photons with sufficiently high energy to ionize atoms are a form of indirectly ionizing radiation. Ionizing photons are generally classified into two categories, namely x-rays and gamma rays, based on their origin. X-rays are produced outside of atomic nuclei via a variety of processes such as electronic state transitions and the bremsstrahlung process. Gamma rays, however, originate from atomic nuclei and are produced by nuclear state transitions and nuclear reactions. Additional subclassifications of ionizing photons may be used, but these two categories are sufficient for the scope of this thesis.

2.2.2 Photon interaction mechanisms

The cross sections describing photon interactions with matter are highly dependent on the photon energy, the atomic number of the absorbing material (Z), and the mass density of the material (ρ). The interaction mechanisms that are most relevant in the context of radiation therapy are described below [1].

Rayleigh scattering

In Rayleigh scattering, also called coherent photon scattering, a photon undergoes an elastic interaction with the atomic electrons of an atom of the absorbing medium and experiences a deflection in its trajectory. This process is unimportant for dosimetric considerations because there is no energy transferred to the absorber. However, Rayleigh scattering is important to consider when modeling radiation transport. The interaction cross section for Rayleigh scattering decreases with increasing photon energy and increases with Z.

Photoelectric effect

The photoelectric effect is an interaction between a photon and an atomic electron that is characterized by the complete absorption of the photon and subsequent ejection of the electron from the atom. The ejected electron has a kinetic energy equal to that of the incident photon, minus the binding energy of that electron. In general, the photoelectric cross section decreases with increasing photon energy. However, there are sharp increases in the photoelectric cross section at discrete photon energies where the photon has sufficient energy to eject electrons from a particular orbital electron shell. The photoelectric cross section also increases with increasing Z.

Compton scattering

Compton scattering, also known as incoherent photon scattering, is the inelastic analog to Rayleigh scattering. In a Compton scattering event, the photon interacts with an atomic electron and is deflected. However, in this case, sufficient energy is imparted to the electron to cause its ejection from the atom with its own unique scattering angle. The relative kinetic energies imparted to the scattered photon and ejected electron, as well as their scattering angles, are probabilistic in nature. For most materials, the Compton scattering cross section has a maximum

value at an intermediate photon energy (keV–MeV). The peak energy and the magnitude of the Compton scattering cross section increase with absorber Z.

Pair production and triplet production

Pair production is characterized by the complete absorption of a photon by an absorber atom and the subsequent production of an electron-positron pair. This interaction is only possible when the photon energy exceeds the rest energy of an electron-positron pair (1.022 MeV, i.e. $2m_ec^2$). The energy of the incident photon is essentially split between the electron and positron, although a small amount is absorbed by the atomic nucleus to conserve momentum. When the photon energy exceeds 2.044 MeV (i.e. $4m_ec^2$), it is possible for some of the energy to be absorbed by an orbital electron. This process is known as triplet production. Triplet production is thus characterized by the emission of two electrons and one positron from the interaction site. The interaction cross sections for both pair and triplet production increase with photon energy and absorber Z.

Photonuclear reactions

At high photon energies, there is a chance for interactions to occur between photons and absorber nuclei. Such interactions, called photonuclear reactions, result in nuclear disintegration and corresponding energetic emission of one or more nuclear fragments. The total cross section for photonuclear reactions has two notable features: (i) a threshold energy below which these reactions do not occur and (ii) a prominent peak known as the "giant resonance" [1]. The threshold energy for photonuclear reactions is generally between 7–15 MeV. However, there are notable exceptions like the 1.7 MeV threshold for beryllium and the 2.2 MeV threshold for hydrogen [1]. Meanwhile, the resonance peak in the photonuclear cross section occurs around 20 MeV for low Z materials and around 12 MeV for high Z materials [1].

Even though the cross section for photonuclear reactions constitutes only a few percent of the total cross section for all possible photon interaction [1], these interactions are the most relevant for this thesis. The most probable photonuclear reactions involve the emission of a single neutron known as a photoneutron, and are broadly labeled as (γ, n) reactions. However, there are three distinct processes that contribute to the total cross section for photoneutron production: (i) photoionization, (ii) compound nucleus formation, and (iii) the quasi-deuteron effect [2].

1. In the photoionization process the entire photon energy is transferred to the neutron, minus the nuclear binding energy. Photoionization is the dominant means of photoneutron production for light nuclei and constitutes approximately 10–20% of photoneutron production for heavier nuclei.

2. Compound nucleus formation occurs when the photon is temporarily absorbed by an absorber nucleus, resulting in an excited nuclear state. The resulting de-excitation yields an energetic neutron whose energy follows a spectral distribution. Compound nucleus formation is the dominant means of photoneutron production for nuclei with atomic weights larger than 40.

3. The quasi-deuteron effect is a process that results in the production of neutron-proton pairs such that each particle carries about half of the initial photon energy. However, this process only occurs for photons with energies greater than 50 MeV, well above the energies encountered in photon and electron radiation therapy.

These photoneutron production processes together constitute the mechanism by which megavoltage photon beams generate secondary neutrons via interactions with the linac, the treatment room, and the patient. The total cross section for photoneutron production in tungsten and copper, two elements commonly used in the shielding material of linacs, are shown in Figure 2.2. Similar neutron-producing reactions are also possible for highly energetic electrons but the probability for such interactions is approximately 100 times lower [2].

2.3 Neutrons

2.3.1 Classification of neutrons

Like x-rays and gamma rays, neutrons are electrically neutral particles that may be considered a form of indirectly ionizing radiation. Unlike x-rays and gamma rays, neutrons have considerable mass ($m_{\mathrm{n}} = 939.6\ \mathrm{MeV/c^2}$) that is slightly larger than the mass of a proton ($m_{\mathrm{p}} = 938.3\ \mathrm{MeV/c^2}$). Owing to their mass, neutron interactions in matter are considerably different than photon interactions. The cross sections for neutron interactions have considerable energy dependence and, consequently, neutrons are often classified according to their energy. One possible neutron classification scheme is summarized in Table 2.1.

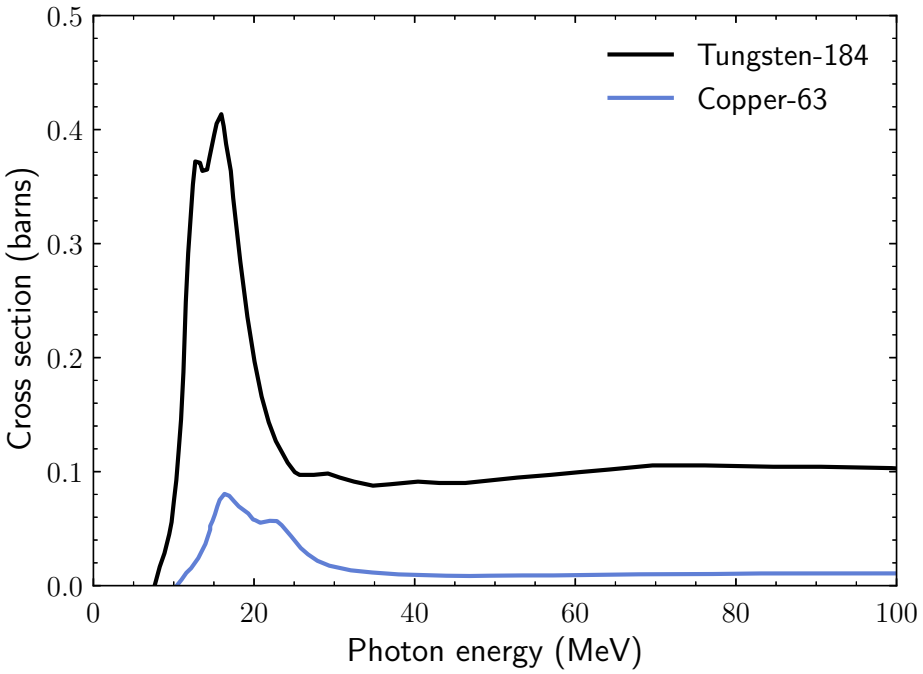

Figure 2.2 Total cross section for photoneutron production in two materials commonly found in medical linear accelerators. Data obtained from Kawano et al. [3].

2.3.2 Neutron interaction mechanisms

Neutrons interact with the nuclei of absorbers and undergo one of the following five types of interactions [1]:

Elastic scatter

Assuming the neutron is non-relativistic, an elastic scattering interaction between a neutron and a nucleus can be treated as a classical collision scenario wherein energy and momentum are conserved. In this scenario, the neutron transfers the following amount of kinetic energy to the nucleus:

$$\Delta E_{\mathrm{K}} = (E_{\mathrm{K}})_i \frac{4 m_{\mathrm{n}} \mathrm{M}}{(m_{\mathrm{n}} + \mathrm{M})^2} \cos^2 \phi \tag{2.1}$$

where $(E_{\mathrm{K}})_i$ is the initial kinetic energy of the neutron, M is the mass of the nucleus, and ϕ is the angle at which the nucleus recoils relative to the direction of the incident neutron. Because

Table 2.1 Classification scheme for categorizing free neutrons according to their energy [1, 4].

Category	Kinetic energy range
Ultracold	$E_K < 2 \times 10^{-7}$ eV
Very cold	2×10^{-7} eV $\leq E_K \leq 5 \times 10^{-5}$ eV
Cold	5×10^{-5} eV $\leq E_K \leq 0.025$ eV
Thermal	$E_K \approx 0.025$ eV
Epithermal	1 eV $\leq E_K \leq$ 1 keV
Intermediate	1 keV $\leq E_K \leq$ 100 keV
Fast	100 keV $\leq E_K \leq$ 20 MeV
Relativistic	20 MeV $\leq E_K$

of the inverse dependence on nuclear mass, relatively little energy is transferred to a heavy absorber via elastic scatter compared to lighter absorbers. The largest energy transfers occur with hydrogen atoms, and the resulting energetic proton will undergo many Coulomb reactions and generally not travel far. This property serves as the motivation to use hydrogenous materials to moderate high-energy neutrons for the purposes of both radiation protection and neutron detection.

The cross section for elastic scatter is relatively uniform with respect to neutron energy for most materials, as shown in Figure 2.3. However, there are sharp resonance peaks in the cross sections for certain materials (also shown in Figure 2.3). These resonances are the result of an alternative form of elastic scatter wherein the neutron is absorbed by a nucleus to form a compound nucleus and promptly followed by the emission of a neutron with the same energy [5].

Inelastic scatter

During inelastic neutron scatter, the neutron is temporarily absorbed by a nucleus resulting in a compound nucleus in an excited nuclear state. A neutron n' is then emitted with a lower energy in a different direction than that of the incident neutron. Finally, the excited nucleus reverts back to ground state via emission of a high-energy gamma ray, as described by the following equation:

$$\mathrm{n} + {}^{\mathrm{A}}_{\mathrm{Z}}\mathrm{X} \longrightarrow {}^{\mathrm{A+1}}_{\mathrm{Z}}\mathrm{X}^{*} \longrightarrow {}^{\mathrm{A}}_{\mathrm{Z}}\mathrm{X} + n' + \gamma \tag{2.2}$$

The inelastic scattering cross section is characterized by a energy threshold below which these reactions do not occur. This threshold for inelastic scatter varies by material, however it is generally on the order of a few MeV.

Neutron capture

Similar to inelastic scatter, neutron capture occurs when a neutron is absorbed by the nucleus to temporarily form a compound nucleus. However, in this case, the neutron remains in the nucleus and the excited nucleus is de-excited through the emission of a gamma ray or charged particle. These reactions are respectively denoted as (n,γ) and (n,x) for any charged particle x. Each of these reactions has an associated Q-value that quantifies the amount of energy released by the reaction, some of which is imparted to the reaction products.

Neutron capture cross sections generally decrease with increasing neutron energy until around 1 MeV, at which point a variety of resonance effects occur. Below 1 MeV these cross sections adhere to a $1/v$ dependence, where v is the velocity of the neutron [6]. An attractive option for detecting thermal neutrons is to use a material subject to neutron capture reactions that are characterized by (i) a large thermal neutron capture cross section and (ii) the production of short-ranged charged particles. These characteristics facilitate high detector sensitivity and the ability to distinguish neutron capture events from other interactions in the detector. These properties are discussed further in Chapter 3.

Neutron-induced fission

For heavy nuclei ($Z \geq 92$), the compound nucleus formed after neutron absorption can undergo nuclear fission. Fission is characterized by nuclear fragmentation into two lighter daughter nuclei and the emission of multiple fast neutrons. Because neutrons are both a reactant and product of nuclear fission, it is possible under the right conditions to achieve a chain reaction and substantial energy release. Nuclear reactors utilize this property in a controlled manner for scientific purposes or to generate power [1]. Although both fast and thermal neutrons can induce fission, the reaction does not play a role in the radiation therapy context because atomic nuclei with sufficiently high Z (i.e. fissionable nuclei) are generally not encountered.

Nuclear spallation

For neutrons with energies exceeding ~ 100 MeV, the nuclear spallation interaction is possible [1]. Nuclear spallation is the disintegration of a nucleus into many smaller components (e.g. protons, neutrons, alpha particles, etc.) as a result of impact or stress. Nuclear spallation does not play a role in photon and electron radiation therapy because neutrons of sufficiently high energy to induce spallation are not encountered.

Summary

The cross sections for neutron elastic scatter, inelastic scatter, as well as the (n,γ) and (n,p) capture reactions are shown for the four most abundant elements (by mass) in human tissue in Figure 2.3. These cross sections demonstrate the uniformity and predominance of elastic scatter at all energies in human tissue. The characteristic $1/v$ dependencies of various neutron capture cross sections are also shown. Generally speaking, neutron capture by nitrogen atoms is the dominant mechanism of energy deposition for thermal neutrons while elastic scatter with hydrogen atoms is the dominant mechanism of energy deposition for fast neutrons [1].

2.4 Physical and dosimetric concepts

This section defines a variety of physical and dosimetric concepts that are essential in order to quantify and understand the impact that neutrons have on the human body.

2.4.1 Fluence and flux

Particle fluence Φ is defined as the number of particles dN incident on a sphere of cross-sectional area dA [8]:

$$\Phi = \frac{\mathrm{d}N}{\mathrm{d}A} \tag{2.3}$$

and has units of inverse area (e.g. m^{-2}). A mathematically equivalent definition of fluence was conceived by Kellerer [9], which describes the mean particle fluence in a volume. In this formalism, fluence is calculated as the sum of the lengths of particle tracks ds that traverse a volume, divided by its cubic volume dV:

$$\bar{\Phi} = \frac{\sum \mathrm{d}s}{\mathrm{d}V} \tag{2.4}$$

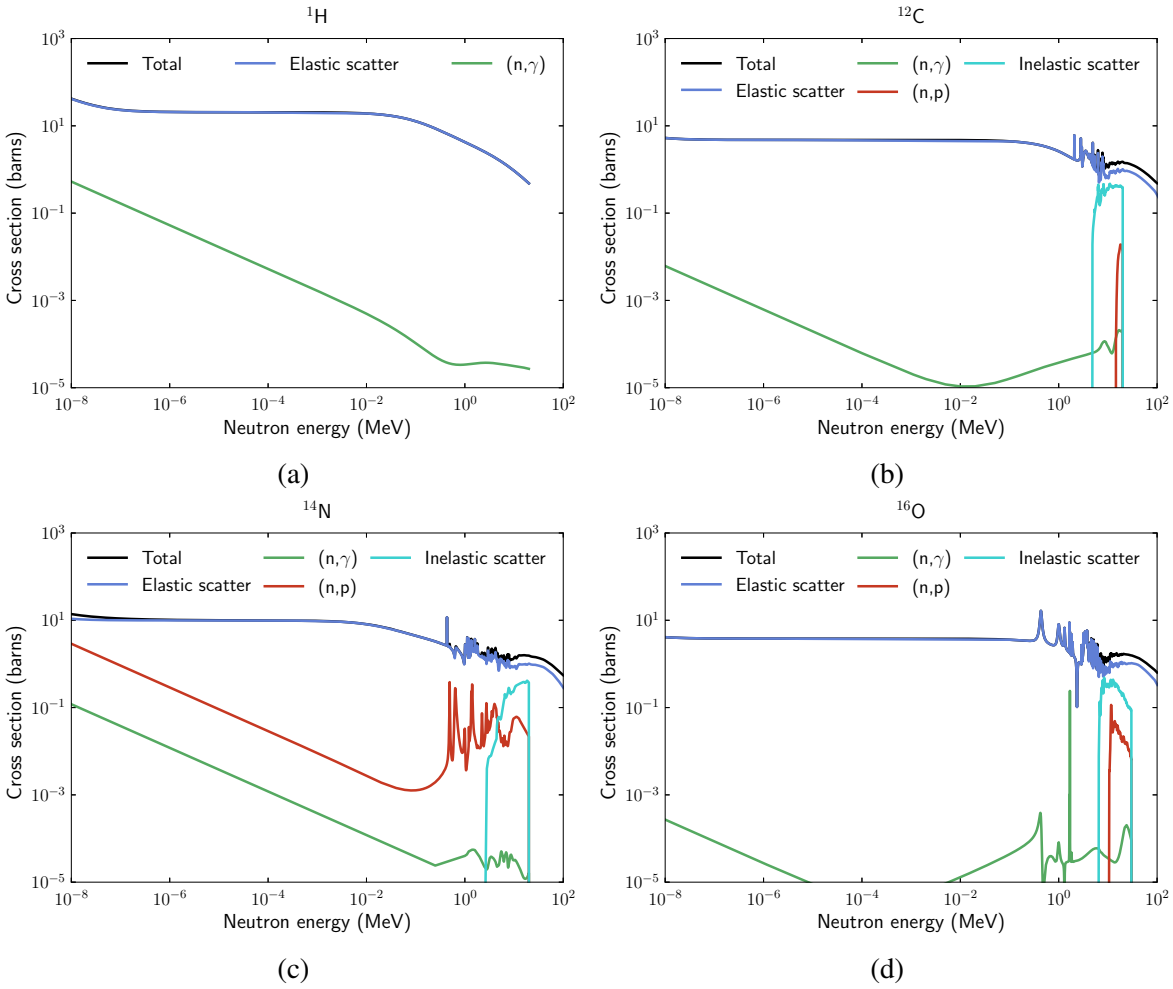

Figure 2.3 Neutron interaction cross sections for the four most abundant elements by mass in the human body: (a) hydrogen, (b) carbon, (c) nitrogen, and (d) oxygen. Data were obtained from the Evaluated Nuclear Data File (ENDF) [7].

This definition is more practical than the conventional definition in the context of Monte Carlo simulations of radiation transport [10].
The time derivative of particle fluence is known as the particle fluence rate, or particle flux:

$$\dot{\Phi} = \frac{\mathrm{d}\Phi}{\mathrm{d}t} \tag{2.5}$$

Finally, a polyenergetic field of a particular type of radiation can be described by the particle fluence spectrum:

$$\Phi_E(E) = \frac{\mathrm{d}\Phi}{\mathrm{d}E}(E) \tag{2.6}$$

2.4.2 Linear energy transfer

Linear energy transfer (LET) measures the rate of energy absorption by a medium as it is traversed by ionizing radiation [1].

$$\mathrm{LET} = \frac{\mathrm{d}E}{\mathrm{d}l} \tag{2.7}$$

LET is typically expressed in units of $\mathrm{keV{\cdot}\mu m^{-1}}$ and is used to describe the density of ionizations in an absorbing medium caused by radiation. Ionizing radiation with $\mathrm{LET} < 10\,\mathrm{keV{\cdot}\mu m^{-1}}$ is typically classified as sparsely ionizing or low LET radiation, while that with $\mathrm{LET} > 10\,\mathrm{keV{\cdot}\mu m^{-1}}$ is typically classified as densely ionizing or high LET radiation [1]. Example types of radiation within each category are provided in Table 2.2

2.4.3 Absorbed dose

Absorbed dose is a fundamental concept in medical physics and radiation oncology that is used to quantify the amount of radiation absorbed by an irradiated medium. Specifically, absorbed dose measures the amount of energy absorbed ΔE_{abs} by a volume of mass Δm [11]:

$$D = \frac{\Delta E_{\mathrm{abs}}}{\Delta m} \tag{2.8}$$

Although absorbed dose is technically a point quantity, it is typically used to express the average energy imparted over a macroscopic volume. The SI unit of absorbed dose is the gray (Gy), which is equal to $1\ \mathrm{J{\cdot}kg^{-1}}$. Throughout this thesis, absorbed dose is often referred to as dose, consistent with convention in the field.

Table 2.2 LET values for various types of ionizing radiation. Table adapted from Podgoršak [1].

LET classification	Particle	Kinetic energy	LET (keV·μm^{-1})
Low LET	X-rays	3 MeV	0.3
		250 kVp	2
	Electrons	1 MeV	0.25
		10 keV	2.3
High LET		1 keV	12.3
	Neutrons	14 MeV	12
	Protons	2 MeV	17
	Carbon ions	100 MeV	100-2000

2.4.4 Relative biological effectiveness

Relative biological effectiveness (RBE) is used to quantify the relative potency of two types of radiation to induce the same biological effect. The concept of RBE is used to recognize that not all types of ionizing radiation deposit dose in the same manner. For example, a densely ionizing radiation (high LET) tends to deposit energy in a more spatially-clustered manner than a sparsely ionizing radiation (low LET). These variations have important ramifications when considering dose deposition in biological targets like human tissue and DNA. Thus, RBE is generally calculated as [12]:

$$\text{RBE} = \frac{D_{\text{x}}}{D_{\text{test}}} \tag{2.9}$$

where D_{x} is the dose required by a reference radiation to induce a particular biological effect and D_{test} is the dose required by a "test" radiation of interest to induce the same effect. Typically low LET radiation such as 250 kVp x-rays, or gamma rays from the decay of ^{60}Co or ^{137}Cs are used as the reference radiation.

Although RBE and LET are closely related, their relationship is not always linear. For example, for the endpoint of cell killing, RBE increases with LET until achieving a maximum value between 100–200 keV·μm^{-1}, which is the optimal ionization density for inducing DNA double strand breaks. At larger LET values, RBE decreases because the additional density of ionizations does not lead to greater degree of cell killing, which is known as the overkill effect [11].

Table 2.3 Radiation weighting factors for various types of ionizing radiation. Table reproduced from ICRP Publication 103 [13].

Radiation type	Radiation weighting factor w_R
Photons	1
Electrons and muons	1
Protons and charged pions	2
Alpha particles, fission fragments, heavy ions	20
Neutrons	A continuous function of energy

In addition to the specified endpoint, RBE is highly dependent on variety of factors such as dose, dose rate, fractionation, tissue and cell type, etc. In general, RBE for stochastic effects is maximized at low doses of radiation because deterministic effects dominate at high doses [13].

2.4.5 Radiation weighting factors and equivalent dose

In 1991, the International Commission on Radiological Protection (ICRP) introduced the concept of the radiation weighting factor w_R to broadly account for the differences in RBE between different types of radiation (R) when assessing the dose deposited in human tissue [14]. These w_R values are based on aggregate experimental RBE data for inducing a variety of stochastic biological effects, such as carcinogenesis and life shortening in animals [13]. Specifically, the w_R values are based on experimental data obtained using low radiation doses where RBE for stochastic effects is maximized. Thus, the w_R values serve as conservative upper estimates of RBE for a variety of stochastic effects and are used for the purposes of radiation protection. This approach allows w_R to be presented independently of factors such as dose and dose rate. The values of w_R for various types of radiation are listed in Table 2.3.

Unlike other types of ionizing radiation, neutrons are assigned an energy dependent w_R by the ICRP. The original neutron w_R values included in ICRP Publication 60 [14] were revised in ICRP Publication 92 [15] in 2003 according to a review of more recent experimental RBE data. Another revision of the w_R values was published in the 2007 recommendations of the ICRP, as contained within ICRP Publication 103 [13]. These most recent recommendations describe neutron w_R as an empirical function of neutron energy E_n that is defined by the following

piecewise equation and is plotted in Figure 1.6.

$$w_{\mathrm{R}} = \begin{cases} 2.5 + 18.2e^{-[\ln(E_n)]^2/6} & E_n < 1 \text{ MeV} \\ 5.0 + 17.0e^{-[\ln(2E_n)]^2/6} & 1 \text{ MeV} \leq E_n \leq 50 \text{ MeV} \\ 2.5 + 3.25e^{-[\ln(0.04E_n)]^2/6} & E_n > 50 \text{ MeV} \end{cases} \tag{2.10}$$

Radiation weighting factors may be used to calculate a quantity known as equivalent dose, which has both clinical and scientific utilities. The equivalent dose delivered by one or more types of radiation R to a particular tissue or organ T is defined as:

$$H_{\mathrm{T}} = \sum_{\mathrm{R}} w_{\mathrm{R}} D_{\mathrm{T,R}} \tag{2.11}$$

Although the units of equivalent dose are technically the same as absorbed dose, equivalent dose is instead expressed in units of sieverts (Sv) to differentiate the two concepts.

2.4.6 Tissue weighting factors and effective dose

Tissue weighting factors w_{T} are another quantity created by the ICRP [14] that account for differences in the radiosensitivity of various tissues in the human body. The sum of w_{T} for all radiosensitive tissues is unity. w_{T} are used to weight the equivalent dose delivered to every exposed tissue type T as a means to calculate a quantity called effective dose:

$$E = \sum_{\mathrm{T}} w_{\mathrm{T}} H_{\mathrm{T}} \tag{2.12}$$

Similar to equivalent dose, effective dose is measured in units of sieverts. Both equivalent dose and effective dose are radiation protection quantities that are used to define radiation exposure limits for various populations. While these quantities are not measurable in practice, such limits serve as guides to ensure that the risk for stochastic health effects is kept below unacceptable levels [13].

2.4.7 Dose equivalent

Operational quantities known as dose equivalents are measurable quantities that can be used to monitor and quantify the amount of dose delivered to the human body during actual radiation

exposure scenarios [13]. In general, dose equivalent is measured in sieverts and is calculated using the following formula:

$$H = DQ \tag{2.13}$$

where D is the absorbed dose and Q is a radiation quality factor specific to each type of radiation. Q factors are broadly similar to w_{R} and are based on RBE but are more closely related to particle LET [13]. Quantitative differences between these factors can be clearly seen by comparing the neutron Q described by the United States Nuclear Regulatory Commission (US NRC) with the ICRP's w_{R} values, as shown in Figure 1.6.

There are two types of dose equivalent of interest:

1. Personal dose equivalent $H_{\mathrm{p}}(d)$ is used in individual dose monitoring to assess the effective dose delivered to an individual during a uniform, whole-body exposure. It is specified at a specific depth d in tissue below the point where the individual's dosimeter was worn.

2. Ambient dose equivalent $H^{*}(10)$ is used in area dose monitoring situations where individuals don't wear personal dosimeters (e.g. to assess aircrew exposure [13]). Specifically it is the dose equivalent produced by the given radiation field in the ICRU sphere [16] at a radial depth of 10 mm. The ICRU sphere is essentially a hypothetical soft-tissue phantom with a 30 cm diameter that is used to represent the human torso.

2.5 Summary

This chapter described the particle interactions, physical quantities, and dosimetric concepts that are referenced throughout the remainder of this thesis. Particular emphasis was given to the interactions that involve neutrons (either as reactants or products), as well as the quantities that describe the large, energy dependent stochastic risk associated with neutrons compared to other forms of radiation.

References

[1] E. B. Podgoršak. *Radiation Physics for Medical Physicists*. Springer International Publishing Switzerland, Swizterland, third edition, 2016.

[2] National Committee on Radiation Protection and Measurements. NCRP Report No. 31: Shielding for high·energy electron accelerator installations. Technical report, 1964.

[3] T. Kawano, et al. IAEA Photonuclear Data Library 2019. *Nuclear Data Sheets*, 163: 109–162, 2020. 10.1016/j.nds.2019.12.002.

[4] P. Andreo, D. T. Burns, A. E. Nahum, J. Seuntjens, and F. H. Attix. *Fundamentals of ionizing radiation dosimetry*. John Wiley and Sons Incorporated, Weinheim, Germany, 2017.

[5] E. Hussein. *Radiation Mechanics: Principles and Practice*. Elsevier Science, 2007.

[6] K. H. Beckhurts and K. Wirtz. *Neutron Physics*. Springer-Verlag Berlin Heidelberg, 1964.

[7] The Cross Section Evaluation Working Group. Report BNL-NCS-44945 (ENDF-102). Technical report, National Nuclear Data Center, 1995.

[8] J. P. Seuntjens, W. Strydom, and K. R. Shortt. Dosimetric Principles, Quantities and Units. In E. B. Podgoršak, editor, *Radiation Oncology Physics: A Handbook for Teachers and Students*, chapter 2, pages 45–70. International Atomic Energy Agency, Vienna, 2005.

[9] A. Kellerer. Considerations on the random traversal of convex bodies and solutions for general cylinders. *Radiation Research*, 47:359–376, 1971. 10.2307/3573243.

[10] G. H. Hartmann and P. Andreo. Fluence calculation methods in Monte Carlo dosimetry simulations. *Zeitschrift fur Medizinische Physik*, 29(3):239–248, 2019. 10.1016/j.zemedi.2018.08.003.

[11] P. Ortiz López, G. Rajan, and E. B. Podgoršak. Radiation Protection and Safety in Radiotherapy. In E. B. Podgoršak, editor, *Radiation Oncology Physics: A Handbook for Teachers and Students*, chapter 16, pages 549–609. International Atomic Energy Agency, Vienna, 2005.

[12] N. Suntharalingam, E. B. Podgoršak, and J. H. Hendry. Basic radiobiology. In *Radiation Oncology Physics: A Handbook for Teachers and Students*, chapter 14, pages 485–504. Vienna, 2005.

[13] ICRP. ICRP 103: The 2007 Recommendations of the ICRP. *Annals of the ICRP*, 37(2-4), 2007.

[14] International Commission on Radiological Protection. ICRP 60: The 1990 Recommendations of the International Commission on Radiological Protection. *Annals of the ICRP*, 21 (1-3), 1991.

[15] ICRP. ICRP 92: Relative Biological Effectiveness (RBE), Quality Factor (Q), and Radiation Weighting Factor (wR). *Annals of the ICRP*, 33(4), 2003.

[16] D. R. White, J. Booz, R. V. Griffith, J. J. Spokas, and I. J. Wilson. Report 44. *Journal of the International Commission on Radiation Units and Measurements*, os23(1), 1989. 10.1093/jicru/os23.1.report44.

Chapter 3

Detecting neutrons in radiation therapy

This chapter explains the fundamental principles of measuring neutron spectra in the context of radiation therapy. An overview of gas-filled detectors and how they can be used to detect both fast and slow neutrons is presented first. The design and operation principles of two notable neutron spectrometers, the Bonner Sphere Spectrometer (BSS) [1] and the Nested Neutron Spectrometer^{TM} (NNS) [2], are then presented. Finally, the chapter concludes with a review of several publications that have used these spectrometers to measure neutron fluence spectra in radiation therapy environments.

3.1 Radiation detection

Radiation detection refers to the measurement and quantification of ionizing radiation using instruments called radiation detectors. When radiation interacts with one of these devices, a measurable signal is produced that is often proportional to the amount of energy deposited. Broadly, radiation detectors can be classified as either a particle counter or a radiation dosimeter. Particle counters are designed to measure the number (or rate) of particles that traverse the detector while dosimeters measure dosimetric quantities, such as absorbed dose. Radiation detectors can also be classified as active or passive, depending on whether the signal is measurable in real-time or obtained via post-processing.

Although there are many types of radiation detectors, this chapter focuses on a subset of these devices that are used for detecting neutrons. In particular, gas-filled detectors are described in greatest detail because such a detector comprises the sensitive component of the NNS [2], which was used in the manuscripts presented in subsequent chapters.

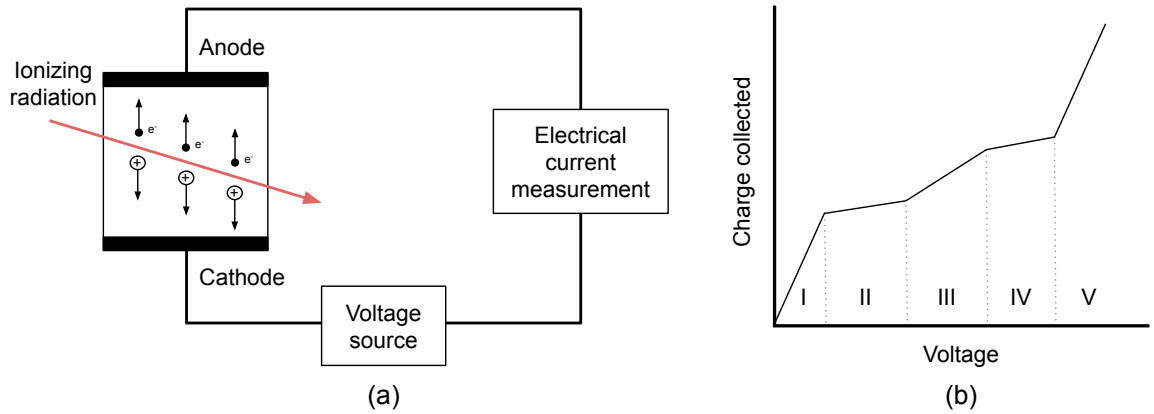

Figure 3.1 Design and operation of a gas-filled radiation detector. (a) Simplified schematic of the leaky capacitor design used in a gas-filled detector (b) Overview of the relationship between measured charge and the voltage applied to a gas-filled detector, classified into five regions: (I) recombination region, (II) ionization chamber region, (III) proportional counter region, (IV) Geiger-Müller plateau, (V) continuous discharge region. Figure adapted from [3].

3.2 Gas-filled detectors

The sensitive volume of a gas-filled detector is a chamber that contains a dielectric gas between a cathode and an anode [3]. The fundamental "leaky capacitor" design of a gas-filled detector is achieved when a voltage is applied to this chamber, as shown schematically in Figure 3.1(a). When there is no ionizing radiation present, the chamber acts as a capacitor and prevents the flow of electrical current. When irradiated, ionizations in the gas produce free electrons and positively-charged ions (i.e. ion pairs) that are attracted towards the appropriate electrode, thereby inducing a measurable current.

3.2.1 Types of gas-filled detectors

The charge collected in a gas-filled detector occurs over five distinct regions of operation defined by the applied voltage, as shown in Figure 3.1(b). Region I is known as the recombination region and is not useful for measuring radiation in practice. In this region the potential difference is insufficient to collect the liberated ion pairs at the electrodes before they recombine. Region V, the continuous discharge region, is also not used because a single ionization event can initiate a continuous electric discharge that completely saturates the detector. The remaining regions II,

III, and IV give rise to three different types of gas-filled detectors, each of which has its own unique advantages and disadvantages:

Ionization chambers

Gas-filled detectors operated in region II are known as ionization chambers. Under these conditions, the applied voltage is sufficiently high to collect all ion pairs at the electrodes but not high enough that liberated electrons undergo additional ionization events (i.e. charge multiplication) [3]. An ionization chamber cannot be used to detect and discriminate single particle interactions because the electrical signal produced by a single ionization is small relative to various measurement limitations such as noise and leakage. However, a measurable charge or current can be obtained by integrating over all ionizations caused in the detector. This measured charge can be related to the total amount of energy deposited if the average energy required to liberate an ion pair in the gas (i.e. the W-value of the gas) is known [4]. Thus, ionization chambers are very useful for measuring dosimetric quantities. For example, absorbed dose can be determined by dividing the total energy deposited by the mass of gas in the sensitive volume.

Proportional counters

When operated in region III, gas-filled detectors are known as proportional counters. Due to the higher voltage applied to a proportional counter than an ion chamber, the liberated electrons can gain sufficiently high energy to cause secondary ionizations [5]. These secondaries can also gain enough energy to cause additional ionization events before reaching the anode, thereby resulting in exponential growth of the measurable signal. This cascade of ionization events is known as a Townsend avalanche. Proportional counters are able to discriminate single ionization events in the gas because of the larger signal produced per ionization. The large measured signal is directly proportional to the energy deposited by the incoming radiation, which allows discrimination of particle type and energy in a mixed radiation field. Consequently, proportional counters are often used as neutron detectors.

Geiger-Müller counters

Geiger-Müller counters (or simply Geiger counters) are gas-filled detectors operated in region IV where the usable voltage range is highest. As with proportional counters, Geiger counters experience charge multiplication from primary ionization events that result in Townsend

avalanches. What differentiates a Geiger counter from a proportional counter is that the voltage is sufficiently high such that secondary charged particles can cause molecular excitations in the gas [5]. Subsequent de-excitation of these molecules may involve the emission of a UV photon that can then cause additional ionization events and subsequent Townsend avalanches throughout the gas volume. This Geiger discharge process, is eventually halted by the buildup of positive ions around the anode that disrupts the electric field applied by the potential difference. The signal produced by a Geiger counter is very strong but is essentially independent of the type and energy of the initial radiation. As a result, Geiger counters are commonly used as survey meters to detect the presence of ionizing radiation but not to for quantification purposes.

3.2.2 Pulse mode vs current mode

Gas-filled detectors are active detectors that can be operated in one of two signal-readout modes depending on the attached electronics: pulse-mode or current-mode [5].

In pulse-mode, the detector generates a distinguishable signal for every initial ionization event in the gas. This signal encapsulates both the amplitude and timing of the charge pulse caused by the associated ionization event. Specific particle energies can be identified by incorporating an electronic discriminator that only records pulses that exceed a certain magnitude or that are within a certain range of magnitudes. When operated in pulse-mode, the issues of pulse pileup and detector dead time must be considered [6]. Pulse pileup occurs when two signal pulses occur sufficiently close to each other that they are treated as a single pulse with a magnitude equal to the sum of the two pulses. Such a pulse is incorrectly interpreted as having been caused by a single, larger magnitude event. Detector dead time is the time period after a pulse is recorded during which the electronics are processing the measurement and are insensitive to other radiation events. When the count rate is sufficiently large, the detector becomes overwhelmed by pulse pileup and saturated with detector deadtime. Thus, pulse-mode detectors are only suitable for detecting radiation events with a suitably low count rate.

In current-mode, the detector is equipped with different electronics that are operated at a slower response time in order to measure the time-averaged current that results from many individual charge pulses [5]. Integrating-mode is a variation of current mode wherein the detector simply accumulates the charge pulses over the entire exposure to obtain the resulting total charge. Thus, current mode can be reliably used in high count-rate environments but cannot distinguish individual events.

3.3 Detecting neutrons

3.3.1 Neutron detectors

Neutron detectors typically contain a compound with a high cross section for a particular neutron interaction. Proportional counters containing a material with a suitably high neutron capture cross section allow active readout but are often also sensitive to other forms of radiation, which must be accounted for in a mixed radiation field. Another means to detect neutrons involves using metallic activation foils with large neutron capture cross sections. Foils can be used to selectively measure neutrons in a mixed radiation field but require passive, time-intensive readout techniques [5]. Because of the characteristic $1/v$ energy dependence of neutron capture cross sections, both proportional counters and activation foils are only practical for measuring slow neutrons.

Other devices like thermoluminescent dosimeters (TLDs), optically-stimulated luminescent dosimeters (OSLDs), and bubble detectors are useful for estimating dosimetric quantities like neutron dose equivalents that result from a range of neutron energies. However, these devices make assumptions about the underlying fluence spectrum and cannot be used to measure neutron spectra. The inability to measure neutron spectra is particularly notable given the marked energy dependence of neutrons for inducing stochastic effects as described by the neutron w_{R} and Q factors. It is thus of interest to consider how to measure a spectrum of neutrons containing both fast and slow neutrons.

3.3.2 Detecting slow neutrons

Three elements that are commonly used in slow neutron detectors are ^{3}He, ^{10}B, and ^{6}Li [5]. Each of these elements has an associated thermal neutron capture reaction that is characterized by the following properties:

1. The magnitude of capture cross section is large, which means that a high percentage of incoming neutrons will interact with the detector.

2. The reaction has a large Q-value. When capturing slow (low energy) neutrons, essentially all the energy released by the reaction (i.e. the Q-value) is transferred to the reaction products.

Table 3.1 Neutron capture reactions commonly used in slow neutron detectors. Data were obtained from the Evaluated Nuclear Data File (ENDF) [7].

Reaction	Q-value (MeV)	Thermal neutron cross section (b)
$^{3}\mathrm{He}(\mathrm{n},\mathrm{p})^{3}\mathrm{H}$	0.764	5316
$^{10}\mathrm{B}(\mathrm{n},\alpha)^{7}\mathrm{Li}$	2.790	3844
$^{6}\mathrm{Li}(\mathrm{n},\alpha)^{3}\mathrm{H}$	4.783	940

3. The reaction products are short-ranged charged particles, so that they are completely absorbed in the detector. The resulting signal is thus essentially proportional to the large Q-value of the reaction, which allows detection of individual neutron capture events.

The neutron capture reactions of interest for these three elements are summarized in Table 3.1. Of these reactions, the $^{3}\mathrm{He}(\mathrm{n},\mathrm{p})^{3}\mathrm{H}$ reaction has the largest thermal neutron capture cross section but suffers from the lowest Q-value. Inversely, the $^{6}\mathrm{Li}(\mathrm{n},\alpha)^{3}\mathrm{H}$ reaction has the largest Q-value but the lowest thermal neutron capture cross section. Meanwhile, the $^{10}\mathrm{B}(\mathrm{n},\alpha)^{7}\mathrm{Li}$ reaction has an intermediate Q-value and cross section.

These elements can be incorporated into a detector in a variety of ways. For example, the gas in a proportional counter can directly contain one of these elements or the inner surface of the cavity can be coated with a compound containing the element.

3.3.3 Detecting fast neutrons

The most common approach for detecting fast neutrons is to slow the neutrons before they reach a thermal neutron detector. This is achieved by encapsulating the thermal neutron detector in a moderating material with a large cross section for elastic neutron scatter. The moderator preferentially absorbs thermal neutrons and slows fast neutrons before they reach the thermal detector. In doing so, the sensitivity of the detector is essentially shifted from thermal neutrons to higher energy neutrons. The basis of measuring neutron spectra is thus to acquire multiple measurements with differing amounts of moderating material around the thermal neutron detector, such that each measurement preferentially detects neutrons at different energies.

3.4 Neutron spectrometers

Neutron spectrometers are sophisticated radiation detectors that enable detection of neutron fluence spectra. Determination of the full neutron spectrum is important from a radiation safety perspective because of the marked energy dependence of neutron RBE for inducing stochastic effects [8, 9]. Neutron spectrometers typically include a sensitive thermal neutron detector and multiple moderators of increasing size to enable detection of a range of higher energy neutrons.

Two neutron spectrometers that have been used extensively in the context of radiation therapy are the BSS [1] and the NNS [2]. These devices cannot directly measure neutron fluence spectra owing to the fact that a spectrum is a continuous differential quantity [10]. Instead, these devices measure a finite set of integrated counts (or count rates) and a fluence spectrum is obtained by deconvolving these measured counts with the response functions of the detector in a process known as unfolding. An overview of the BSS, the NNS, and the unfolding process is provided in the following sections.

3.4.1 The Bonner Sphere Spectrometer

The first BSS was developed by Bramblett et al. [1] in 1960. The BSS is characterized by a thermal neutron detector encapsulated in one of several moderating spheres of varying thickness. A photo of BSS moderating spheres of varying sizes is shown in Figure 3.2. For every unique combination of a thermal neutron detector and moderator there is an associated detector response function that characterizes the energy-dependent response of that configuration.

Thermal neutron detector

In the original BSS [1], a small ^{6}LiI(Eu) scintillator was used as the thermal neutron detector. Although this scintillator was a good starting point to demonstrate the potential utility of the BSS, it had difficulties in discriminating photon interactions [12]. Since the initial publication, many other thermal neutron detectors have been implemented into BSS systems including a variety of proportional counters [12]. Gold activation foils (^{197}Au) have also been extensively used in BSS systems to measure neutron spectra in radiation therapy environments [10, 13–18]. These foils are relatively insensitive to photons and have no dead time, making them well suited for use around a linac [12]. One drawback is that the analysis of activated gold foils

Figure 3.2 Bonner Sphere Spectrometer moderators. Photo obtained from the ELSE Nuclear website [11].

requires passive detector readout of the resulting 411 keV gamma ray emissions, typically using a high-purity germanium detector [10, 19].

Fast neutron moderators

Spherical fast neutron moderators are typically made of a hydrogenous plastic material called polyethylene $\left(\left(C_2H_4\right)_n\right)$ [1, 12], although other materials like liquid water have been used [20]. There is no ideal quantity and thickness of moderators [12], however, there should be a sufficient number of moderators with meaningfully different response functions in order to sample contributions from the full neutron energy range of interest. In practice, most BSS systems use around six moderators with thicknesses that vary between 2 and 12 inches [1, 10, 12].

Detector response functions

The response functions $R_i(E)$ of a detector essentially constitute a map between the neutron-induced measurements M_i and the neutron fluence spectrum at the point of measurement $\Phi_E(E)$ [19]. This relationship is described for every configuration i of a thermal neutron detector and

fast neutron moderator by a Fredholm integral of the first kind:

$$M_i = \int R_i(E)\,\Phi(E)\,\mathrm{d}E \tag{3.1}$$

In practice, detector response values can be obtained for only a finite number of neutron energies J, resulting in the following discrete version of Equation 3.1:

$$M_i = \sum_{j}^{J} R_{ij}\Phi_j \tag{3.2}$$

Detector response functions for a particular thermal neutron detector and fast neutron moderator can be determined numerically using Monte Carlo simulations of radiation transport [12] (described generally in Chapter 7). Using Monte Carlo, the shape, materials, and efficiency of the detector are modeled and subsequently irradiated with a uniform neutron fluence. In general, the detector response function of a particular configuration is the resulting number of neutron capture reactions in the thermal neutron detector per unit fluence as a function of neutron energy. Example response functions for the ^{197}Au-based BSS system developed by Howell et al. [10] are shown in Figure 3.3. These response functions demonstrate how the primary sensitivity of the detector shifts from low neutron energies to high neutron energies with increasing moderator thickness. A set of response functions can be validated by unfolding BSS measurements made around a radioactive source with a known neutron fluence spectrum, such as ^{252}Cf or americium-beryllium (AmBe), and comparing the result.

Unfolding BSS measurements

Generally, the number of neutron energies J over which the response functions are defined is greater than the number of measurements I. Thus, Equation 3.2 describes an ill-posed deconvolution problem that cannot be analytically solved for $\Phi(E)$. Indeed, there are an infinite number of possible neutron spectra that can fit the measured data [10, 12]. However, an appropriate neutron fluence spectrum can be determined using one of many possible unfolding techniques, several of which are summarized by Matzke [21].

Typically, the objective of unfolding techniques is to minimize some parameter that encapsulates both the measured data and the estimated fluence spectrum, such as a χ^2 value [12]. All unfolding techniques require an initial guess of the neutron spectrum Φ_j^0, in addition to the measured BSS data M_i and the response functions R_{ij}. Overall there is considerable subjectivity

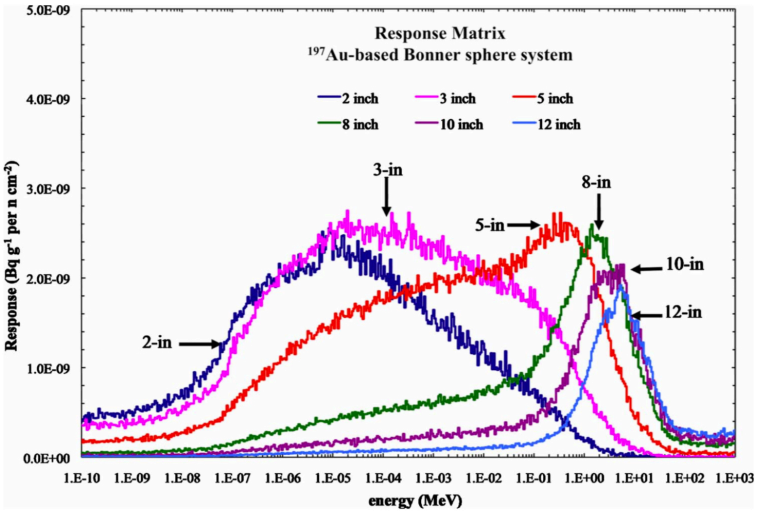

Figure 3.3 Detector response functions of the ^{197}Au-based Bonner Sphere Spectrometer system developed by Howell et al. [10].

in the unfolding process, including the choice of Φ_j^0 and the choice of parameter to evaluate the unfolded spectrum. These sources of subjectivity can result in both inter-user and intra-user variations in unfolded spectra.

Summary

For many years, the BSS has been the *de facto* neutron spectrometer in many fields, including radiation therapy. The system has many positive features, including the ability to detect an extremely wide range of neutron energies (from thermal to GeV), a nearly isotropic response, and relatively simple operation principles [13]. The main drawbacks of the BSS include:

- A slow measurement process due to the cumbersome nature of the spherical moderators, which is exacerbated when a passive thermal neutron detector is used.
- The moderators cannot be nested inside each other, which makes them difficult to transport.
- The various ambiguities associated with the unfolding process.

3.4.2 The Nested Neutron Spectrometer

The NNS is a modern spectrometer that was developed by Dubeau et al. [2] in 2012. This device has similar operation principles as the BSS but features a streamlined design to facilitate more rapid measurement acquisition and easier handling.

Thermal neutron detector

The NNS utilizes a ^{3}He proportional counter as the thermal neutron detector, which can be operated in pulse-mode or current-mode. While this detector is primarily sensitive to neutrons, it does have a non-negligible photon response. This drawback can be readily accounted for in pulse-mode by isolating the spectral peak caused by the protons produced by the $^{3}\mathrm{He}(\mathrm{n},\mathrm{p})^{3}\mathrm{H}$ reaction. In current-mode, this drawback must be accounted for by using a ^{4}He detector that has the same physical dimensions and photon response as the ^{3}He detector but is insensitive to neutrons. One must simply repeat every NNS measurement with both detectors and subtract the ^{4}He reading from the ^{3}He reading to obtain the net neutron-only signal [22]. When operated in current-mode, the measured current is converted to the corresponding count rate using a vendor-specified calibration coefficient [22].

Fast neutron moderators

The NNS has seven concentric cylindrical moderator shells that are assembled in Russian nesting doll fashion, as shown in Figure 3.4(a). Each of these shells is constructed of high-density polyethylene (HDPE) and increase in diameter from 3 to 10 inches [22]. The dimensions of the NNS shells were optimally designed to achieve a nearly isotropic response to incident neutrons [2].

Detector response functions

The response functions for each moderator configuration of the NNS containing a ^{3}He proportional counter are defined between 1.2 meV and 15.9 MeV as shown in Figure 3.4(b). A similar shift in the energy sensitivity can be seen in these response functions as those describing the ^{197}Au-based BSS system of Howell et al. [10] (Figure 3.3).

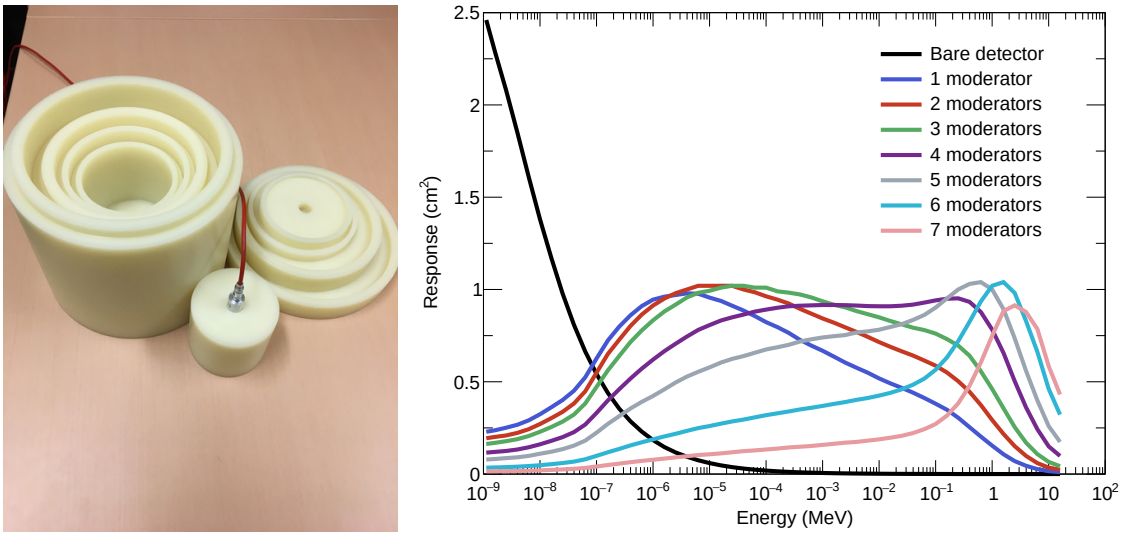

(a) (b)

Figure 3.4 The Nested Neutron Spectrometer (NNS). (a) Photograph of the HDPE cylindrical moderator shells and the ^{3}He proportional counter. (b) The NNS response functions.

Unfolding NNS measurements

Measurements obtained with the NNS can be unfolded using all of the same techniques used to unfold BSS measurements. However, a custom implementation of the iterative Maximum-Likelihood Expectation–Maximization (MLEM) algorithm [23] that was developed by Maglieri et al. [22] has been used by this research group to unfold NNS measurements. This approach and our rational for adopting it are described in greater detail in the following manuscript-based chapters.

Validation for use in radiation therapy

Although the current-mode of the NNS was calibrated in the low count-rate environment around an AmBe source [2, 19, 22] it can be operated in the high count-rate environment around a linac. A preliminary validation of the NNS in high count-rate environments was conducted by Maglieri et al. [22], who used the NNS to measure neutron fluence spectra at several locations in a radiation therapy bunker and found consistency with Monte Carlo generated spectra. Subsequently, Mathew et al. [19] developed a passive NNS with ^{197}Au foils in place of the ^{3}He proportional counter and used it to measure and compare with spectra generated

using the conventional NNS. Results were in good agreement between the two detectors, which served to validate use of the NNS in high count-rate radiation therapy environments. Moreover, the streamlined design and efficient, active measurement process make the NNS an appealing choice for such measurements.

3.5 Review of neutron spectral investigations in radiation therapy

As discussed in Chapter 1, the neutron fluence spectrum produced by a linac operated at high energies ($\gtrsim$ 8 MeV) is characterized by a fast peak, a thermal peak, and an intermediate energy tail. Several published studies have demonstrated that the relative prominence of the fast peak and thermal peak changes with increasing distance from the linac [13, 22, 24, 25]. Other variations in the shape and magnitude of neutron spectra due to variations in treatment parameters have been investigated by many authors and are summarized here.

The particle type and energy of the beam have a large impact on the neutron fluence spectrum. For photon beams, the neutron spectrum can increase by approximately an order of magnitude by increasing the energy from 10 MV to 15 MV and is a few times higher still at 18 MV [10, 26]. The neutron spectra produced by electron beams also vary significantly with beam energy [27], although the magnitude is generally smaller than for photon beams (e.g. the spectrum produced by a 20 MeV electron beam is similar in magnitude to a 10 MV photon beam). Clinical proton beams produced by a synchrotron generate neutron spectra with a third characteristic peak that is centred around the maximum beam energy (e.g. 250 MeV) [28]. This peak arises because the neutrons produced by the direct photoionization process have higher energies than for photon and electron beams, and are thus energetically distinct from those arising from the compound nucleus process. The linac make and model also can have a large impact on neutron fluence spectra, as demonstrated by Howell et al. [10]. Additionally, a variety of linac collimation settings can affect the neutron spectrum, such as the field size [16, 27] or the presence of the MLC [16].

Use of flattening-filter-free (FFF) beams has the potential to reduce photoneutron production, as was investigated by Kry et al. [15, 29]. Implementation of FFF beams has recently become possible because modern computerized treatment planning algorithms can perform calculations using beams without a flat profile [30]. FFF beams offer several advantages, including the

capability to deliver higher dose rates (i.e. faster treatments), reduce photon leakage from the linac, and reduce photoneutron production [30]. Indeed, Kry et al. [15, 29] found that a ∼70% reduction in photoneutron production per unit of photon dose was possible by experimentally removing the flattening filter from the 18 MV beam of a Varian Clinac 21EX. However, until the recent publication by our group (Chapter 4), there was a lack of data on photoneutron production by lower energy FFF beams and for modern linacs with clinically-commissioned FFF beams.

References

[1] R. L. Bramblett, R. I. Ewing, and T. W. Bonner. A new type of neutron spectrometer. *Nuclear Instruments and Methods*, 9(1):1–12, 1960. 10.1016/0029-554X(60)90043-4.

[2] J. Dubeau, S. S. Hakmana Witharana, J. Atanackovic, A. Yonkeu, and J. P. Archambault. A neutron spectrometer using nested moderators. *Radiation Protection Dosimetry*, 150(2): 217–222, 2012. 10.1093/rpd/ncr381.

[3] N. Tsoulfanidis and S. Landsberger. *Measurement and Detection of Radiation*. Taylor & Francis Group, Boca Raton, fourth edition, 2015.

[4] G. F. Knoll. *Radiation Detection and Measurement*. Wiley, New York, third edition, 2001.

[5] G. F. Knoll. Radiation measurement, 2017. https://www.britannica.com/technology/radiation-measurement.

[6] S. Usman and A. Patil. Radiation detector deadtime and pile up: A review of the status of science. *Nuclear Engineering and Technology*, 50(7):1006–1016, 2018. 10.1016/j.net.2018.06.014.

[7] The Cross Section Evaluation Working Group. Report BNL-NCS-44945 (ENDF-102). Technical report, National Nuclear Data Center, 1995.

[8] ICRP. ICRP 103: The 2007 Recommendations of the ICRP. *Annals of the ICRP*, 37(2-4), 2007.

[9] US NRC. Units of Radiation Dose. *Code of Federal Regulations*, 10(20.1004):298–300, 2021.

[10] R. M. Howell, S. F. Kry, E. Burgett, N. E. Hertel, and D. S. Followill. Secondary neutron spectra from modern Varian, Siemens, and Elekta linacs with multileaf collimators. *Medical Physics*, 36(9):4027–4038, 2009. 10.1118/1.3159300.

[11] ELSE Nuclear. Bonner Spheres Spectrometer. http://www.elsenuclear.com/en/bonner-spheres-spectrometer.

[12] D. J. Thomas and A. V. Alevra. Bonner sphere spectrometers - A critical review. *Nuclear Instruments and Methods in Physics Research, Section A: Accelerators, Spectrometers, Detectors and Associated Equipment*, 476(1-2):12–20, 2002. 10.1016/S0168-9002(01)01379-1.

[13] D. J. Thomas, A. G. Bardell, and E. M. Macaulay. Characterisation of a gold foil-based Bonner sphere set and measurements of neutron spectra at a medical accelerator. *Nuclear Instruments and Methods in Physics Research, Section A: Accelerators, Spectrometers, Detectors and Associated Equipment*, 476(1-2):31–35, 2002. 10.1016/S0168-9002(01)01384-5.

[14] R. M. Howell, N. E. Hertel, Z. Wang, J. Hutchinson, and G. D. Fullerton. Calculation of effective dose from measurements of secondary neutron spectra and scattered photon dose from dynamic MLC IMRT for 6 MV, 15 MV, and 18 MV beam energies. *Medical Physics*, 33(2):360–368, 2006. 10.1118/1.2140119.

[15] S. F. Kry, et al. Energy spectra, sources, and shielding considerations for neutrons generated by a flattening filter-free Clinac. *Medical Physics*, 35(5):1906–1911, 2008. 10.1118/1.2905029.

[16] R. M. Howell, S. F. Kry, E. Burgett, D. Followill, and N. E. Hertel. Effects of tertiary MLC configuration on secondary neutron spectra from 18 MV x-ray beams for the Varian 21EX linear accelerator. *Medical Physics*, 36(9):4039–4046, 2009. 10.1118/1.3159301.

[17] K. Amgarou, V. Lacoste, A. Martin, B. Asselineau, and L. Donadille. Neutron spectrometry with a passive bonner sphere system around a medical LINAC and evaluation of the associated unfolding uncertainties. *IEEE Transactions on Nuclear Science*, 56(5): 2885–2895, 2009. 10.1109/TNS.2009.2026416.

[18] S. Garny, V. Mares, H. Roos, F. M. Wagner, and W. Rühm. Measurement of neutron spectra and neutron doses at the Munich FRM II therapy beam with Bonner spheres. *Radiation Measurements*, 46(1):92–97, 2011. 10.1016/j.radmeas.2010.08.015.

[19] F. Mathew, C. Chilian, L. Montgomery, and J. Kildea. Development of a passive gold-foil Nested Neutron Spectrometer to validate the active current-mode He-3 measurements in a high neutron fluence rate radiotherapy environment. *Nuclear Instruments and Methods in Physics Research, Section A: Accelerators, Spectrometers, Detectors and Associated Equipment*, 985:164662, 2021. 10.1016/j.nima.2020.164662.

[20] P. Qi, et al. Design and performance of the Water-moderator nested spheres neutron spectrometer. *Nuclear Instruments and Methods in Physics Research, Section A: Accelerators, Spectrometers, Detectors and Associated Equipment*, 988:164868, 2021. 10.1016/j.nima.2020.164868.

[21] M. Matzke. Propagation of uncertainties in unfolding procedures. *Nuclear Instruments and Methods in Physics Research, Section A: Accelerators, Spectrometers, Detectors and Associated Equipment*, 476(1-2):230–241, 2002. 10.1016/S0168-9002(01)01438-3.

[22] R. Maglieri, A. Licea, M. Evans, J. Seuntjens, and J. Kildea. Measuring neutron spectra in radiotherapy using the nested neutron spectrometer. *Medical Physics*, 42(11):6162–6169, 2015. 10.1118/1.4931963.

[23] A. P. Dempster, N. M. Laird, and D. B. Rubin. Maximum Likelihood from Incomplete Data via the EM Algorithm. *Journal of the Royal Statistical Society. Series B (Methodological)*, 39(1):1–22, 1977. 10.1142/9789812388759_0028.

[24] K. Amgarou, V. Lacoste, A. Martin, B. Asselineau, and L. Donadille. Neutron spectrometry with a passive bonner sphere system around a medical LINAC and evaluation of the associated unfolding uncertainties. *IEEE Transactions on Nuclear Science*, 56(5): 2885–2895, 10 2009. 10.1109/TNS.2009.2026416.

[25] A. M. Fontanilla, et al. Neutron spectrometry with an 115In-based multi-shell neutron spectrometer in a medical linear accelerator facility. *Nuclear Instruments and Methods in Physics Research, Section A: Accelerators, Spectrometers, Detectors and Associated Equipment*, 993:165078, 2021. 10.1016/j.nima.2021.165078.

[26] R. M. Howell, et al. Measurements of secondary neutron dose from 15 MV and 18 MV IMRT. *Radiation Protection Dosimetry*, 115(1-4):508–512, 2005. 10.1093/rpd/nci041.

[27] F. Mathew, G. A. Makdessi, L. Montgomery, M. Evans, and J. Kildea. The impact of treatment parameter variation on secondary neutron spectra in high-energy electron beam radiotherapy. *Physica Medica*, 80:125–133, 2020. 10.1016/j.ejmp.2020.10.016.

[28] R. M. Howell and E. A. Burgett. Secondary neutron spectrum from 250-MeV passively scattered proton therapy: Measurement with an extended-range Bonner sphere system. *Medical Physics*, 41(9):1–8, 2014. 10.1118/1.4892929.

[29] S. F. Kry, et al. Reduced Neutron Production Through Use of a Flattening-Filter-Free Accelerator. *International Journal of Radiation Oncology Biology Physics*, 68(4):1260–1264, 2007. 10.1016/j.ijrobp.2007.04.002.

[30] D. Georg, T. Knöös, and B. McClean. Current status and future perspective of flattening filter free photon beams. *Medical Physics*, 38(3):1280–1293, 2011. 10.1118/1.3554643.

Chapter 4

The effect of the flattening filter on photoneutron production at 10 MV in the Varian TrueBeam linear accelerator

Logan Montgomery, Michael Evans, Liheng Liang, Robert Maglieri, John Kildea

Article published in: *Medical Physics, vol. 45(10), 2018, 4711-4719. DOI: 10.1002/mp.13148*

4.1 Preface

As discussed in the previous chapter, published studies using BSS systems have shown that the photoneutron fluence per unit photon dose can be reduced by using an 18 MV FFF beam instead of an 18 MV beam [1, 2]. As these previous studies involved non-clinical beams, we identified the need for additional experimental data on FFF beams that can be commissioned for clinical use on modern linac models, such as the Varian TrueBeam. Nominally, 10 MV beams are the lowest energy beams at which photoneutron production is a concern and are clinically of interest because of their potential for improved skin-sparing and deeper penetration compared to 6 MV beams. Thus, we carried out an investigation using the NNS to measure and compare the photoneutron fluence spectra produced by the 10 MV and 10 MV FFF beams of a Varian

Truebeam linac. For the purposes of this thesis, this study served to demonstrate our ability to use the NNS to provide clinical information of value.

4.2 Abstract

Purpose: Neutrons are an unavoidable by-product of high-energy radiation therapy treatments that deliver unwanted nontarget dose to patients. Use of flattening-filter-free (FFF) photon beams has been shown to significantly reduce photoneutron production per monitor unit (MU) of dose delivered. The purpose of this investigation was to characterize the photoneutron production of the 10 MV and 10 MV FFF beams of the Varian TrueBeam^{TM} linear accelerator.
Methods: Neutron fluence spectra were measured using a Nested Neutron Spectrometer^{TM} (NNS, Detec Inc., Gatineau, Canada). The ratios of neutron fluence and ambient dose equivalent for the 10 MV FFF beam relative to the 10 MV beam, dubbed FF-ratios (FFF/FF), were used to characterize the difference between the two beams. FF-ratios were compared under the following three conditions (1) per MU, at various locations in the treatment room, (2) per MU, with the linac jaws opened and closed, and (3) per electron striking the bremsstrahlung target, as opposed to per MU, at one location with the jaws closed.
Results: On average, the neutron fluence for the 10 MV FFF beam was 37% lower per MU than the 10 MV beam (FF-ratio = 0.63). The FF-ratio in neutron fluence and ambient dose equivalent did not vary by much between different locations within the treatment room. However, the FF-ratio in neutron ambient dose equivalent was reduced significantly when the linac jaws were opened compared to closed, which implies that the jaws contribute more to the photoneutron spectrum of the 10 MV FFF beam than to the 10 MV beam. Finally, it was found that the 10 MV FFF beam produces more photoneutrons per electron striking the bremsstrahlung target than the 10 MV beam (FF-ratio = 2.56).
Conclusions: The photoneutron fluence per MU produced by the 10 MV FFF beam is 37% lower than the 10 MV beam of a Varian TrueBeam linac. Accordingly, a reduction in neutron dose received by patients is achieved through use of the unflattened beam, provided that treatment plans for each beam require approximately the same number of MU. It was found to be instructive to compare the photoneutron yield per source electron between the two beams as it helped provide an understanding of the physics underlying photoneutron production in both beams.

4.3 Introduction

During external beam radiation therapy treatments that utilize high-energy photons ($\gtrsim$ 8 MV), neutrons are produced via photoneutron reactions between photons and components inside the head of the linear accelerator (linac). Within the treatment room, the production of these unwanted but unavoidable photoneutrons poses a potential risk to both patients, in the form of nontarget dose [3–5], and staff due to activation of in-room materials [6–9]. Compared to other types of ionizing radiation, neutrons have a high relative biological effectiveness for carcinogenesis that varies with neutron energy. Thus, treatment techniques that offer lower photoneutron yield, and thereby reduce the carcinogenic risk posed to patients by photoneutrons, are of interest to the radiation therapy community.

The primary sources of photoneutrons in a linac are the primary collimator, bremsstrahlung target, flattening filter, jaws, and the shielding material surrounding the bending magnet and head [2, 10, 11]. Flattening-filter-free (FFF) beams have been recently incorporated into clinical practice because they offer several advantages compared to conventional, flattened beams. These include the capability to deliver higher dose rates, reduce treatment duration, improve dosimetry, reduce photon leakage from the head, and reduce photoneutron yield [12].

Measurements and Monte Carlo modeling have demonstrated that neutron yield per monitor unit (MU) is significantly reduced when the flattening filter is removed, but the overall shape of the neutron energy spectrum is essentially unchanged [1, 2, 13, 14]. The first evidence of this was published in 2007 by Kry et al. [1], who measured the photoneutron fluence around a Varian 21EX Clinac with and without the flattening filter for an 18 MV beam. They noted that their 18 MV FFF beam used the same monitor chamber calibration as the 18 MV beam and delivered 3.65 cGy of photon dose at d_{max} in water along the central axis per MU, compared to 1 cGy for the 18 MV beam. An average reduction of 20% in the neutron fluence per MU was observed, corresponding to a 76% reduction in the neutron fluence per photon dose at d_{max}. Subsequently, they calculated that a reduction in neutron fluence by 69% could be expected for an IMRT prostate treatment plan delivered with their 18 MV FFF beam instead of the 18 MV beam.

Since the publication of Kry et al. [1], there has been limited experimental data published on (1) modern linear accelerator models, such as the Varian TrueBeam, and on (2) 10 MV photon beams. Modern linacs are of interest because they offer the ability to treat patients using calibrated unflattened beams. 10 MV beams are of interest because they are the lowest energy

photon beams at which photoneutron production is typically a concern. This is an important consideration, for example, when examining the implications of using 10 MV beams to treat patients with implanted cardiac devices. Additionally, IMRT treatments at 10 MV are of interest because of the potential for improved skin-sparing and deeper penetration than treatments at 6 MV.

Motivated by the above, we undertook an investigation to compare the relative photoneutron yield of the clinically-commissioned 10 MV and 10 MV FFF beams of a Varian TrueBeam linear accelerator at our centre. We used a Nested Neutron Spectrometer^{TM} (NNS; Detec Inc., Gatineau Quebec) [15] to measure the photoneutron fluence spectra produced by each beam. To thoroughly examine the physics underlying photoneutron production, the following three measurement objectives were set:

1. Determine if the relative photoneutron yield per MU of the two beams varies with measurement location in the treatment room.

2. Evaluate the effect of the linac jaws on the relative photoneutron yield per MU of the two beams via measurements at two field sizes.

3. Determine which beam produces more photoneutrons per electron striking the linac bremsstrahlung target, and quantify by how much.

In this paper, we report on the methodology we used to achieve our three objectives and on the findings of our investigation. With regard to objective 2, we note that comparisons of the photoneutron yield of flattened and unflattened photon beams as a function of treatment field size have previously been reported in the literature [1, 2, 16]. Also, it is known that there is interplay between photoneutron production in the flattening filter for flattened beams and in the linac jaws for unflattened beams [2]. Our rationale for including a field-size comparison in this work was that it would facilitate understanding of the results of objective 3 given the potentially-unique combination of flattening filter and jaws in the Varian TrueBeam at 10 MV.

4.4 Materials and Methods

4.4.1 The Nested Neutron Spectrometer

The NNS is a neutron spectrometer that operates similarly to a Bonner sphere spectrometer [17], and was previously validated by our group for use in radiation therapy facilities [18]. It consists

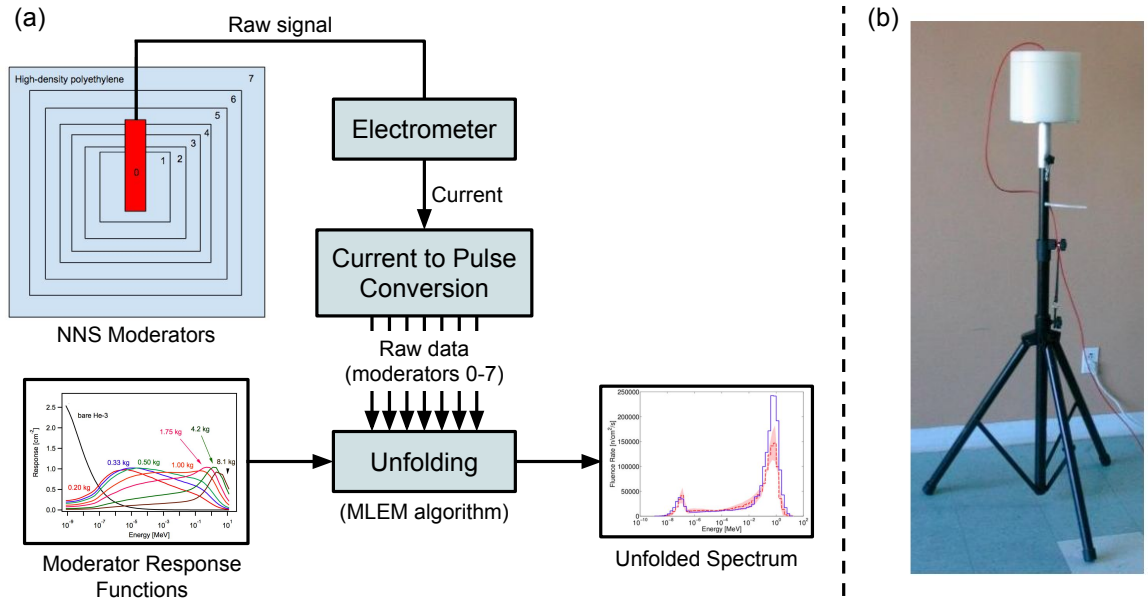

Figure 4.1 The Nested Neutron Spectrometer^{TM} (NNS). (a) Schematic cross section of the cylindrical NNS system that shows the central He-3 detector (red) and seven moderator shells [15]. The signal processing pathway for current-mode operation is shown and includes moderator response functions that were generated by the NNS vendor. (b) Photograph of the NNS on a tripod. The tripod height may be adjusted between measurements to keep the He-3 detector at the same location for all moderator configurations.

of a central He-3 detector and seven cylindrical high-density polyethylene moderator shells assembled in nesting Russian doll fashion. A schematic and photograph of the NNS are shown in Figure 4.1. Thermal neutrons are detected by the He-3 detector through (n,p) reactions with the He-3 gas (Q-value 764 keV). The ambient neutron spectrum is sampled by surrounding the He-3 detector with moderator shells such that ambient neutrons of increasing energy are thermalized and become detectable as successive shells are added.

The He-3 detector can be operated in two modes: pulse-mode and current-mode. Pulse-mode, in which individual neutron events are counted, can only be reliably used in environments with count rates less than 1×10^4 counts per second (cps), and is thus unsuitable for use around radiation therapy linacs where neutron count rates may exceed 1×10^6 cps. For use in radiation therapy environments, the He-3 detector may be operated in current-mode, as described in our earlier publication [18]. In this mode, a neutron-insenstive He-4 detector is used to quantify any photon contribution to the He-3 signal. The resulting photon-subtracted accumulated charge

measurements are converted to neutron count rates using a calibration coefficient of 7.0 fA/cps that was provided by the NNS vendor and previously validated by our group [18].

In this paper, the term "measurement" will be used to describe a complete set of eight He-3 measurements obtained using all seven moderator configurations and the bare detector, with leakage and the photon component removed. For a particular experimental setup, one "measurement" gives rise to one measured spectrum for that setup after spectral unfolding, as described below.

4.4.2 Unfolding the neutron counts per second data

The count rates measured by the NNS for a particular moderator configuration represents a convolution of the ambient neutron fluence spectrum and the NNS response function for that configuration. To obtain the ambient neutron spectrum, the response functions must be unfolded from the cps data. In our research group, unfolding is performed using a custom-developed Maximum-Likelihood Expectation-Maximization (MLEM) algorithm that we validated in our earlier work using reference neutron sources and Monte Carlo modeling [18]. When iterated to convergence, the MLEM algorithm maximises the likelihood of obtaining the measured data $\{m_i\}$ given that the spectrum is $\{n_j\}$, and is described as follows:

$$n_j^{k+1} = \frac{n_j^k}{\sum_{i=1}^{N} a_{ij}} \sum_{i=1}^{N} a_{ij} \frac{m_i}{\sum_{b=1}^{J} a_{ib} n_b^k}. \tag{4.1}$$

Here, the index i spans the number of moderator configurations (N), j and b span the number of energy bins (J) over which the NNS response functions are defined, and k is the iteration index of the MLEM algorithm. Thus, n^{k+1} is the next estimated spectrum of the MLEM algorithm, n^k is the current estimate, a is the response function of the detector, and m is the set of measurements in counts per second. The NNS response functions span thermal to fast neutron energies as shown in Figure 4.1, and thus permit unfolding the entire neutron spectrum of interest in radiation therapy. A step function (high at thermal energies and low onward) is used as the starting spectrum for the unfolding process. Its appropriateness was determined by reconstructing Monte Carlo spectra, as outlined in our previous publication [18].

A stopping criterion must be provided to the MLEM algorithm to terminate the unfolding process. To this end, a number of iterations must be identified that yields completely unfolded spectra with minimal accumulation of noise. In this work, in order to ensure fair comparison

between the FF and FFF beams, the same number of iterations was used for all corresponding 10 MV and 10 MV FFF spectra that were measured under identical experimental conditions.

In our unfolding algorithm, uncertainties in the unfolded spectra are estimated using a Poisson random sampling process. Each count rate measurement is considered as the mean and variance of a Poisson distribution, from which a randomly-sampled measurement may be obtained. Fifty randomly-sampled measurements are obtained in this way and each is unfolded to obtain 50 sampled neutron spectra. The average root mean square difference between the measured spectrum and the sampled spectra is used as the spectrum uncertainty.

4.4.3 Facilities and Experimental Setup

Two photon beams of a Varian TrueBeam linac were used in this study; the 10 MV and 10 MV FFF beams. Both beams were in clinical use, having been commissioned and calibrated in accordance with the AAPM TG-51 protocol such that one MU corresponds to a photon dose delivery of 1 cGy at d_{max} in water on the central axis for a field size of 10×10 cm^2 [19]. All measurements were obtained with gantry rotation of 0°, collimator rotation of 0°, couch rotation of 0°, and a fully-retracted multi-leaf collimator. The sensitive volume of the detector within the NNS was placed at the height of isocentre at for all measurements.

Setup for Objective 1

The first measurement objective was to determine if the relative photoneutron yield per MU between the two beams is dependent on measurement location within the treatment room. Thus, neutron spectral measurements were made for each beam with the NNS placed at three distinct locations: location A at 100 cm from isocentre along the couch and away from the gantry, location B at 200 cm from isocentre also along the couch and away from the gantry, and location C at the maze-room junction. These locations are shown in Figure 4.2. The linac jaws were closed (field size of 0.5×0.5 cm^2 at isocentre) and a photon dose rate of 400 MU/min was used to deliver 200 MU for each of the eight NNS configurations. For simplicity, the same dose rate was used for the two beams.

Setup for Objective 2

The second objective was to evaluate the effect of the linac jaws on the relative photoneutron yield of the two beams. Therefore, an additional measurement was made at location A for

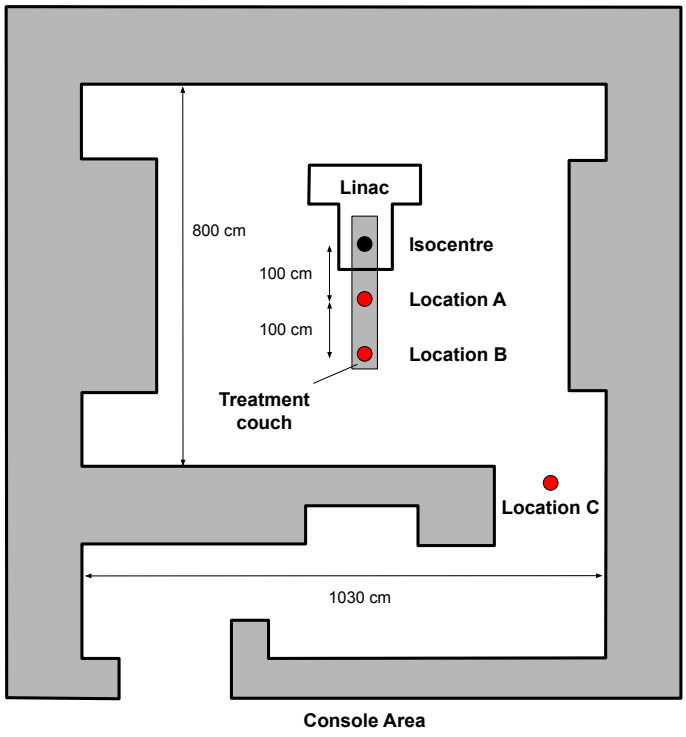

Figure 4.2 Schematic of the doorless treatment room in which neutron spectral measurements were made. Measurement locations are shown in red. Figure not to scale.

both beams with open jaws (field size of 20×20 cm^2) to be compared with those acquired at location A with the jaws closed. The dose rate of 400 MU/min and dose of 200 MU were maintained for this measurement.

Setup for Objective 3

The third and final objective was to determine which beam produces more photoneutrons per electron striking the linac's bremsstrahlung target (i.e. per source electron). An oscilloscope was used to measure the electron pulse width and pulse repetition frequency on the target in order to find dose rates at which the rate of source electrons was the same for both beams. We found that when operated at their maximum dose rates with the dose rate servo turned off, the rates of source electrons were the same. These dose rates were nominally 600 MU/min for the 10 MV beam and 2400 MU/min for the 10 MV FFF beam but they ran approximately 15% higher when the dose rate servo was turned off.

To meet our third objective, measurements were made with the NNS at location A while both beams were operated at their maximum dose rates with the dose rate servo turned off and linac jaws closed. We operated them for the same amount of time (30 seconds for each NNS configuration) to generate the same number of source electrons for each beam.

4.4.4 Measurement Quantities

The counts per second data for each measurement were unfolded to obtain a neutron fluence spectrum. The total fluence (Φ) for each measurement was calculated by integrating over the entire unfolded spectrum. For objectives 1 and 2, in which the same number of MU was used for both the FFF and FF beams, the neutron fluence was normalized per MU. For objective 3, since the absolute number of source electrons for each beam was unknown but equal, the neutron fluence for each beam was normalized per second.

The neutron ambient dose equivalent ($H^*(10)$) was also calculated for each measurement. This was achieved by multiplying the measured fluence in each energy bin of the neutron fluence spectrum by the appropriate neutron fluence-to-dose conversion coefficient provided in ICRP-74 [20], and summing over each bin.

To examine the effect of the flattening filter, the ratio in measured quantities of the FFF to the FF beam, which we refer to as the FF-ratio (FFF/FF), was calculated for all measurements.

Table 4.1 Total neutron fluence per monitor unit (Φ) for the 10 MV and 10 MV FFF beams of the Varian TrueBeam linac.

		Φ (n · cm^{-2} · MU^{-1})		
Location	Field size (cm^2)	10 MV	10 MV FFF	Φ_{FFF}/Φ_{FF}
A	0.5×0.5	$(3.52 \pm 0.08) \times 10^3$	$(2.32 \pm 0.07) \times 10^3$	0.66 ± 0.02
A	20×20	$(3.13 \pm 0.08) \times 10^3$	$(1.94 \pm 0.07) \times 10^3$	0.62 ± 0.03
B	0.5×0.5	$(2.08 \pm 0.07) \times 10^3$	$(1.33 \pm 0.05) \times 10^3$	0.64 ± 0.03
C	0.5×0.5	$(4.0 \pm 0.1) \times 10^2$	$(2.36 \pm 0.09) \times 10^2$	0.58 ± 0.03

Statistical uncertainties in all measurement quantities were calculated by propagating the uncertainty in the unfolded spectra using standard error propagation rules.

4.5 Results

4.5.1 Results for Objective 1: Effect of measurement location on photoneutron yield per MU

The unfolded neutron fluence spectra per MU for the 10 MV and 10 MV FFF beams that were measured at locations A, B, and C are shown in Figure 4.3. Statistical uncertainties are shown as shaded regions around the spectra. A fast neutron peak and thermal neutron peak are seen for both beams under all setup conditions. The total neutron fluence and ambient dose equivalent per MU, as determined from the spectra, are tabulated in Table 4.1 and 4.2. The FF-ratios in these parameters are also provided. It is evident from Figure 4.3 and Table 4.1 that the neutron fluence per MU for the 10 MV FFF beam was consistently lower than the 10 MV beam.

As expected, the total neutron fluence per MU decreased with increasing distance from the linac for both the flattened and unflattened beam. A statistically significant decrease in the FF-ratio at location C compared to locations A and B was observed. This may be attributed to the almost-complete thermalization of the fast neutron peak of the unflattened beam as seen in Figure 4.3(d).

The change in neutron ambient dose equivalent per MU as a function of location, as tabulated in Table 4.2, was found to be consistent with the change in fluence for both beams.

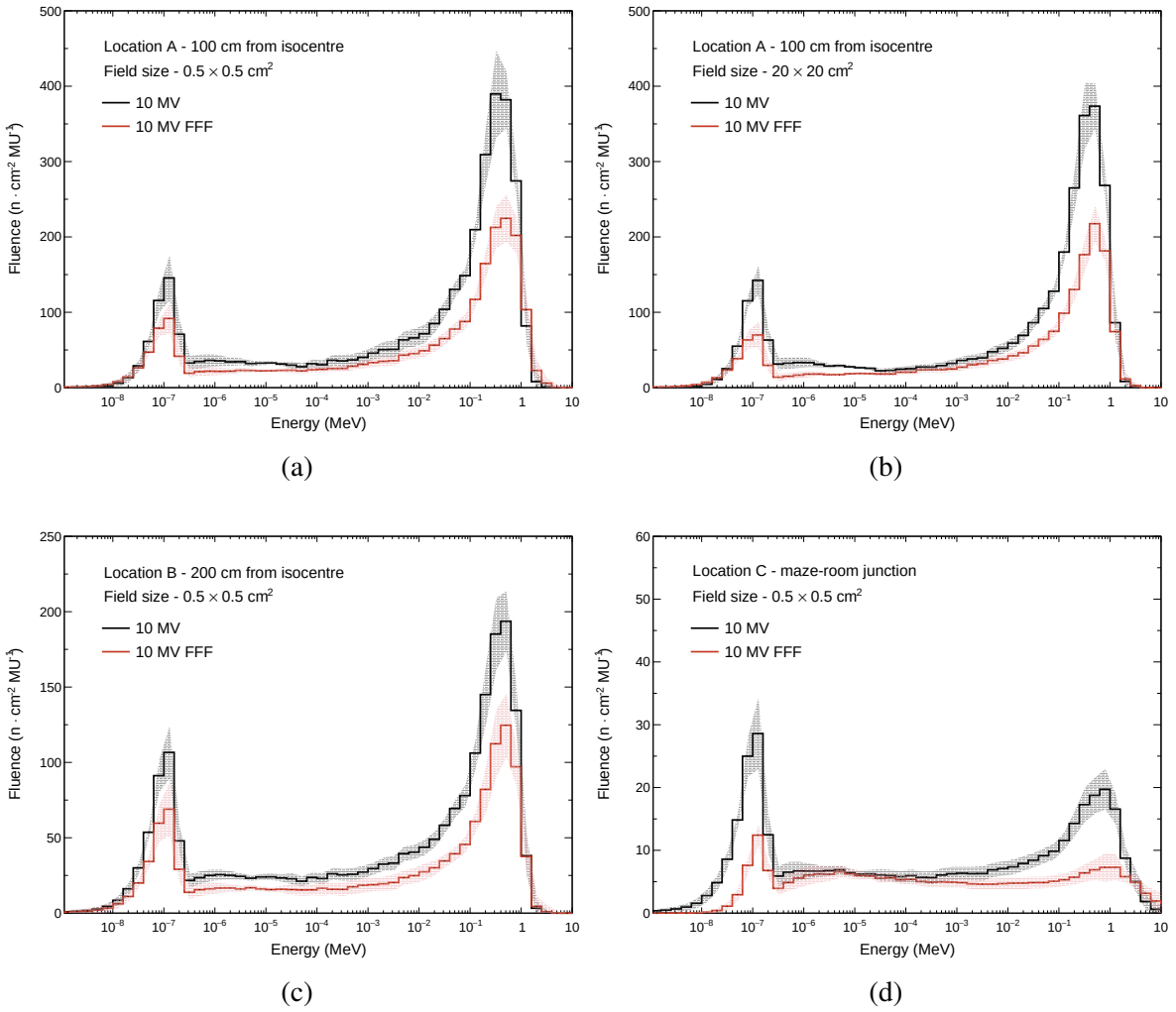

Figure 4.3 Neutron fluence spectra per MU for the 10 MV (black) and 10 MV FFF (red) beams of a Varian TrueBeam linac. Spectra were measured at (a) location A, 100 cm from isocentre along the couch and away from the gantry, with closed linac jaws (field size of 0.5×0.5 cm^2), (b) location A, 100 cm from isocentre along the couch and away from the gantry, with open linac jaws (field size of 20×20 cm^2), (c) location B, 200 cm from isocentre along the couch and away from the gantry, with closed linac jaws, and (d) location C, the maze-room junction with closed linac jaws. The statistical uncertainties in each 10 MV and 10 MV FFF spectrum are shown as the black and red shaded regions respectively.

Table 4.2 Neutron ambient dose equivalent per monitor unit ($H^*(10)$) for the 10 MV and 10 MV FFF beams of the Varian TrueBeam linac.

		$H^*(10)$ (mSv · MU^{-1})		
Location	Field size (cm^2)	10 MV	10 MV FFF	$\frac{H^*(10)_{FFF}}{H^*(10)_{FF}}$
A	0.5×0.5	$(4.1 \pm 0.1) \times 10^{-4}$	$(2.86 \pm 0.09) \times 10^{-4}$	0.69 ± 0.03
A	20×20	$(3.90 \pm 0.08) \times 10^{-4}$	$(2.41 \pm 0.07) \times 10^{-4}$	0.62 ± 0.02
B	0.5×0.5	$(2.05 \pm 0.07) \times 10^{-4}$	$(1.38 \pm 0.06) \times 10^{-4}$	0.67 ± 0.04
C	0.5×0.5	$(3.7 \pm 0.2) \times 10^{-5}$	$(2.0 \pm 0.2) \times 10^{-5}$	0.55 ± 0.06

4.5.2 Results for Objective 2: Effect of the linac jaws on photoneutron yield per MU

Whether the jaws were opened or closed had an observable effect on the measured quantities. As shown in Table 4.1, the FF-ratio in neutron fluence was lower with open jaws than closed jaws at location A, although the two values were within statistical uncertainty. The FF-ratio in neutron ambient dose equivalent per MU was also lower with open jaws, as shown in Table 4.2, but the reduction was statistically significant in this case.

4.5.3 Results for Objective 3: Photoneutron yield per source electron

The unfolded neutron fluence rate spectra obtained at location A for the 10 MV and 10 MV FFF beams with an equal number of source electrons are shown in Figure 4.4. For comparison, the spectra obtained using 400 MU/min at location A with closed linac jaws were renormalized per unit time and are also plotted in Figure 4.4.

The FF-ratios in the fluence rate and ambient dose equivalent rate for the two beams with equal source-electron rates were determined to be $\frac{\dot{\Phi}_{FFF}}{\dot{\Phi}_{FF}} = 2.56 \pm 0.05$ and $\frac{(\dot{H}^*(10))_{FFF}}{(\dot{H}^*(10))_{FF}} = 2.64 \pm 0.05$, respectively. We note that these FF-ratios per source electron are approximately four times larger than the FF-ratios per MU, for which both beams were operated at 400 MU/min at location A. This was expected given the relative increase in dose rate from 400 MU/min to the maximum for each beam ($\frac{400\ MU/min}{400\ MU/min}$ to $\frac{2400\ MU/min}{600\ MU/min}$).

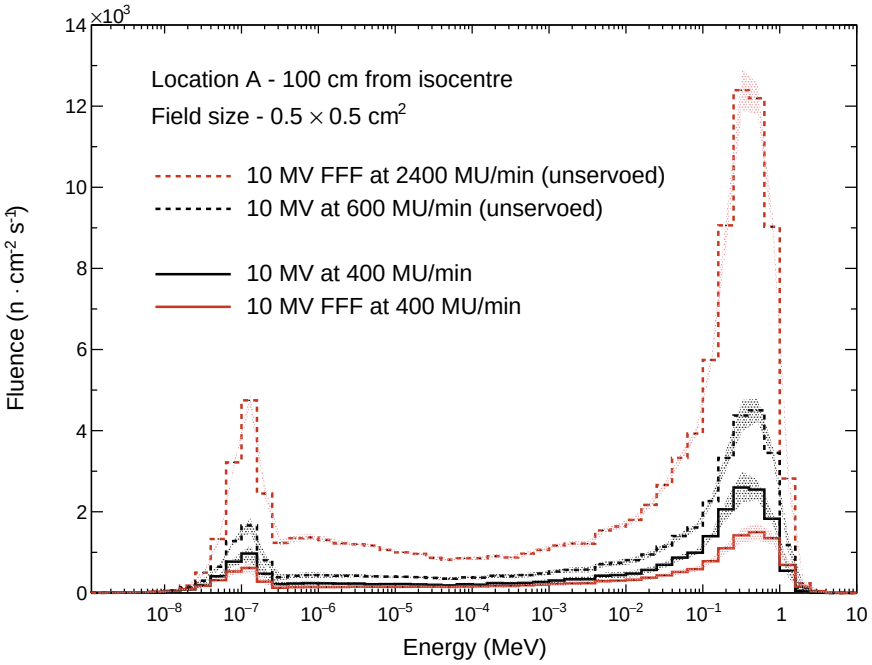

Figure 4.4 Neutron fluence rate spectra for the 10 MV (black) and 10 MV FFF (red) beams of a Varian TrueBeam linac measured at location A, 100 cm from isocentre along the couch and away from the gantry with linac jaws closed. The spectra depicted with dashed lines correspond to an equal number of source electrons and were obtained using the maximum available dose rate of each beam. The spectra depicted with solid lines correspond to an equal number of MU and were presented in Figure 4.3(a). Statistical uncertainties are shown as shaded regions around each spectrum.

4.6 Discussion

To evaluate the consistency of our measured photoneutron yield with existing published data, we compared our neutron ambient dose equivalent measurement at location A with closed linac jaws using the 10 MV beam to the data reported for the 10 MV beam of a Varian Clinac in NCRP 151 at the same location [21]. Our measured value of $(4.1 \pm 0.1) \times 10^{-4}$ mSv/MU corresponds to (41 ± 1) μSv/Gy, which agrees with the published value of 40 μSv/Gy.

4.6.1 Photoneutron yield per MU for the 10 MV and 10 MV FFF beams

In this investigation, it was found that the photoneutron fluence per MU produced by a Varian TrueBeam linac was 34-42% lower for the 10 MV FFF beam than the 10 MV beam. This reduction in neutron fluence per MU for the clinically-commissioned and calibrated unflattened beam is due to the reduction in upstream photon fluence required to produce an MU when the attenuating effect of the flattening filter is removed [1]. Qualitatively, this is consistent with previous experimental and Monte Carlo studies at various photon beam energies for various linac models [1, 2, 13, 14]. The closest point of reference to the present investigation was an abstract published in 2015 by Sawkey and Svatos who simulated the neutron fluence produced by the 10 MV FFF and 10 MV beams of a Varian TrueBeam over a 70 cm radius sphere centered on the linac head [13]. They measured an FF-ratio in neutron fluence per MU of 0.58, which agrees well with our results tabulated in Table 4.1.

Corresponding to the lower neutron fluence for the 10 MV FFF beam, a reduction in neutron ambient dose equivalent of 31-38% was observed at the patient-relevant locations A and B. To assess the potential reduction in neutron dose received by patients through use of the 10 MV FFF beam instead of the 10 MV beam, one must consider the number of MU required to deliver clinically-equivalent treatment plans for the two beams. Chung et al. [22] compared the number of MU requried for equivalent VMAT-SABR (volumetric-modulated arc therapy, stereotactic ablative body radiation therapy) prostate treatment plans using 10 MV and 10 MV FFF beams. They found that the 10 MV FFF plans required 10% more MU than the 10 MV plans on average. Similarly, Stieler et al. [23] found that 8% more MU were required for 6 MV FFF VMAT plans than 6 MV plans to treat multiple brain metastases. However, they also found that 2-4% fewer MU were required for 6 MV FFF IMRT plans than 6 MV plans to treat single brain metastases. Based on a review of the literature, they concluded that flattening-filter-free treatment plans for large volumes or complex plans tend to require more MU than equivalent plans with flattened beams.

Thus, it seems reasonable to expect that approximately the same number or slightly more MU (on the order of 10%) are required for 10 MV FFF treatment plans than 10 MV plans. This does not offset the 31-38% reduction in neutron ambient dose equivalent per MU for the 10 MV FFF beam at locations A and B. An important reduction in neutron dose received by patients treated with the 10 MV FFF beam can therefore be expected, although consideration must be given to the size of the treatment volume and plan complexity. Additionally, the

increase in scattered and leakage photon dose associated with a plan that requires more MU must be considered in order to fully account for the nontarget dose received by patients.

4.6.2 The effect of measurement location on photoneutron yield per MU

Changes to both the unflattened and flattened photoneutron fluence spectra as the NNS was placed further from the linac were qualitatively similar to previous findings by our group at 18 MV [18]. The total neutron fluence for each beam decreased with increasing displacement from isocentre, and the dominant peak in the spectrum transitioned from the fast peak at location A, 100 cm from isocentre, to the thermal peak at location C, at the maze-room junction. This change in the dominant peak of the spectra for both beams was due to thermalization of fast neutrons by the treatment room walls and furnishings [24]. The FF-ratios did not change significantly from one location to the next for all measured quantities. This is consistent with findings in the literature at 10 MV, 15 MV, and 18 MV for measurement locations outside of the treatment field [1, 14].

4.6.3 The effect of the linac jaws on photoneutron yield per MU

Neutron fluence and ambient dose equivalent were found to decrease slightly more for the unflattened beam than the flattened beam when the linac jaws were opened compared to when they were closed. Although the reduction observed in the FF-ratio for the neutron fluence was within statistical uncertainty, the reduction in the FF-ratio for the neutron ambient dose equivalent was found to be statistically significant. The reduction may be attributed to the fact that the neutron fluence to ambient dose conversion coefficients are energy dependent and exhibit a peak around 1 MeV [20]. As seen in Figure 4.3(a) and 4.3(b), the fast peak of the flattened spectrum shifted closer to 1 MeV (from 0.25 MeV to 0.4 MeV) when the jaws were opened compared to when the jaws were closed, while the peak of the unflattened spectrum remained at the same energy.

Physically, this may be explained by examining the relative amount of neutrons produced by the various the components of the linac head. Kry et al. [2] demonstrated, using Monte Carlo modelling, that the linac jaws contribute more to the neutron yield of the unflattened beam than the flattened beam at 18 MV for the Varian 21EX Clinac. This is because without a flattening filter to attenuate the upstream photons, the full neutron-producing potential of the photon beam, which would otherwise be reduced by neutron production in the flattening filter,

is transported to the jaws. The jaws thus play a more important role in generating neutrons for the unflattened beam than the flattened beam. This finding is of particular relevance when interpreting the photoneutron yield per source electron.

4.6.4 Photoneutron production per source electron

The photoneutron fluence per source electron obtained for the 10 MV FFF beam was 2.56 times greater than for the 10 MV beam. Qualitatively similar findings have been reported for 18 MV and 18 MV FFF photon beams by other groups [2, 16]. When the rate of electrons striking the bremsstrahlung target is the same, the difference in photoneutron fluence between the flattened and unflattened beam is simply due to the presence of the flattening filter. Everything else, including the photon fluence upstream of the flattening filter, remains the same. This manifests itself as higher photoneutron production per source electron for the unflattened beam than the flattened beam for two reasons, both of which arise from the fact that the jaws contribute more to photoneutron production in the unflattened beam.

Firstly, the jaws are further downstream in the linac head than the flattening filter. Therefore, neutrons produced in the jaws are less likely to be absorbed before exiting the linac than those produced in flattening filter. Secondly, the material composition of a flattening filter is typically different than that of the jaws [2, 14], with the jaws having a higher photonuclear cross-section. For example, Najem et al. [14] reported that the 10 MV flattening filter of the Varian Clinac is composed of copper, while linac jaws are typically composed primarily of tungsten [1]. The photoneutron cross-section of tungsten has a threshold energy below 10 MeV and is larger than the cross-section of most intermediate-Z metals like copper, which have a threshold energy around 10 MeV [25]. While the material compositions of the TrueBeam's 10 MV flattening filter and jaws are not disclosed by the vendor, we can use the observations from other linac models by the same vendor to postulate that the jaws produce more photoneutrons per photon than the flattening filter in a 10 MV beam.

Although it is of no clinical consequence, we believe that our approach of examining the relative photoneutron production per source electron helps elucidate the underlying physics of photoneutron production in linacs, and allows for comparison of findings obtained using different linacs and different MU calibrations.

4.7 Conclusions

The photoneutron production of a Varian TrueBeam linear accelerator was investigated at 10 MV with and without a flattening filter using a Nested Neutron Spectrometer. It was found that the neutron fluence per MU of the unflattened beam was 34-42% lower than the flattened beam, with minor variation as a function of measurement location and jaw setting. Thus, an important reduction in the neutron dose received by patients can be achieved through use of the 10 MV FFF beam compared to the 10 MV beam, provided that treatment plans for each beam require approximately the same number of MU.

When examined from the perspective of the number of neutrons produced per electron striking the bremsstrahlung target, it was found that the 10 MV FFF beam actually produces 2.56 times more neutrons per source electron than the 10 MV beam. This difference may be attributed to the composition of the jaws and the higher contribution of the jaws to the photoneutron fluence of the unflattened beam than the flattened beam.

4.8 Acknowledgements

We acknowledge the support of the Natural Sciences and Engineering Research Council of Canada (NSERC) (Alexander Graham Bell Canada Graduate Scholarship-Doctoral: L. Montgomery, Discovery Grant: J. Kildea). Partial support for this research was provided by the CREATE Medical Physics Research Training Network grant of the Natural Sciences and Engineering Research Council (Grant number: 432290) and by the Canadian Nuclear Safety Commission (support for student Robert Maglieri). The Nested Neutron Spectrometer used in this investigation was generously provided on loan from the Canadian Nuclear Safety Commission (CNSC). Helpful advice and discussions provided by Stephen Davis (McGill), Susannah Hickling (McGill), Joe Larkin (McGill University Health Centre), Angel Licea (CNSC), and Jacques Dubeau (Detec Inc.) are gratefully acknowledged.

References

[1] S. F. Kry, U. Titt, F. Ponisch, et al. Reduced neutron production through use of a flattening-filter-free accelerator. *International Journal of Radiation Oncology* Biology* Physics*, 68 (4):1260–1264, July 2007. 10.1016/j.ijrobp.2007.04.002.

[2] S. F. Kry, et al. Energy spectra, sources, and shielding considerations for neutrons generated by a flattening filter-free clinac. *Medical Physics*, 35(5):1906–1911, 2008. 10.1118/1.2905029.

[3] S. F. Kry, B. Bednarz, R. M. Howell, et al. AAPM TG 158: Measurement and calculation of doses outside the treated volume from external-beam radiation therapy. *Medical Physics*, 44(10):e391–e429, 2017. 10.1002/mp.12462.

[4] W. D. Newhauser and M. Durante. Assessing the risk of second malignancies after modern radiotherapy. *Nature Reviews Cancer*, 11(6):438–448, 2011. 10.1038/nrc3069.

[5] S. F. Kry, M. Salehpour, D. S. Followill, et al. The calculated risk of fatal secondary malignancies from intensity-modulated radiation therapy. *International Journal of Radiation Oncology* Biology* Physics*, 62(4):1195–1203, 2005. 10.1016/j.ijrobp.2005.03.053.

[6] Y. Z. Wang, M. D. Evans, and E. B. Podgorsak. Characteristics of induced activity from medical linear accelerators. *Medical Physics*, 32(9):2899–2910, 2005. 10.1118/1.2001767.

[7] H. W. Fischer, B. Tabot, and B. Poppe. Comparison of activation products and induced dose rates in different high-energy medical linear accelerators. *Health Physics*, 94(3): 272–278, 2008. 10.1097/01.HP.0000291945.15684.a7.

[8] K. Polaczek-Grelik, B. Karaczyn, and A. Konefał. Nuclear reactions in linear medical accelerators and their exposure consequences. *Applied Radiation and Isotopes*, 70(10): 2332–2339, 2012. 10.1016/j.apradiso.2012.06.021.

[9] J. A. Rawlinson, M. K. Islam, and D. M. Galbraith. Dose to radiation therapists from activation at high-energy accelerators used for conventional and intensity-modulated radiation therapy. *Medical Physics*, 29(4):598–608, 2002. 10.1118/1.1463063.

[10] X. Mao, et al. Neutron sources in the Varian Clinac 21000/23000 medical accelerator calculated by the EGS4 code. *Health Physics*, 72(4):524–529, 1997. 10.1097/00004032-199704000-00003.

[11] A. Zanini, E. Durisi, F. Fasolo, et al. Monte carlo simulation of the photoneutron field in linac radiotherapy treatments with different collimation systems. *Physics in Medicine and Biology*, 49(4):571–582, 2004. 10.1088/0031-9155/49/4/008.

[12] D. Georg, T. Knöös, and B. McClean. Current status and future perspective of flattening filter free photon beams. *Medical Physics*, 38(3):1280–1293, 2011. 10.1118/1.3554643.

[13] D. Sawkey and M. Svatos. Su-e-t-168: Characterization of neutrons from the TrueBeam treatment head. In *Fifty-seventh annual meeting of the American association of physicists in medicine*, volume 42, page 3370. American Association of Physicists in Medicine, 2015.

[14] M. A. Najem, F. A. Abolaban, Z. Podolyák, and N. M. Spyrou. Neutron production from flattening filter free high energy medical linac: A Monte Carlo study. *Radiation Physics and Chemsitry*, 116:176–180, 2015. 10.1016/j.radphyschem.2015.01.040.

[15] J. Dubeau, S. S. Hakmana Witharana, J. Atanackovic, A. Yonkeu, and J. P. Archambault. A neutron spectrometer using nested moderators. *Radiation Protection Dosimetry*, 150(2): 217–222, June 2012. 10.1093/rpd/ncr381.

[16] A. Mesbahi. A Monte Carlo study on neutron and electron contamination of an unflattened 18-MV photon beam. *Applied Radiation and Isotopes : including data, Instrumentation and Methods for use in Agriculture, Industry and Medicine*, 67(1):55–60, 2009. 10.1016/j.apradiso.2008.07.013.

[17] R. L. Bramblett, R. I. Ewing, and T. W. Bonner. A new type of neutron spectrometer. *Nuclear Instruments and Methods*, 9(1):1–12, 1960. 10.1016/0029-554X(60)90043-4.

[18] R. Maglieri, A. Licea, M. Evans, J. Seuntjens, and J. Kildea. Measuring neutron spectra in radiotherapy using the Nested Neutron Spectrometer. *Medical Physics*, 42(11):6162–6169, 2015. 10.1118/1.4931963.

[19] P. R. Almond, P. J. Biggs, B. Coursey, et al. AAPM's TG-51 protocol for clinical reference dosimetry of high-energy photon and electron beams. *Medical Physics Lancaster*, 26: 1847–1870, 1999. 10.1118/1.598691.

[20] International Commission on Radiological Protection. Conversion coefficients for use in radiological protection against external radiation. Technical Report ICRP Publication 74, International Organization for Standardization, 1996.

[21] National Council on Radiation Protection and Measurements. Structural shielding design and evaluation for megavoltage x- and gamma-ray radiotherapy facilities. *NCRP Report*, (151), 2006.

[22] J. Chung, J. Kim, K. Eom, et al. Comparison of VMAT-SABR treatment plans with flattening filter (FF) and flattening filter filter-free (FFF) beam for localized prostate cancer. *Journal of Applied Clinical Medical Physics*, 16(6):302–313, 2015. 10.1120/jacmp.v16i6.5728.

[23] F. Stieler, J. Fleckenstein, A. Simeonova, F. Wenz, and F. Lohr. Intensity modulated radiosurgery of brain metastases with flattening filter-free beams. *Radiotherapy and Oncology*, 109:448–451, 2013. 10.1016/j.radonc.2013.10.017.

[24] J. Pena, et al. Monte Carlo study of Siemens PRIMUS photoneutron production. *Physics in Medicine and Biology*, 50(24):5921–5933, 2005. 10.1088/0031-9155/50/24/011.

[25] International Atomic Energy Agency. Handbook on photonuclear data for applications cross-sections and spectra. Technical report, IAEA-TECDOC-1178, March 2000.

Chapter 5

A novel MLEM stopping criterion for unfolding neutron fluence spectra in radiation therapy

Logan Montgomery, Anthony Landry, Georges Al Makdessi, Felix Mathew, John Kildea

Article published in: *Nuclear Instruments and Methods in Physics Research Section A: Accelerators, Spectrometers, Detectors and Associated Equipment, vol. 985, 2020, 164662. DOI: 10.1016/j.nima.2020.163400*

5.1 Preface

As described in the previous chapter, when unfolding NNS measurements we terminated our MLEM algorithm after a fixed number of iterations defined by an expert user. We identified this step as an undesirable source of subjectivity in the unfolding process. We sought to address this issue by incorporating an objective MLEM stopping criterion that was capable of producing unfolded neutron fluence spectra that have achieved sufficient solution convergence with minimal noise. The manuscript presented in this chapter describes how we developed and validated such a stopping criterion.

5.2 Abstract

The spectrum of secondary neutrons generated by a medical linear accelerator (linac) during high-energy radiation therapy must be accurately determined in order to assess the carcinogenic risk that these neutrons pose to patients. Neutron spectrometers such as the Nested Neutron Spectrometer (NNS) can be used to measure neutron fluence spectra but the raw measured data must be deconvolved (unfolded) with the detector's response functions. The iterative Maximum-Likelihood Expectation-Maximization (MLEM) algorithm can be used to unfold the raw data, however it lacks an objective stopping criterion and produces an increasingly noisy solution as it iterates. In this work, we describe an objective stopping criterion that terminates MLEM unfolding of secondary neutron spectra in radiation therapy after solution convergence but prior to significant accumulation of noise. We validated the robustness of our stopping criterion by using it to unfold NNS measurements spanning a wide range of neutron fluence rates that were acquired around two linacs. We found that these unfolded spectra demonstrate a high level of agreement with the corresponding ideal unfolded spectra (obtained using Monte Carlo simulated spectra) and are relatively free of noise. Thus, use of our stopping criterion increases confidence in experimentally unfolded neutron spectra and can aid in improving carcinogenic risk estimates for patients receiving radiation therapy.

5.3 Introduction

The spectrum of secondary neutrons that is produced during high-energy radiation therapy treatments ($\gtrsim$ 8 MeV) typically spans thermal energies up to the maximum energy of the primary beam [1–3]. These neutrons deliver unwanted dose to patients, induce activation of materials inside the treatment room, and thus pose a carcinogenic risk to both patients [4, 5] and staff [6, 7]. Because the carcinogenic risk associated with neutron radiation is believed to vary widely with energy [8, 9], accurate risk assessment requires accurate determination of the neutron fluence spectrum.

Neutron spectrometers such as the Bonner sphere spectrometer [10] and the Nested Neutron Spectrometer (NNS) [11] can be used to measure neutron fluence spectra, and both have been used in the context of radiation therapy [12, 13]. The raw measurements obtained with these detectors must be deconvolved with the detector's response functions (i.e. unfolded) in order to obtain the spectrum of interest. However, this unfolding problem is typically an

under-determined problem having fewer measured data-points than the desired resolution of the spectrum. Thus, mathematically there are an infinite number of spectra that can satisfy a particular set of measurements obtained with one of these neutron spectrometers.

One method to solve an under-determined problem is to use the iterative Maximum-Likelihood Expectation-Maximization (MLEM) algorithm that was first published in 1977 [14]. MLEM is widely used in positron emission tomography (PET) image reconstruction [15] and has been used to unfold neutron fluence spectra by our group [13, 16] and others [17]. When convolved with the detector's response functions, the MLEM solution (e.g. a voxelized image when applied to PET, or a fluence spectrum when applied to neutron spectrometry) is that which maximizes the likelihood of producing the measured data. However, it has been shown that the level of random noise in the MLEM solution increases as the number of iterations increases [18] due to (i) the ill-posedness of the problem, (ii) Poisson noise inherent to the measurements, and (iii) imperfections in the modeled detector response [19].

A simple method to reduce noise accumulation in the MLEM solution is to apply a de-noising filter after a fixed number of iterations [20]. Another method is to use the maximum *a priori* approach wherein an additional factor is incorporated into the MLEM formulation that penalizes "roughness" in the estimated solution at each iteration [20]. However, both of these require subjective empirical tuning parameters and MLEM must be terminated at an arbitrary and user-dependent number of iterations. One method that does not rely on an empirical tuning parameter, is to introduce a stopping criterion that terminates MLEM when a statistical or heuristic condition has been satisfied.

The objective of this work was to develop an MLEM stopping criterion for unfolding neutron counts-per-second (CPS) data that are measured using the NNS. Specifically, we desired a stopping criterion that terminates unfolding after sufficient convergence to the most likely neutron fluence spectrum but prior to significant accumulation of noise, without requiring subjective user input. Additionally, the stopping criterion must be robust enough to handle the wide range of neutron fluence rates encountered in external beam photon and electron radiation therapy (EBRT; $\sim 10^4$ to 10^6 n·cm^{-2}·s^{-1}). This manuscript describes our method to develop such a stopping criterion and the results of its application.

5.4 Unfolding NNS measurements using MLEM

Use of the NNS in radiation therapy has been described previously by our group [13, 16]. Briefly, the NNS consists of a He-3 proportional counter that is sensitive to thermal neutrons and seven cylindrical high-density polyethylene moderator shells that are assembled in Russian nesting doll fashion. Thermal neutrons undergo neutron capture reactions (n,p) within the He-3 chamber, which are counted to yield a neutron CPS measurement. Neutrons of increasing energy are detected by adding successive moderators around the He-3 chamber such that the entire neutron energy range of interest is sampled.

A set of eight neutron CPS measurements m_i obtained with the NNS must be unfolded with the NNS response functions a_{ij} to yield an estimate of the underlying neutron fluence spectrum n_j. We use the iterative MLEM algorithm to unfold NNS measurements, which is described by:

$$n_j^{k+1} = \frac{n_j^k}{\sum_{i=1}^{I} a_{ij}} \sum_{i=1}^{I} a_{ij} \frac{m_i}{\sum_{b=1}^{J} a_{ib} n_b^k} \tag{5.1}$$

Here, the index i spans the number of NNS moderator configurations ($I = 8$), j and b span the number of energy bins over which the response functions are defined ($J = 52$), and k is the MLEM iteration index. A new spectrum estimate n_j^{k+1} is generated at each iteration by scaling the previous estimate n_j^k by the normalized ratio of the NNS measurements to the MLEM-reconstructed measurements. For succinctness, we denote the MLEM-reconstructed measurements at each iteration as:

$$q_i^k = \sum_{b=1}^{J} a_{ib} n_b^k \tag{5.2}$$

A schematic of the unfolding process is shown in Figure 5.1. It is important to note that the unfolded spectrum is highly dependent on the initial guess spectrum n_j^0 that is input to the MLEM algorithm. Justification of our choice of the step function shown in Figure 5.1 and its application for use in radiation therapy is presented in our previous publication [13].

We cannot directly obtain neutron CPS measurements by operating the He-3 chamber of the NNS as a pulse-counting detector because the high fluence rates encountered in radiation therapy lead to pulse-pileup. Instead, we operate the He-3 chamber in current mode and measure a neutron-induced charge for each moderator configuration using an electrometer. Each charge is first converted to a time-averaged neutron current and subsequently to a neutron

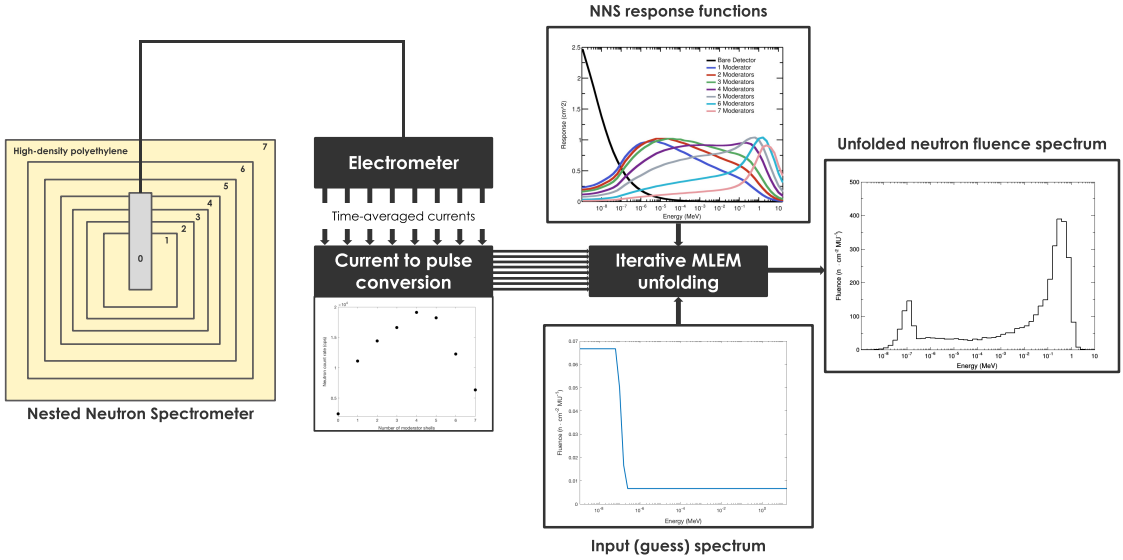

Figure 5.1 Schematic of the NNS unfolding process. A time-averaged neutron current is measured for each moderator shell configuration (eight total) and converted to neutron CPS. These neutron CPS are input into a custom MLEM algorithm along with the NNS response functions and a guess spectrum. The algorithm iterates until terminated, yielding an estimate of the neutron fluence spectrum.

CPS measurement using a calibration coefficient that was provided by the vendor and validated by our group [13].

5.5 The MLEM-STOP method

5.5.1 Application to PET image reconstruction

The MLEM-STOP method [19] relies on the fact that physical measurements naturally contain Poisson noise such that $m_i = \mu_i + \beta_i$, where μ_i are the mean counts of the distributions from which each corresponding m_i is sampled and β_i are Poisson noise terms. Without a stopping criterion, MLEM infinitely iterates to a spectrum $n_j^{k\to\infty}$ that maximizes the likelihood of reconstructing the noisy m_i. We are actually interested in the ground-truth spectrum $\bar{n}_j$ that maximizes the likelihood of obtaining the noise-free measurements μ_i. To this end, consider the following indicator function that may be evaluated at each MLEM iteration k:

$$\mathscr{J}^k = \frac{\sum_{i=1}^{I} \left(m_i - q_i^k\right)^2}{\sum_{i=1}^{I} q_i^k} \tag{5.3}$$

After the initial iteration, $\mathscr{J}^k$ has a positive value whose magnitude depends on the guess spectrum n_j^0. As the iterations proceed, the reconstructed measurements converge to the noisy measurements ($q_i^k \to m_i$) such that $\mathscr{J}^k \to 0$. At some intermediate iteration number, the reconstructed measurements may equal the noise-free measurements ($q_i^k = \mu_i$). It is straightforward to show that $\mathscr{J}^k \approx 1$ when this occurs because the expectation value of the mean square deviation (MSD) between a noisy measurement m_i sampled from a Poisson distribution and the mean μ_i is:

$$E\left[(m_i - \mu_i)^2\right] = \mu_i \tag{5.4}$$

The basis of MLEM-STOP is thus to set a threshold value, $\mathscr{J}_t = 1$, and terminate unfolding when $\mathscr{J}^k \leq \mathscr{J}_t$. At subsequent iterations it is increasingly likely that the noise inherent to each measurement (β_i) is reconstructed rather than the true noise-free measurement (μ_i) from which the noisy measurement was sampled, which leads to noise in the unfolded spectrum.

Ben Bouallègue *et al* applied this method to reconstructing images from artificial PET datasets and demonstrated promising results [19]. For each dataset, they compared the MLEM-STOP estimate with (i) a conventional estimate obtained using a fixed number of iterations and (ii) an ideal MLEM estimate. The ideal MLEM estimates were obtained by terminating reconstruction of each dataset when the root mean square error (RMSE) between the reconstructed image and the corresponding ground-truth artificial image was minimized. In terms of noise content and resolution, the MLEM-STOP estimates were better than the conventional (fixed iteration) estimates and very similar to the ideal estimates.

5.5.2 Application to neutron spectral unfolding

We applied the MLEM-STOP criterion to unfolding neutron CPS measurements obtained with the NNS. However, we found the use of $\mathscr{J}_t = 1$ unsuitable because the rate of MLEM convergence (i.e. the rate at which $m_i/q_i^k \to 1$) is independent of measurement magnitude, but the rate at which $\mathscr{J}^k \to 1$ is not (as explained in the Appendix). As a result, we found that $\mathscr{J}^k > \mathscr{J}_t = 1$ for all k when unfolding high magnitude measurements, which meant that the stopping criterion was never satisfied. Also, when unfolding low magnitude measurements,

we found that the stopping criterion was satisfied too early, resulting in spectra that had not sufficiently converged. Thus, we developed a modified MLEM-STOP method that applied well to measurements of varying magnitude that result from neutron fluence rates, $\dot{\Phi}$, of approximately 10^4 to 10^6 n·cm^{-2}·s^{-1}.

5.6 A modified MLEM-STOP method

This section explores the core idea of our modified MLEM-STOP method; that there exists an optimal average measurement magnitude $\bar{m}_{\text{ideal}}$ (and corresponding neutron fluence) at which the $\mathscr{J}_t = 1$ stopping criterion best applies. We describe how we determined $\bar{m}_{\text{ideal}}$ using ideal unfolded spectra and then capitalized on the linearity of MLEM to establish a new stopping criterion that may be applied when unfolding measurements spanning a broad range of magnitudes.

5.6.1 Ideal unfolded spectra

As described by Ben Bouallègue *et al* [19], the ideal unfolded estimate $n_j^{k_{\text{ideal}}}$ of the ground-truth spectrum $\bar{n}_j$ is determined by calculating the root mean square error (RMSE) between $\bar{n}_j$ and the MLEM estimate n_j^k at each iteration:

$$\text{RMSE}^k = \sqrt{\frac{\sum_{j=1}^{J}\left(\bar{n}_j - n_j^k\right)^2}{J}} \tag{5.5}$$

The ideal unfolded spectrum $n_j^{k_{\text{ideal}}}$ is obtained when the RMSE is minimized and represents an ideal compromise between solution convergence and noise. Note that RMSE can only be calculated if the ground-truth is known and thus minimization of RMSE cannot be used experimentally as a stopping criterion.

In this work, we required $n_j^{k_{\text{ideal}}}$ for multiple spectra spanning a wide range of neutron fluence in order to determine the optimal measurement magnitude $\bar{m}_{\text{ideal}}$ at which the $\mathscr{J}_t = 1$ criterion best applies. As described in our previous publication on validating the NNS for use in radiation therapy [13], we simulated and experimentally measured the photoneutron fluence spectra produced by the 18 MV beam of a Varian Clinac 21EX at four locations in the treatment room for which the neutron fluences varied significantly. These locations are shown in Figure 5.2(a).

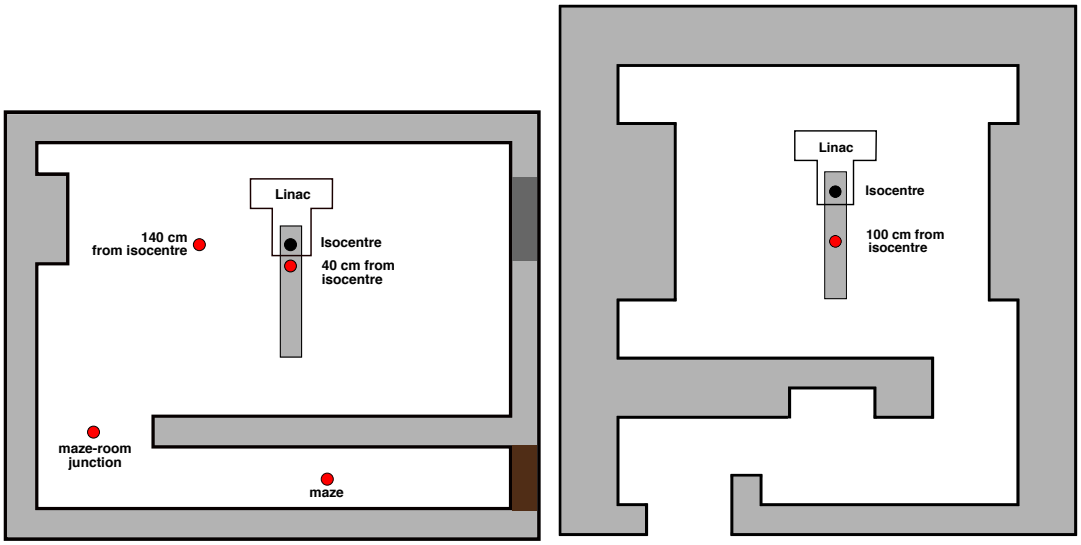

(a) (b)

Figure 5.2 Schematics of the radiation therapy treatment rooms in which neutron spectral measurements were made. Measurement locations are indicated in red. Figures not to scale. (a) Treatment room housing the Varian Clinac 21EX with a door. Measurements were used to develop and validate our novel stopping criterion. (b) Doorless treatment room housing the Varian Truebeam. Measurements were used to further test our stopping criterion.

The simulations were performed using the Monte Carlo modeling package MCNP6 [21] with validated in-house models of the linac (including accelerator components and shielding) and the treatment room. In the present work, we assumed that each simulated spectrum was equivalent to the ground-truth spectrum $\bar{n}_j$ at the corresponding location. The experimental $n_j^{k_{\text{ideal}}}$ was then determined for each of the four NNS measurement sets by calculating the RMSE between the simulated ground-truth and the reconstructed experimental spectrum at each MLEM iteration (using Equation 5.5), and terminating when minimized.

5.6.2 A new stopping criterion

For each of the four datasets for which we determined $n_j^{k_{\text{ideal}}}$, we calculated the mean deviation (MD) between the experimental measurements and their corresponding reconstructed measurements at the ideal number of iterations ($q_i^{k_{\text{ideal}}}$):

$$\text{MD} = \frac{\sum_{i=1}^{I} \left| m_i - q_i^{k_{\text{ideal}}} \right|}{I} \tag{5.6}$$

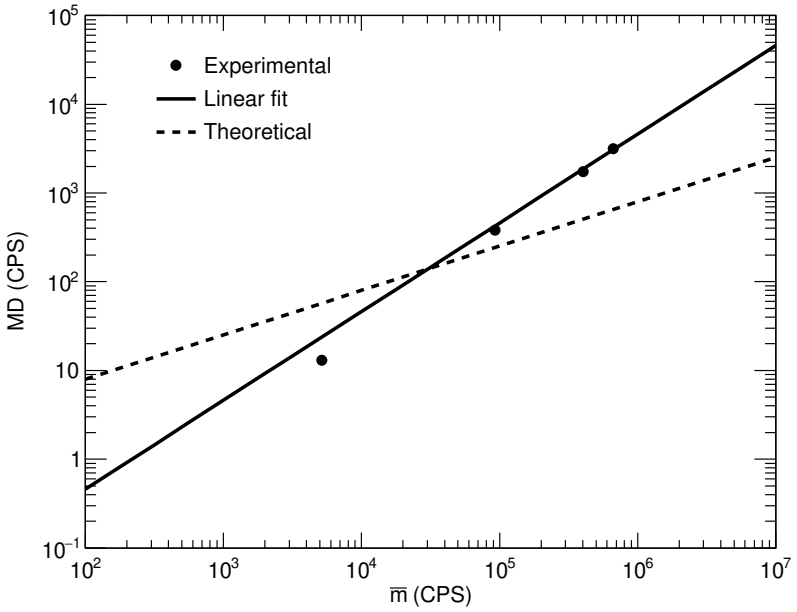

Figure 5.3 Comparison of the mean deviation (MD) between NNS measurements and MLEM reconstructed measurements (data points), and the expectation value of the MD between the mean and sampled values of a Poisson distribution (dashed line), as a function of mean neutron CPS. The solid line represents a linear fit through the origin to the experimental MLEM data.

We plotted the MD for each dataset as a function of the average measurement magnitude (i.e. $\bar{m} = \sum_{i=1}^{I} {}^{m_i}/_{I}$), as shown in Figure 5.3. As previously stated, the rate of MLEM convergence is independent of measurement magnitude and consequently the MD between measurements and their reconstructions is linear with respect to measurement magnitude. Thus, a linear least-squares regression through the origin was performed on these four data points, the result of which is shown as the solid line in Figure 5.3. This fitted line represents the level of MLEM convergence attained at the ideal number of iterations as a function of $\bar{m}$. Note that we forced a zero y-intercept because otherwise the regression produced a negative intercept that erroneously implies a negative MD for data with low $\bar{m}$.

This result was compared with the principle assumption of the MLEM-STOP method, namely that $q_i^k \to \mu_i$ at some k. The expectation value of the MD between the mean of a Poisson distribution and values sampled from the distribution is shown as the dotted line in Figure 5.3 and is calculated by [22]:

$$\mathrm{MD} = \frac{2e^{-\bar{m}}\bar{m}^{\bar{m}+1}}{\bar{m}!} \tag{5.7}$$

The point where the two curves in Figure 5.3 overlap is the optimal magnitude ($\bar{m}_{\mathrm{ideal}} \approx 30\,000 \cdot$CPS) at which the ideal level of MLEM convergence is aligned with the assumption of MLEM-STOP. This leads to three possible scenarios:

1. If $\bar{m} = \bar{m}_{\mathrm{ideal}}$, MLEM converges to the ideal unfolded spectrum $n_j^{k_{\mathrm{ideal}}}$ around when $\mathscr{J}^k = \mathscr{J}_t = 1$.

2. If $\bar{m} > \bar{m}_{\mathrm{ideal}}$, MLEM converges to $n_j^{k_{\mathrm{ideal}}}$ at some point when $\mathscr{J}^k > \mathscr{J}_t = 1$ because the ideal experimental MD is greater than the theoretical expectation.

3. If $\bar{m} < \bar{m}_{\mathrm{ideal}}$, MLEM converges to $n_j^{k_{\mathrm{ideal}}}$ at some point when $\mathscr{J}^k < \mathscr{J}_t = 1$ because the ideal experimental MD is less than the theoretical expectation.

These scenarios clarify and quantify our earlier findings that MLEM-STOP does not apply well to high magnitude measurements (never reaches $\mathscr{J}^k = \mathscr{J}_t = 1$) nor to low magnitude measurements (insufficient convergence when $\mathscr{J}^k = \mathscr{J}_t = 1$).

Fortunately, since the rate of MLEM convergence is independent of $\bar{m}$, one can simply scale any set of measurements such that $\bar{m} = \bar{m}_{\mathrm{ideal}}$ by multiplying by $\bar{m}_{\mathrm{ideal}}/\bar{m}$. These scaled measurements can then be unfolded using MLEM-STOP, which is terminated when $\mathscr{J}^k \leq \mathscr{J}_t = 1$. Following this approach, the final unfolded spectrum must be scaled back by the inverse ratio, $\bar{m}/\bar{m}_{\mathrm{ideal}}$. An alternative approach that is simpler than scaling the measurements is to specify a new threshold value for each unique dataset:

$$\mathscr{J}_t = \frac{\bar{m}}{\bar{m}_{\mathrm{ideal}}} \tag{5.8}$$

and terminate when $\mathscr{J}^k \leq \mathscr{J}_t = \bar{m}/\bar{m}_{\mathrm{ideal}}$. This latter approach is more succinctly stated as a stopping criterion and was adopted as our modified MLEM-STOP criterion.

5.6.3 Uncertainty calculations

A statistical uncertainty in each neutron fluence spectrum obtained using the modified MLEM-STOP method was estimated using a random sampling process that was adapted from the method described in our previous publication [13]. All eight measurements m_i in an NNS

Table 5.1 The number of iterations, k_{STOP}, required to satisfy our modified MLEM-STOP criterion for all experimental NNS datasets considered in this work. Datasets are grouped according to their purpose and within each group are sorted in order of decreasing neutron fluence rate $\dot{\Phi}$. The number of iterations, k_{ideal}, corresponding to the ideal unfolded spectra are provided for the 18 MV datasets used to develop and validate our method.

Purpose	Beam energy	Location	$\dot{\Phi}\ \left(\text{n}\cdot\text{cm}^{-2}\cdot\text{s}^{-1}\right)$	k_{ideal}	k_{STOP}
Validation	18 MV	40 cm from isocentre	$(1.23\pm0.02)\times10^{6}$	3687	3699
	18 MV	140 cm from isocentre	$(7.64\pm0.07)\times10^{5}$	2742	2113
	18 MV	maze-room junction	$(1.90\pm0.01)\times10^{5}$	2059	1674
	18 MV	maze	$(1.22\pm0.01)\times10^{4}$	5632	1182
Testing	15 MV	100 cm from isocentre	$(2.56\pm0.03)\times10^{5}$	N/A	3873
	10 MV	100 cm from isocentre	$(2.18\pm0.03)\times10^{4}$	N/A	3879
	16 MeV	100 cm from isocentre	$(1.36\pm0.01)\times10^{4}$	N/A	2805

dataset were set as the mean of a Poisson distribution and each distribution was subsequently sampled 100 times to yield 100 pseudo-measurement sets. All of the pseudo-measurement sets were then unfolded using the modified MLEM-STOP method. The root mean square difference between the experimental unfolded spectrum and the 100 unfolded pseudo-spectra was then set as the spectrum uncertainty.

5.7 Results

5.7.1 Validation: comparison with ideal unfolded spectra

To validate our modified MLEM-STOP method, we applied it to all four NNS datasets for which $n_j^{k_{\text{ideal}}}$ and $\bar{n}_j$ were known (i.e. the measurements made at the locations indicated in Figure 5.2(a)). The resulting MLEM-STOP spectra are plotted alongside $n_j^{k_{\text{ideal}}}$ and $\bar{n}_j$ in Figure 5.4. The ideal number of iterations (k_{ideal}) and the number of iterations determined for use in MLEM-STOP, denoted k_{STOP}, are provided in Table 5.1.

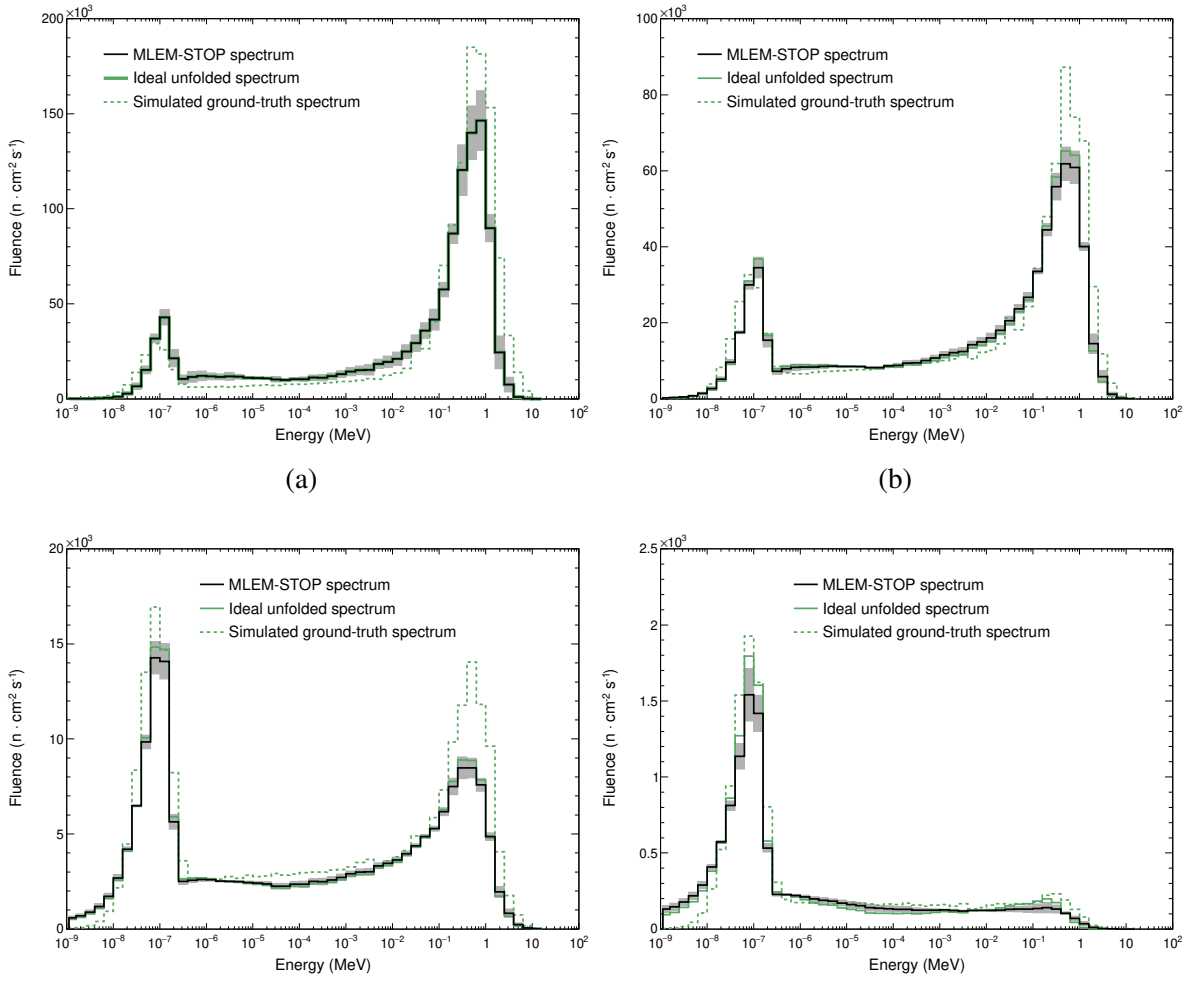

Figure 5.4 Comparison of neutron fluence spectra obtained by unfolding NNS measurements using our modified MLEM-STOP method (solid black) with corresponding ideal unfolded spectra (solid green) and Monte Carlo simulated spectra that were assumed to be equivalent to the ground-truth (dashed green). Spectra were obtained using the 18 MV beam of a Varian Clinac at four locations around the treatment room; (a) at 40 cm from isocentre, (b) at 140 cm from isocentre, (c) at the maze-room junction, and (d) in the maze.

5.7.2 Testing: comparison with a conventional unfolding approach

To further test our modified MLEM-STOP criterion, we applied it to the unfolding of three NNS datasets for which $\bar{n}_j$ and thus $n_j^{k_{\text{ideal}}}$ were unknown. These datasets comprised NNS measurements at 100 cm from isocentre along the treatment couch of a Varian Truebeam linac, as indicated in Figure 5.2(b). Measurements for the 15 MV and 10 MV photon beams as well as the 16 MeV electron beam were obtained. The unfolded spectra are shown in Figure 5.5 and the corresponding k_{STOP} values are provided in Table 5.1.

In the absence of ground-truth, we compared each MLEM-STOP spectrum with two spectra obtained by terminating unfolding at fixed iteration numbers that serve as empirical upper and lower limits, between which unfolding should usually be terminated. The upper limit was set as $k_{\text{upper}} = 15000$ because we observed that significant noise, in the form of adjacent bins of alternating high and low magnitude, is typically visible in the intermediate energy region ($\sim$ 1 eV to 10 keV) at this number of iterations and above. The lower limit was set as $k_{\text{lower}} = 1000$ because with fewer iterations the fast and thermal peaks are typically poorly-defined, which indicates insufficient convergence. These peaks are known to be well-defined for secondary neutron spectra in photon and electron EBRT, as widely reported in the literature and observed in our own Monte Carlo simulated spectra [1, 2, 13]. The spectra obtained at these upper and lower limits are shown alongside the MLEM-STOP spectra in Figure 5.5. Note that the Poisson sampling approach described in Section 5.6.3 was also used to estimate uncertainties for the upper and lower limit spectra with the exception that the corresponding fixed number of iterations was used as the stopping criterion for each set of pseudo-measurements (instead of MLEM-STOP).

To demonstrate the dosimetric impact of the spectral differences shown in Figure 5.5, the neutron ambient dose equivalent rate, $\dot{H}^*(10)$, was calculated for each MLEM-STOP spectrum as well as for the conventional upper and lower limits. $\dot{H}^*(10)$ was calculated by multiplying the measured fluence rate in each energy bin by the appropriate neutron fluence-to-dose conversion coefficient provided in ICRP-74 [23] and by summing over all bins. The resulting $\dot{H}^*(10)$ values are provided in Table 5.2. Uncertainties were set as the root mean square deviation between the experimental $\dot{H}^*(10)$ value and the pseudo-$\dot{H}^*(10)$ values calculated for all 100 pseudo-spectra that were generated for the corresponding spectral uncertainty calculations.

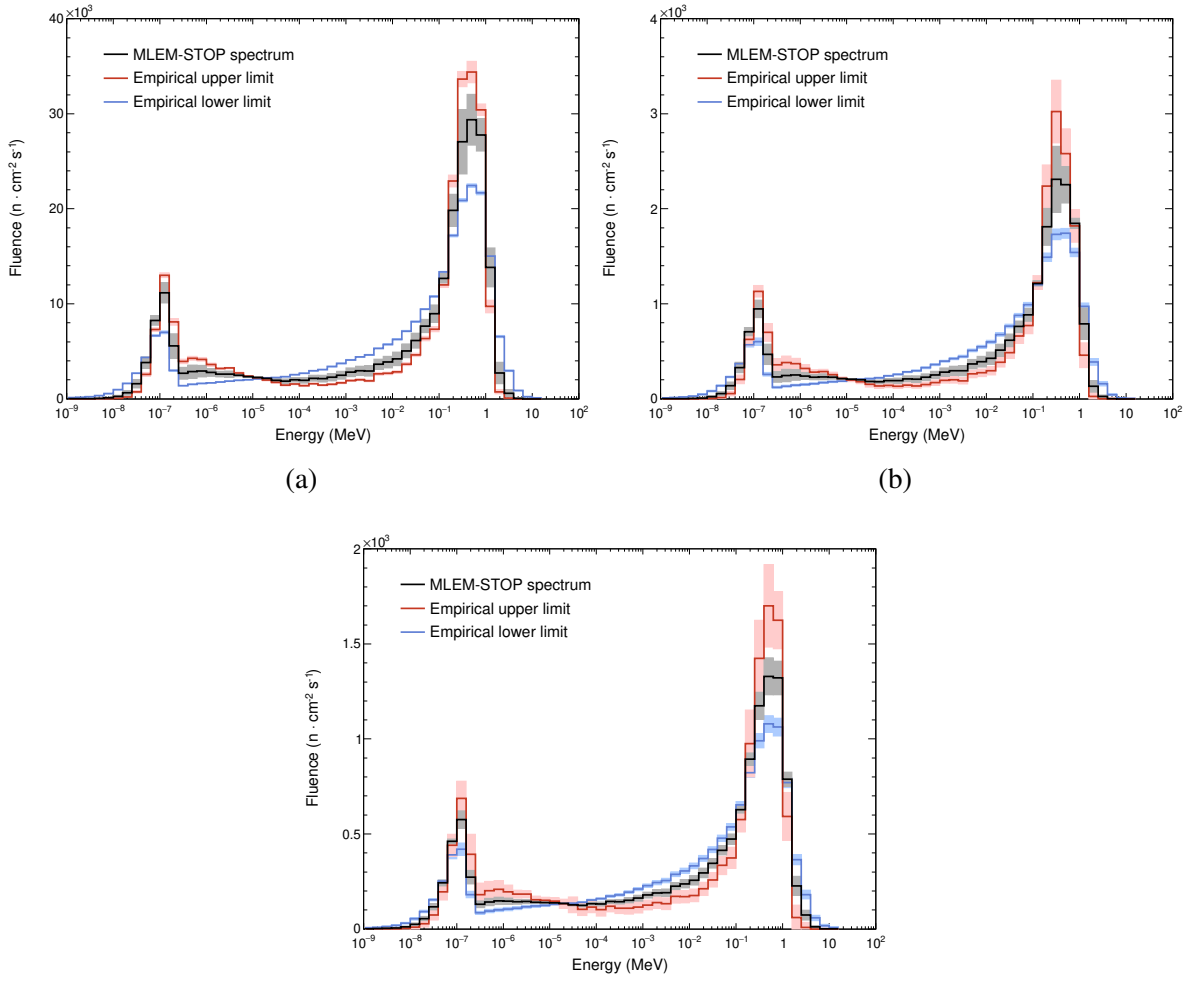

Figure 5.5 Comparison of neutron fluence spectra obtained by unfolding NNS measurements using our modified MLEM-STOP method (black) with unfolded spectra using fixed iteration numbers corresponding to empirical upper (red) and lower (blue) limits. An upper limit of $k_{\text{upper}} = 15000$ iterations and a lower limit of $k_{\text{lower}} = 1000$ iterations were used. Spectra were measured at 100 cm from isocentre along the treatment couch for two photon beams and one electron beam of a Varian Truebeam linac: (a) 15 MV, (b) 10 MV, and (c) 16 MeV.

Table 5.2 Neutron ambient dose equivalent rates, $\dot{H}^*(10)$, associated with unfolded neutron fluence spectra obtained using MLEM-STOP versus empirical upper and lower iteration limits.

	$\dot{H}^*(10)$ (mSv · hr^{-1})		
Beam energy	Empirical lower limit	MLEM-STOP	Empirical upper limit
15 MV	124.7 ± 0.7	131 ± 2	135 ± 1
10 MV	9.20 ± 0.07	9.7 ± 0.2	10.1 ± 0.1
16 MeV	6.31 ± 0.03	6.6 ± 0.1	6.84 ± 0.07

5.8 Discussion

Our modified MLEM-STOP method utilizes a statistical stopping criterion that terminates iterative MLEM unfolding of secondary neutron fluence spectra in EBRT without subjective user input. The spectra obtained with this method demonstrate a high level of agreement with the corresponding ideal unfolded spectra (obtained through comparison with Monte Carlo simulated spectra), as shown in Figure 5.4. This serves as validation of our method for neutron fluence spectra ranging from $\dot{\Phi} \approx 10^4$ to 10^6 n·cm^{-2}·s^{-1}. It is important to note that the experimental unfolded spectra (MLEM-STOP and ideal) do not agree completely with the simulated spectra. This could be due to inaccuracies in the Monte Carlo models, limitations of the resolution of NNS measurements, and the ill-posed nature of the unfolding problem. However, this does not undermine our finding that MLEM-STOP is able to generate spectra that are almost entirely within uncertainty of the ideal unfolded spectra.

The modified MLEM-STOP approach was also applied to NNS measurements for which the ground-truth spectra were unknown; the results of which are shown in Figure 5.5. These spectra appear reasonable because of the well-defined fast and thermal peaks (demonstrating sufficient convergence) as well as the limited presence of visible noise in the intermediate energy region. We do not have simulated ground-truth spectra to compare with because the specifications of the beam shaping assembly of the Varian Truebeam linac is not disclosed by the vendor, and we are thus unable to model it for Monte Carlo simulations. However, through comparison with the empirical upper and lower limits, the MLEM-STOP spectra appear to satisfy our goal to produce spectra that have sufficiently converged with minimal noise.

The effect of the spectral shape (and thus iteration number) on the dosimetric quantity of interest, $\dot{H}^*(10)$, is elucidated in Table 5.2. For all three datasets, the ambient dose equivalent

rate associated with the MLEM-STOP spectrum is significantly different from both the empirical upper and lower limits. These differences arise from the tendency of the dominant peak (in these cases, the fast peak) to increase in magnitude as MLEM iterates. This finding, coupled with the fact that the fluence-to-dose conversion coefficients are peaked around 1 MeV [23], results in the observed dosimetric discrepancies. Although there are no ground-truth $\dot{H}^*(10)$ values to compare with, the MLEM-STOP estimates are a good compromise between the upper and lower limits.

As shown in Table 5.1, the fluence rates of the spectra with no known ground-truth are within the range spanned by the 18 MV spectra with known ground-truth. We anticipate that the modified MLEM-STOP method is applicable for any set of measurements wherein each measurement m_i is governed by Poisson statistics because MLEM behaves linearly with measurement magnitude. Regarding the unfolding of measurements acquired using the NNS specifically, there may be experimental limitations at low fluence rates due to insufficient signal relative to the noise and at high fluence rates due to loss of linearity of the He-3 chamber.

Finally, the dynamic threshold, $\mathscr{J}_t$, of our modified MLEM-STOP method is calculated using $\bar{m}_{\text{ideal}}$ as shown in Equation 5.8 and thus the MLEM-STOP spectra are sensitive to the fitting procedure used to determine $\bar{m}_{\text{ideal}}$. Furthermore, we believe our method may be applied generally to other "classes" of spectra having significantly different shapes. However, if a different guess spectrum is required, or if the level of convergence associated with ideal unfolded spectra differs significantly from the fitted curve of Figure 5.3, then a new calibration should be performed to determine $\bar{m}_{\text{ideal}}$. With knowledge of a few ground-truth spectra, the procedure of Section 5.6.2 could then be used to determine $\bar{m}_{\text{ideal}}$ for the "class" of spectra under consideration.

Our software for unfolding and plotting neutron spectra, including our modified MLEM-STOP algorithm, is provided as open-source software on GitHub [24].

5.9 Conclusions

We have developed a statistical stopping criterion to terminate iterative MLEM unfolding of secondary neutron spectra in external beam photon and electron radiation therapy as measured using the Nested Neutron Spectrometer. This stopping criterion is based on the MLEM-STOP methodology published for PET image reconstruction by Ben Bouallègue et al. [19], and is designed to terminate unfolding after sufficient solution convergence but prior to significant

accumulation of noise. Modifications to the published method were required to accommodate the wide range of neutron fluence rates encountered in radiation therapy. Our modified approach uses a dynamic threshold value that is calculated for each unique set of measurements. We obtained good agreement between the spectra unfolded using our modified MLEM-STOP method and the ideal unfolded spectra obtained using knowledge of the underlying ground-truth spectra. When applied to datasets with unknown ground-truth, we found that the MLEM-STOP spectra qualitatively met the theoretical goals of the method. This method should be generally applicable to measurements of any magnitude but may require a unique calibration using known ground-truth for spectra having distinct spectral shapes and alternative guess input spectra.

5.10 Acknowledgements

This work was supported by the Natural Sciences and Engineering Research Council of Canada (NSERC) (Alexander Graham Bell Canada Graduate Scholarship-Doctoral: L. Montgomery, Discovery Grant: J. Kildea). Partial support for this research was provided by the CREATE Medical Physics Research Training Network grant of the Natural Sciences and Engineering Research Council of Canada (Grant number: 432290) and by the Canadian Nuclear Safety Commission (CNSC). A Nested Neutron Spectrometer used in this investigation was generously provided on loan from the CNSC. Logistical support provided by the Prince Edward Island Cancer Treatment Centre was invaluable for this work. Insightful advice and discussions provided by Jacques Dubeau (Detec Inc.) and Angel Licea (CNSC) are gratefully appreciated.

5.11 Appendix: Incompatible convergence rates

This appendix demonstrates why the rate at which ${}^{m_i}/_{q_i^k} \to 1$ is independent of measurement magnitude but the rate at which $\mathscr{J}^k \to 1$ is not. Consider MLEM unfolding of an arbitrary set of NNS measurements, m_i, provided in Table 5.3. The reconstructed measurements, q_i^k, after $k = 2784$ iterations of MLEM are also provided in Table 5.3. When these data are used to calculate $\mathscr{J}^k$ via Equation 5.3, a result of $\mathscr{J}^k = 1$ is obtained.

Now consider another set of eight NNS measurements, M_i such that $M_i = 10m_i$. When these are unfolded using the same number of iterations ($k = 2784$) the resulting MLEM-reconstructed measurements, Q_i^k, are equal to $10 \times q_i^k$ as shown in Table 5.3. Thus, the ratios ${}^{m_i}/_{q_i^k}$ and ${}^{M_i}/_{Q_i^k}$ are equal, which indicates that the rate of MLEM convergence is independent of measurement

Table 5.3 Comparison between the ratio of measurements to MLEM-reconstructed measurements at $k = 2784$ iterations for an arbitrary NNS measurement set m_i and an artificial measurement set M_i such that $M_i = 10m_i$

# moderators	m_i (CPS)	q_i^k (CPS)	$\frac{m_i}{q_i^k}$	M_i (CPS)	Q_i^k (CPS)	$\frac{M_i}{Q_i^k}$
0	2129	2132	0.9988	21290	21320	0.9988
1	10340	10265	1.0073	103400	102650	1.0073
2	13207	13228	0.9984	132070	132280	0.9984
3	15457	15560	0.9934	154570	155600	0.9934
4	17635	17721	0.9951	176350	177210	0.9951
5	17035	16881	1.0091	170350	168810	1.0091
6	11476	11431	1.0039	114760	114310	1.0039
7	6156	6217	0.9903	61560	62170	0.9903

magnitude. However, when M_i and Q_i^k are used to calculate $\mathscr{J}^k$ at $k = 2784$, a result of $\mathscr{J}^k = 5.7$ is obtained. This occurs because calculation of $\mathscr{J}^k$ involves calculating mean square differences between two values, which increases with the magnitude of the values even if their relative values are constant.

References

[1] R. M. Howell, S. F. Kry, E. Burgett, N. E. Hertel, and D. S. Followill. Secondary neutron spectra from modern Varian, Siemens, and Elekta linacs with multileaf collimators. *Medical Physics*, 36(9):4027–4038, 2009. 10.1118/1.3159300.

[2] H. R. Vega-Carrillo and L. H. Pérez-Landeros. Electroneutrons around a 12 MV LINAC. In *13 International Symposium: Sociedad Mexicana de Irradiacion y Dosimetria*, pages 26–29, 2012.

[3] R. M. Howell and E. A. Burgett. Secondary neutron spectrum from 250 MeV passively scattered proton therapy: Measurement with an extended-range Bonner sphere system. *Medical Physics*, 41(9):092104, 2014. 10.1118/1.4892929.

[4] S. F. Kry, et al. AAPM TG 158: Measurement and calculation of doses outside the treated volume from external-beam radiation therapy. *Medical Physics*, 44(10):e391–e429, 2017. 10.1002/mp.12462.

[5] W. D. Newhauser and M. Durante. Assessing the risk of second malignancies after modern radiotherapy. *Nature Reviews Cancer*, 11(6):438–448, 2011. 10.1038/nrc3069.

[6] Y. Z. Wang, M. D. C. Evans, and E. B. Podgorsak. Characteristics of induced activity from medical linear accelerators. *Medical Physics*, 32(9):2899–2910, 2005. 10.1118/1.2001767.

[7] J. A. Rawlinson, M. K. Islam, and D. M. Galbraith. Dose to radiation therapists from activation at high-energy accelerators used for conventional and intensity-modulated radiation therapy. *Medical Physics*, 29(4):598–608, 2002. 10.1118/1.1463063.

[8] ICRP. ICRP Publication 103: The 2007 recommendations of the International Commission on Radiological Protection. *Annals of the ICRP*, 37(2-4), 2007.

[9] G. Baiocco, et al. The origin of neutron biological effectiveness as a function of energy. *Scientific Reports*, 6:34033, 2016. 10.1038/srep34033.

[10] R. L. Bramblett, R. I. Ewing, and T. W. Bonner. A new type of neutron spectrometer. *Nuclear Instruments and Methods*, 9(1):1–12, 1960. 10.1016/0029-554X(60)90043-4.

[11] J. Dubeau, S. S. Hakmana Witharana, J. Atanackovic, A. Yonkeu, and J. P. Archambault. A neutron spectrometer using nested moderators. *Radiation Protection Dosimetry*, 150(2): 217–222, 2012. 10.1093/rpd/ncr381.

[12] R. M. Howell, N. E. Hertel, Z. Wang, J. Hutchinson, and G. D. Fullerton. Calculation of effective dose from measurements of secondary neutron spectra and scattered photon dose from dynamic MLC IMRT for 6 MV, 15 MV, and 18 MV beam energies. *Medical Physics*, 33(2):360–368, 2006. 10.1118/1.2140119.

[13] R. Maglieri, A. Licea, M. Evans, J. Seuntjens, and J. Kildea. Measuring neutron spectra in radiotherapy using the nested neutron spectrometer. *Medical Physics*, 42(11):6162–6169, 2015. 10.1118/1.4931963.

[14] A. P. Dempster, N. M. Laird, and D. B. Rubin. Maximum Likelihood from Incomplete Data via the EM Algorithm. *Journal of the Royal Statistical Society. Series B (Methodological)*, 39(1):1–38, 1977. 10.1111/j.2517-6161.1977.tb01600.x.

[15] L. A. Shepp and Y. Vardi. Maximum likelihood reconstruction for emission tomography. *IEEE Transactions on Medical Imaging*, MI-1(2):113–122, 1982. 10.1109/TMI.1982.4307558.

[16] L. Montgomery, M. Evans, L. Liheng, R. Maglieri, and J. Kildea. The effect of the flattening filter on photoneutron production at 10 MV in the Varian TrueBeam linear accelerator. *Medical Physics*, 45(10):4711–4719, 2018. 10.1002/mp.13148.

[17] B. Pehlivanovic, S. Avdic, P. Marinkovic, S. A. Pozzi, and M. Flaska. Comparison of unfolding approaches for monoenergetic and continuous fast-neutron energy spectra. *Radiation Measurements*, 49:109–114, 2013. 10.1016/j.radmeas.2012.12.008.

[18] D. L. Synder, M. I. Miller, L. J. Thomas, Jr, and D. G. Politte. Noise and Edge Artifactsin Maximum-Likelihood Reconstructions for Emission Tomography. *IEEE Transactions on Medical Imaging*, MI-6(3):228–238, 1987. 10.1109/TMI.1987.4307831.

[19] F. Ben Bouallègue, J. F. Crouzet, and D. Mariano-Goulart. A heuristic statistical stopping rule for iterative reconstruction in emission tomography. *Annals of Nuclear Medicine*, 27 (1):84–95, 2013. 10.1007/s12149-012-0657-5.

[20] E. Garduño and G. T. Herman. Superiorization of the ML-EM Algorithm. *IEEE Transactions on Nuclear Science*, 61(1):162–172, 2014. 10.1109/TNS.2013.2283529.

[21] T. Goorley, et al. Initial MCNP6 Release Overview. *Nuclear Technology*, 180:298–315, 2012. 10.13182/NT11-135.

[22] E. L. Crow. The mean deviation of the Poisson distribution. *Biometrika*, 45(3-4):556–562, 1958. 10.1093/biomet/45.3-4.556.

[23] ICRP. ICRP Publication 74: Conversion coefficients for use in radiological protection against external radiation. *Annals of the ICRP*, 26(3-4), 1996.

[24] L. Montgomery, G. Al Makdessi, R. Maglieri, F. Mathew, and J. Kildea. Neutron spectrometry. *GitHub repository*, 2020. 10.5281/zenodo.3610493.

Part II

Using Monte Carlo methods to model the energy dependence of neutron RBE for stochastic effects

Chapter 6

Radiation carcinogenesis

In Part II of this thesis the focus shifts from experimental measurements of neutron spectra to computational modeling of neutron RBE for inducing stochastic radiobiological effects like carcinogenesis. To this end, this chapter presents a fundamental overview of both (a) the characteristic features of carcinogenesis and (b) the mechanisms by which radiation can induce carcinogenesis.

6.1 The genome

Discussion of carcinogenesis requires an understanding of the deoxyribonucleic acid (DNA) molecule, genes, and genetic mutations. A high-level summary of these topics is presented in this section.

6.1.1 The structure of human DNA

At the molecular level, DNA is comprised of paired strands of nucleotides arranged in a double helix [1]. A nucleotide is a molecule consisting of three components: a nitrogenous base, a five-carbon sugar (deoxyribose in the case of DNA), and a phosphate. There are four types of nitrogenous bases that are used to construct DNA and they are classified according to their molecular structure as either a purine or a pyrimidine. The purines are adenine (A) and guanine (G), while the pyrimidines are thymine (T) and cytosine (C). A single strand of DNA is formed by linking the 3' (3-prime) and 5' (5-prime) carbon atoms of adjacent deoxyribose molecules via phosphodiester bonds. A second strand of DNA is bound to the first via several weak,

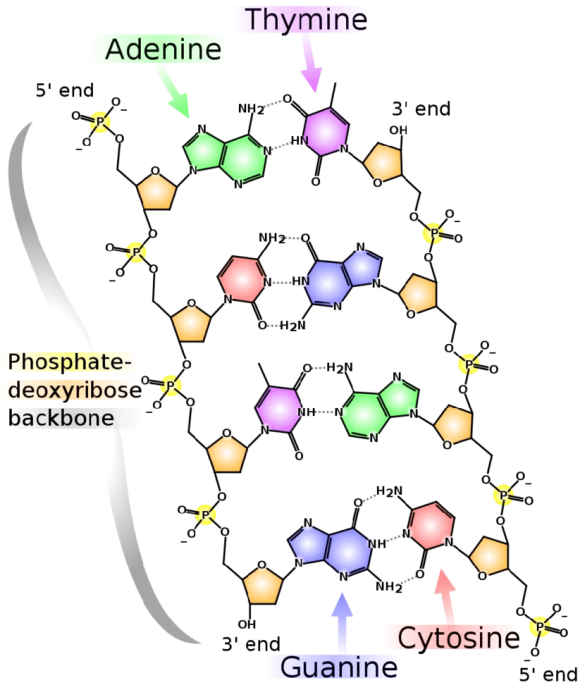

Figure 6.1 The molecular structure of the DNA double helix. Figure reproduced from Price Ball [2].

non-covalent interactions, including hydrogen bonds between opposing bases on either strand. The result is the iconic DNA double helix containing two strands of DNA that are said to be both complementary and antiparallel to each other. Complementarity refers to the fact that the nitrogenous bases on the strands always bind in pairs, such that adenine always binds with thymine and guanine always binds with cytosine. The strands are considered antiparallel because they are bound in opposite orientation (i.e. the 3' end of one DNA strand is bound to the 5' end of the complementary strand). A schematic of the structure of paired DNA strands is shown in Figure 6.1.

An overview of the organizational structure of DNA from the double helix to the chromatid is presented in Figure 6.2 [3]. To summarize, a segment of DNA containing approximately 150 nucleotide base pairs (bp) is tightly wrapped around a core of eight histone proteins to form a nucleosome [4]. Nucleosomes are joined via linker DNA, resulting in the "beads on a string structure of DNA" known as euchromatin. Further compaction is achieved via the helical arrangement of linked nucleosomes into a "30-nanometer fibre", as shown in Figure 6.2. As suggested by the name, these chromatin fibres have a diameter of $\sim$30 nm and

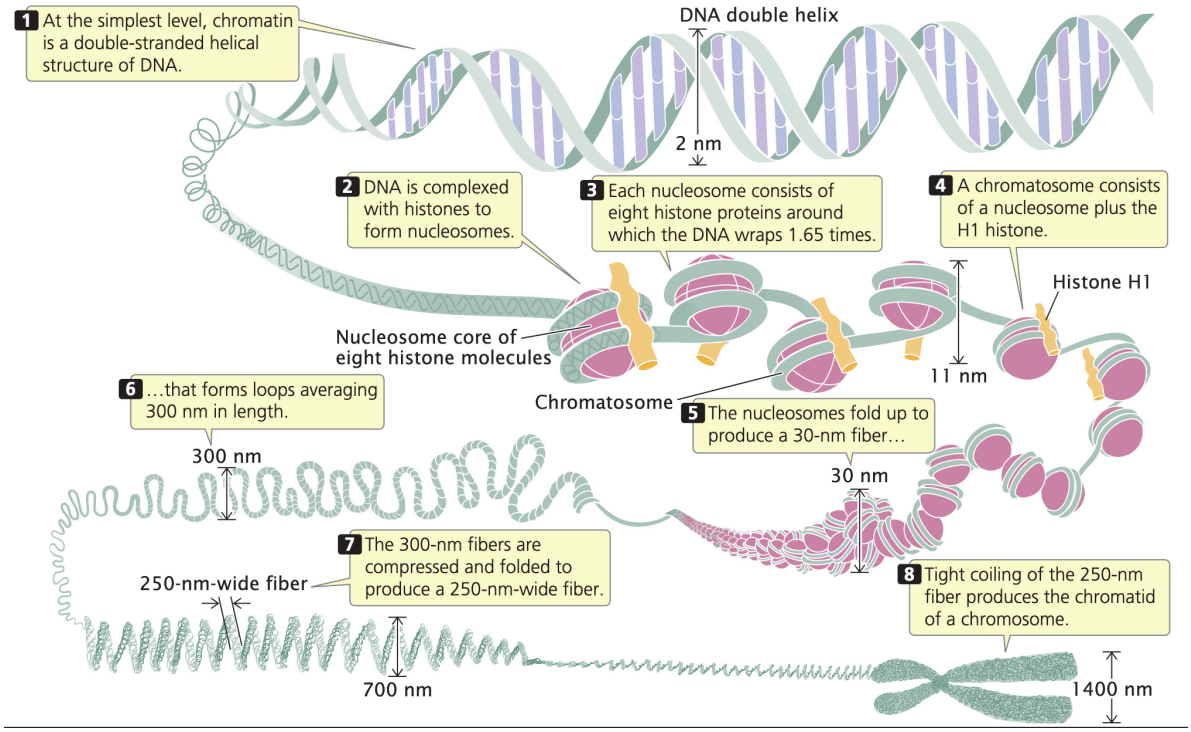

Figure 6.2 The hierarchical arrangement of DNA from the double helix to the chromatid. Figure reproduced from Pierce [3].

are known as heterochromatin. Discrete, tightly-coiled segments of heterochromatin are known as chromosomes. Prior to mitosis (somatic cell division), chromosomes are replicated to form paired sister chromatids that are attached via a centrometre as shown at the end of Figure 6.2.

The Human Genome Project (HGP) elucidated that there are $\sim 3.1 \times 10^9$ bp comprising the human genome [5], which are contained within 24 chromosomes (22 autosomal chromosomes as well as the sex-determining X and Y chromosomes). Most human cells are diploid, which means they contain a maternal and paternal copy of each autosomal chromosome and two sex-determining chromosomes. Thus, there are approximately 6.2×10^9 bp in human somatic cells during interphase, i.e. the phase of the cell cycle when it is not dividing [4].

6.1.2 Genes

A gene is a unit of genetic information that is comprised of a specific sequence of DNA base pairs [6] and codes for the production of specific proteins with various biological functions. Genes can take different forms called alleles that, along with other environmental factors,

determine how a gene is expressed (i.e. its phenotype). The full genome contains approximately 21,000 protein-coding genes and a comparable number of non-coding segments of DNA (the exact numbers are a matter of scientific debate) [7].

6.1.3 Genetic mutations

A genetic mutation is a permanent change in a sequence of DNA that can be passed from a cell to its offspring via mitosis (somatic mutations) or from a parent organism to its offspring via reproduction (germ-line mutations) [3]. The most fundamental way to classify mutations is on the basis of their molecular nature, for which there are three categories: base substitutions, insertions, and deletions. A base substitution is an alteration in a single nucleotide base, for example the replacement of an A with a C. Deletions and insertions constitute the removal or addition of one or more base pairs in a sequence of DNA, respectively. Examples of these types of mutations are shown schematically in Figure 6.3.

There are a variety of possible phenotypic effects that result from a genetic mutation [3]. If protein production and function is unimpacted by the mutation then the mutation is classified as silent or neutral. If the mutation impacts protein function, it can be classified as either a loss-of-function mutation or a gain-of-function mutation. A loss-of-function mutation causes complete or partial disruption in protein function whereas a gain-of-function mutation causes irregular function with regards to the time or location of gene expression.

Mutations play a crucial role in genetic variation between organisms in a population as well as the evolution of species over time. However, mutations can also have serious adverse biological consequences to an organism.

6.2 Carcinogenesis

The longest standing model of carcinogenesis is the somatic mutation theory, which essentially stipulates that somatic mutations in certain genes can lead to the development of cancer [8, 9]. Mutations in three classes of genes constitute the basis of this theory: proto-oncogenes, tumour suppressor genes, and DNA stability genes [6].

Proto-oncogenes promote cell growth. A gain-of-function mutation in a proto-oncogene can cause a cell to ignore signals from other cells and thereby promote unregulated growth and division. In contrast to proto-oncogenes, tumour suppressor genes act as negative growth

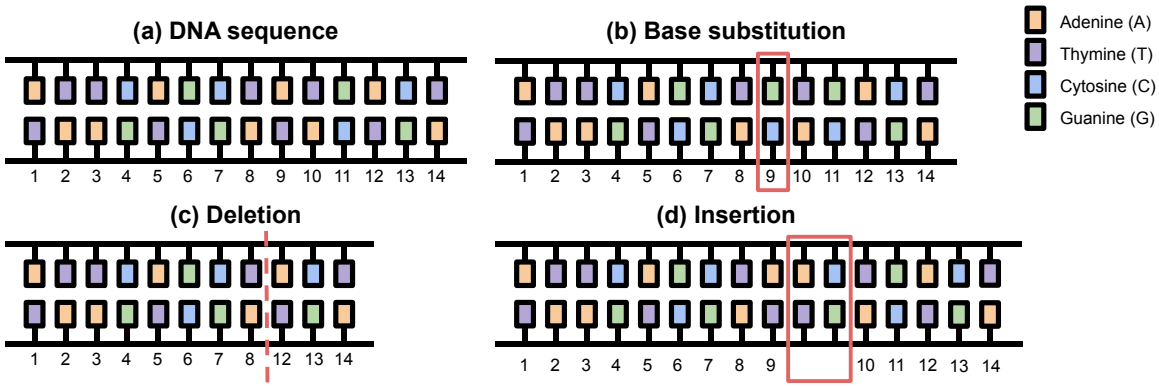

Figure 6.3 Schematic examples of the types of DNA mutations according to their molecular structure: (a) a non-mutated sequence of DNA, (b) a base substitution, (c) a deletion, and (d) an insertion.

regulators. Thus, a loss-of-function mutation in a tumour suppressor can also result in uncontrolled cell growth. Finally, DNA stability genes play a key role in ensuring the integrity of DNA. Improper function of DNA stability genes can result in the cell's inability to detect and repair DNA damage and can lead to the onset of mutagenesis.

Although a complete formula for the onset of carcinogenesis has yet to be established, it is generally believed that the accumulation of multiple mutations is a stimulant for carcinogenic effects [6]. Mutations that arise naturally within the cell tend to accumulate over time, which helps to explain the increase in cancer risk with increasing age [10]. However, there are other risk factors for carcinogenesis in addition to aging. Carcinogens are external agents that can induce genetic mutations, accelerate their accumulation, and ultimately are associated with increased cancer risk. Ionizing radiation is a recognized carcinogen that is capable of inducing genetic mutations and promoting carcinogenic effects.

6.3 Evidence of radiation carcinogenesis

Much of our understanding about the carcinogenic effects of ionizing radiation in humans is derived from epidemiologic studies in populations that were exposed to high levels of radiation [11]. The most recent report of the United Nations Scientific Committee on the Biological Effects of Ionizing Radiation (BEIR), BEIR VII [12], provides quantitative estimates of the carcinogenic risk associated with ionizing radiation. The authors of the BEIR VII report

estimated that the population-averaged excess cancer risk is 10.8% per Sv [6]. However, the authors demonstrated that excess cancer risk estimates vary significantly with many factors including sex and age at the time of exposure. The results summarized in the BEIR VII report are primarily based on data from the Life Span Study (LSS) [13], which is an ongoing analysis of radiation-induced effects on the survivors of the atomic bombings of Hiroshima and Nagasaki.

The carcinogenic risk associated with low doses of radiation ($\lesssim$ 100 mSv) is a matter of ongoing scientific debate [14–16]. The most widespread theory of carcinogenic risk applied in radiation protection is the linear-non-threshold (LNT) model. The LNT model stipulates: (i) that there is no minimum threshold dose below which the stochastic biological effects of ionizing radiation do not occur and (ii) that the risk is is linearly proportional to the amount of dose received. In terms of mutagenesis, the LNT model implies that a single ionizing radiation event has a nonzero risk of inducing a mutation and that the risk increases linearly with increasing radiation exposure.

Radiation therapy patients are one of few populations exposed to low doses of whole-body radiation that can be epidemiologically studied for increased cancer risk. Hall and Giaccia [6] performed a review of such epidemiologic studies in 2012. They found that all single-institution studies independently concluded that there was no increased risk of second malignancies among patients that received radiation therapy compared to other standards of care. However, some multi-institutional studies with larger patient cohorts, and thus greater statistical power, have identified statistically significant excess cancer rates among radiation therapy patients, which were elevated in long-term survivors. Among these larger studies, Brenner et al. [17] found an average increased second cancer risk of 6% among a population of 51,000 cancer patients treated for primary prostate cancer using solely radiation therapy compared to a population of 70,000 patients who were treated using surgery alone. The excess second cancer risk was found to increase with post-treatment time and reached 34% after 10 years. More recently, Grantzau and Overgaard [18] reviewed second cancer occurrence among 762,458 breast cancer patients. They identified an excess cancer risk in patients treated with radiation therapy that was on the order of a few percent and also increased with time post-treatment. While not definitive, such epidemiologic studies indicate that the low doses of whole-body radiation received by patients during radiation therapy are associated with an increased cancer risk.

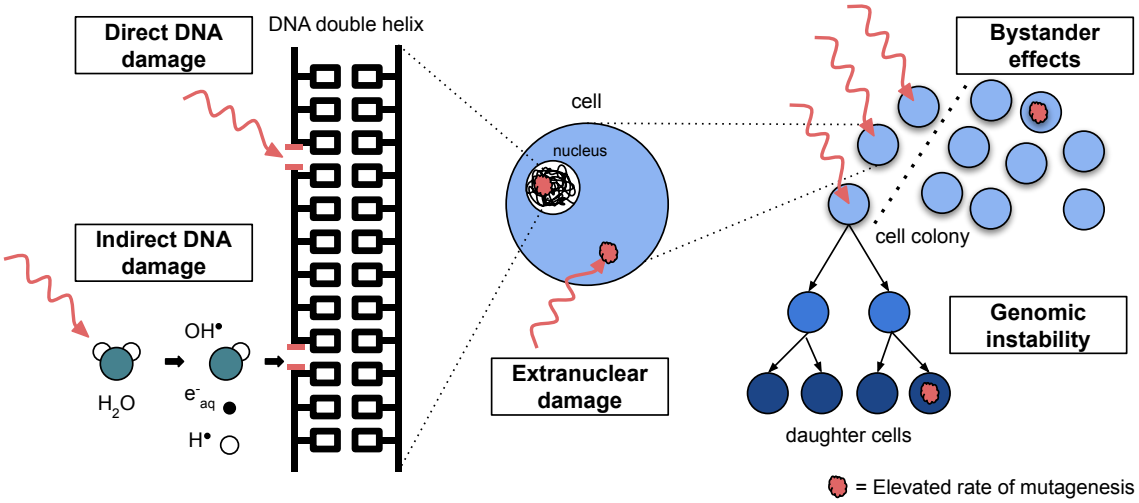

Figure 6.4 Pathways for radiation-induced mutagenesis with potential carcinogenic effects.

6.4 Pathways for radiation carcinogenesis

Presently, there are believed to be several pathways by which ionizing radiation can induce mutagenesis, which may subsequently lead to carcinogenesis. These pathways are described below and are shown schematically in Figure 6.4.

Target theory is a concept that has been applied to radiation-induced biological damage for many decades [6, 11, 19–23]. This theory proposes that radiation interactions in specific biological targets can cause adverse biological effects including mutagenesis. The most widely-studied target is nuclear DNA, which can be damaged by radiation via direct and indirect action [6]. Direct action is the ability of radiation to directly interact with atoms of DNA, which can cause excitations and ionizations that result in DNA damage. Indirect action refers to the ability of radiation to ionize and excite water molecules near DNA in a process known as water radiolysis. Water radiolysis generates a variety of highly-reactive products called free radicals (e.g. $OH^\bullet$ radicals, aqueous electrons e^-_{aq}, etc.) that may diffuse far enough to interact with DNA molecules and cause damage [24]. A permanent genetic mutation can occur if the DNA damage induced by direct or indirect action is not repaired or is misrepaired.

Experimental evidence has indicated that nuclear DNA is not the only biological target of radiation action that can lead to mutagenesis. For example, a pioneering study by Wu et al. [25] used microbeams of alpha particles to selectively irradiate the cytoplasm of individual cells

without irradiating the nucleus, which resulted in a unique spectrum of mutations in nuclear DNA.

Other avenues for radiation-mutagenesis have been proposed as a result of experimental evidence of enhanced levels of mutations in cells that were not directly exposed to ionizing radiation [11, 20, 22]. These non-DNA targeted effects (NTEs) are broadly classified as (i) radiation-induced bystander effects (RIBEs) and (ii) radiation-induced genomic instability (RIGI) [22]. RIBEs are characterised by elevated rates of deleterious cellular effects (e.g. mutations, cell death, etc.) in cells that are in the same colony as irradiated cells but that were not directly exposed [21, 22]. RIGI refers to elevated rates of genetic alterations (e.g. mutations, chromosome aberrations, etc.) within cells that descend from those that were irradiated but did not experience genetic modifications themselves [22]. There is evidence to suggest that NTEs have epigenetic origins, i.e. due to alterations in gene expression rather than genetic mutations of the DNA sequence [22]. However, the exact nature of the cellular mechanisms that give rise to these NTEs has not been determined conclusively.

The roles of extranuclear irradiation and NTEs in causing carcinogenesis are consistent with the somatic mutation theory and do not refute the notion of target theory. Rather, they promote the concept of an "expanding target" [22] both spatially (via extranuclear irradiation and RIBEs) and temporally (via RIGI). Nevertheless, the mechanisms for these carcinogenic pathways are considerably more unclear than the mechanisms of radiation-induced nuclear DNA damage. The remainder of this thesis will focus on the mutagenic affects associated with nuclear DNA damage with the understanding that they constitute only one piece of the larger puzzle of radiation carcinogenesis.

6.5 Radiation-induced DNA damage

As previously discussed, direct and indirect action of radiation on DNA can induce DNA damage that, if misrepaired or left unrepaired, can result in mutagenesis. An approximate timescale for the physical, chemical, and biological effects of radiation action on DNA is shown in Figure 6.5. DNA damage also occurs routinely in cells due to the production of free radicals by endogenous processes like oxidative metabolism [26]. Indeed, cells have sophisticated and effective DNA repair mechanisms, collectively known as the DNA damage response, to fix DNA damage lesions [6].

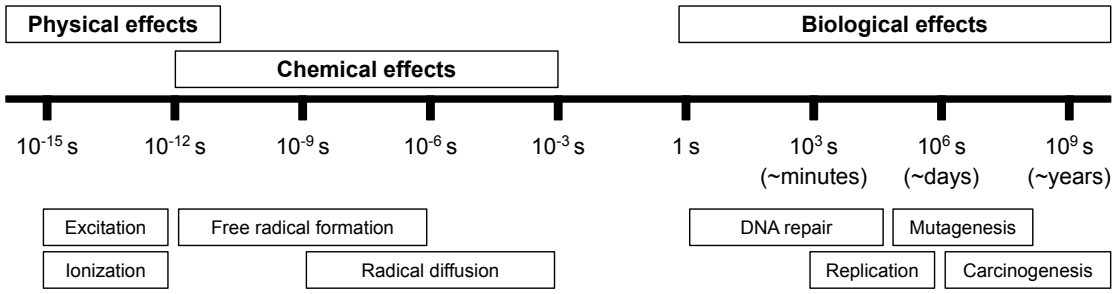

Figure 6.5 Approximate timescale for the effects of radiation action on nuclear DNA. Figure adapted from Ledingham et al. [27].

This section describes the main types of DNA damage that can occur as well as the DNA repair mechanisms typically employed to fix them. The chapter concludes with a discussion of the propensity of radiation to induce clusters of DNA damage, which impede the typical DNA repair pathways and are thus prone to misrepair and mutagenesis. All types of DNA damage considered in this section are shown schematically in Figure 6.6.

6.5.1 Single strand breaks and base damage

There are two fundamental types of DNA damage: DNA single strand breaks (SSBs) and base damage. A strand break is simply the result of a break in the phosphodiester bond between adjacent sugar molecules in a strand of DNA. Base damage is a broader term that encapsulates several types of damage to the nitrogenous bases of DNA, including the following subcategories:

- Apurinic and Apyrimidinic sites (collectively called AP sites) where the nitrogenous base has been removed from a nucleotide in a DNA strand.
- Oxidized bases, wherein a nitrogenous base has been oxidized (i.e. an atomic electron has been removed).

Base excision repair (BER) is the most relevant repair mechanism for both isolated base damage and SSBs [28]. The BER pathway is triggered when an oxidized or otherwise damaged base is detected by a DNA glycosylase enzyme, which then mediates the removal of the base to yield a temporary AP site [29]. The AP site is cleaved from the DNA strand by another enzyme (an AP endonuclease), resulting in a temporary single strand break. In the final stages of BER,

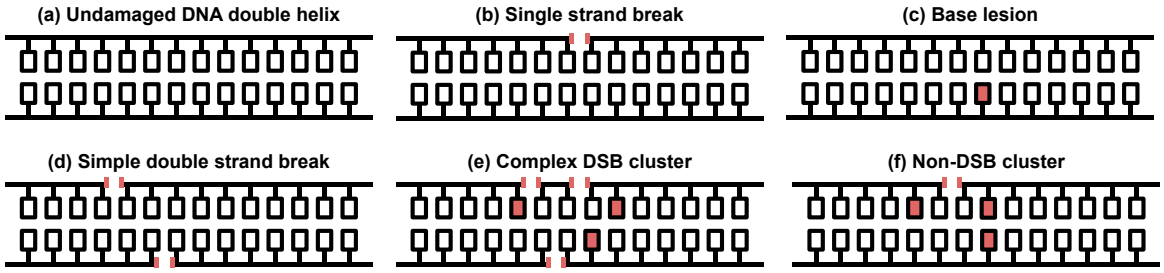

Figure 6.6 Schematic examples of several types of DNA damage that can occur. (a) An undamaged DNA double helix wherein each square represents a nitrogenous base attached to the sugar-phosphate backbone. (b) A single strand break (SSB) depicted as a red separation in the backbone. (c) A generic base lesion depicted as a red base. (d) A double strand break (DSB) containing two SSBs on opposing strands. (e) A complex DSB cluster containing two or more damage sites, including at least one DSB. (f) A non-DSB cluster containing two or more SSBs or base lesions.

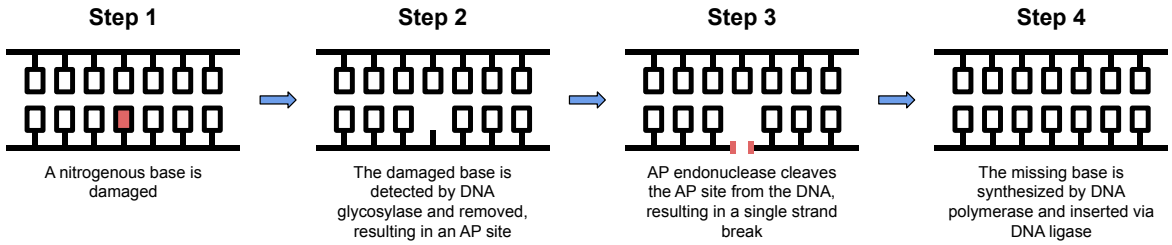

Figure 6.7 The base excision repair repair pathway used to repair DNA base damage. AP sites and single strand breaks are repaired via the same pathway starting from steps 2 and 3, respectively.

polymerase enzymes synthesize a replacement nucleotide or chain of nucleotides that is inserted into the gap and attached via ligase proteins. The repair of AP sites and SSBs follow from the appropriate steps of the BER pathway [29]. This process is shown schematically in Figure 6.7.

6.5.2 DNA double strand breaks

A DNA double strand break (DSB) occurs when two SSBs are induced within one or two turns of the DNA double helix (i.e. within 10–20 bp) on opposing strands [29, 30]. When a DSB occurs, the remaining non-covalent bonds between paired nucleotides and the influence of higher order chromatin structure are not strong enough to keep the two DNA fragments bound together [29].

DSBs are typically repaired by one of two mechanisms that are known as homologous recombination repair (HRR) and non-homologous end-joining (NHEJ) [6]. HRR is slower process than NHEJ [29] and is only available to cells in the late S or G2 phase of the cell cycle wherein a sister chromatid is used as a template to ensure accurate repair. Cells that lack a sister chromatid (i.e. not in the late S or G2 phase) are repaired via the NHEJ pathway, which is more error-prone than HRR. For example, a mutation will arise if the DNA fragments resulting from a DSB are joined together at the wrong ends during NHEJ. If this genetic rearrangement is stable, in that it does not cause cell death, it can potentially activate an oncogene or de-activate a tumour suppressor gene [29].

6.5.3 Clustered DNA damage

Radiation-induced isolated DNA damage lesions and DSBs can lead to misrepair and mutagenesis. However, these lesions are not believed to be the primary cause for the increased mutagenic risk associated with ionizing radiation at low doses because (i) they are not produced at large quantities at low doses relative to the endogenous rates of their production and (ii) their repair mechanisms are generally quite effective [19, 31]. Instead, the propensity of radiation to induce clusters of DNA lesions in close spatial proximity is widely considered a key initiating event for mutagenesis [28–30]. These clustered DNA damage lesions (also known as locally multiply damaged sites; LMDS [6, 31]) are rarely produced endogenously.

Both the mechanisms involved in DNA repair and their efficacy are impacted when individual damages are clustered together within a few turns of the DNA double helix [28, 29]. The extent to which repair is impeded depends on the types of constituent damage and their proximity to each other, in terms of both the number of base pairs between lesions and whether the lesions are located within the same strand or on opposing strands [32, 33]. Detailed reviews of this subject were recently conducted by Nickoloff et al. [34] and Sage and Shikazono [28].

Clustered lesions can be broadly classified as either (i) non-DSB clusters or (ii) complex DSB clusters [28–30, 34]. Non-DSB clusters are comprised of SSBs, AP sites, and/or oxidized bases and constitute approximately 70–80% of clustered DNA damage induced by low LET radiation [28, 29]. The remaining 20–30% of clustered lesions are complex DSB clusters that differ from “simple” DSBs due to the presence of one or more other lesions surrounding the DSB.

Non-DSB clusters can lead to mutagenesis in many possible ways. One avenue is through misrepair of a non-DSB cluster that results in a *de novo* complex DSB cluster [29]. For example, simultaneous BER of adjacent base lesions in a non-DSB cluster can inadvertently cause a DSB, which is more difficult to repair than a simple DSB because of the additional surrounding damage. However, it is important to acknowledge that the production of *de novo* DSBs is not the only way by which non-DSB clusters can lead to mutations [30]. For example, the mere presence of a AP site or SSB adjacent to an oxidized base greatly slows the BER pathway and can yield mutations if the repair process is incomplete or in progress during DNA replication [30].

Complex DSB clusters are typically repaired by the same HRR and NHEJ pathways as simple DSBs but the efficacy is much lower due to the presence of additional DNA lesions. This slow and inaccurate repair of complex DSB clusters primarily results in deletion mutations that may span up to a few hundred base pairs [28, 30]. Misrepair of non-DSB clusters leads to a more diverse spectrum of mutations including base substitutions, insertions, and deletions.

6.6 Summary

This chapter presented an overview of the structure and function of human DNA as well as its role in carcinogenesis. The pathways by which radiation can induce mutagenesis and subsequent carcinogenesis were then discussed. The propensity of radiation to induce clusters of DNA damage that are prone to misrepair and mutagenesis makes for a compelling avenue to model radiation-induced stochastic effects. The following chapters describe how Monte Carlo methods can be used to model radiation-induced DNA damage in general, and to model clustered DNA damage specifically to assess neutron RBE for stochastic effects.

References

[1] L. A. Pray. Discovery of DNA Structure and Function: Watson and Crick, 2008. https://www.nature.com/scitable/topicpage/discovery-of-dna-structure-and-function-watson-397/.

[2] M. Price Ball. Chemical structure of DNA, 2018. https://commons.wikimedia.org/wiki/File:DNA_chemical_structure.svg#/media/File:DNA_chemical_structure.svg.

[3] B. A. Pierce. *Genetics A Conceptual Approach*. W. H. Freeman Company, New York, fourth edition, 2012.

[4] A. Annunziato. DNA Packaging: Nucleosomes and Chromatin, 2008. https://www.nature.com/scitable/topicpage/dna-packaging-nucleosomes-and-chromatin-310.

[5] P. F. Little. Structure and function of the human genome. *Genome Research*, 15(12): 1759–1765, 2005. 10.1101/gr.4560905.

[6] E. J. Hall and A. J. Giaccia. *Radiobiology for the radiologist: Seventh edition*. Lippincott Williams & Wilkins, Philadelphia, seventh edition, 2012.

[7] C. Willyard. New human gene tally reignites debate. *Nature*, 558(7710):354–355, 2018. 10.1038/d41586-018-05462-w.

[8] D. Hanahan and R. A. Weinberg. The Hallmarks of Cancer. *Cell*, 100:57–70, 2000. 10.1016/S0092-8674(00)81683-9.

[9] D. Hanahan and R. A. Weinberg. Hallmarks of cancer: The next generation. *Cell*, 144(5): 646–674, 2011. 10.1016/j.cell.2011.02.013.

[10] S. R. Kennedy, L. A. Loeb, and A. J. Herr. Somatic mutations in aging, cancer and neurodegeneration. *Mechanisms of Ageing and Development*, 133(4):118–126, 2012. 10.1016/j.mad.2011.10.009.

[11] J. B. Little. Radiation carcinogenesis. *Carcinogenesis*, 21(3):397–404, 2000. 10.1093/carcin/21.3.397.

[12] National Research Council of the National Academies. *Health risks from exposures to low levels of ionizing radiation: BEIR VII Phase 2*. The National Academics Press, Washington DC, 2006.

[13] E. J. Grant, et al. Solid Cancer Incidence among the Life Span Study of Atomic Bomb Survivors: 1958–2009. *Radiation Research*, 187(5):513–537, 2017. 10.1667/rr14492.1.

[14] W. F. Morgan and W. J. Bair. Issues in Low Dose Radiation Biology: The Controversy Continues. A Perspective. *Radiation Research*, 179(5):501–510, 2013. 10.1667/rr3306.1.

[15] L. Mullenders, M. Atkinson, H. Paretzke, L. Sabatier, and S. Bouffler. Assessing cancer risks of low-dose radiation. *Nature Reviews Cancer*, 9(8):596–604, 2009. 10.1038/nrc2677.

[16] R. W. Harbron. Cancer risks from low dose exposure to ionising radiation - Is the linear no-threshold model still relevant? *Radiography*, 18(1):28–33, 2012. 10.1016/j.radi.2011.07.003.

[17] D. J. Brenner, R. E. Curtis, E. J. Hall, and E. Ron. Second malignancies in prostate carcinoma patients after radiotherapy compared with surgery. *Cancer*, 88(2):398–406, 2000. 10.1002/(SICI)1097-0142(20000115)88:2<398::AID-CNCR22>3.0.CO;2-V.

[18] T. Grantzau and J. Overgaard. Risk of second non-breast cancer after radiotherapy for breast cancer: A systematic review and meta-analysis of 762,468 patients. *Radiotherapy and Oncology*, 114(1):56–65, 2015. 10.1016/j.radonc.2014.10.004.

[19] D. T. Goodhead. Initial events in the cellular effects of ionizing radiations: Clustered damage in DNA. *International Journal of Radiation Biology*, 65(1):7–17, 1994. 10.1080/09553009414550021.

[20] R. Iyer and B. E. Lehnert. Effects of ionizing radiation in targeted and nontargeted cells. *Archives of Biochemistry and Biophysics*, 376(1):14–25, 2000. 10.1006/abbi.1999.1684.

[21] K. T. Butterworth, S. J. McMahon, A. R. Hounsell, J. M. O'Sullivan, and K. M. Prise. Bystander signalling: Exploring clinical relevance through new approaches and new models. *Clinical Oncology*, 25(10):586–592, 2013. 10.1016/j.clon.2013.06.005.

[22] M. Kadhim, et al. Non-targeted effects of ionising radiation-Implications for low dose risk. *Mutation Research - Reviews in Mutation Research*, 752(2):84–98, 2013. 10.1016/j.mrrev.2012.12.001.

[23] A. L. McNamara, et al. Geometrical structures for radiation biology research as implemented in the TOPAS-nBio toolkit. *Physics in Medicine and Biology*, 63(17):175018, 9 2018. 10.1088/1361-6560/aad8eb.

[24] E. B. Podgoršak. *Radiation Physics for Medical Physicists*. Springer International Publishing Switzerland, Swizterland, third edition, 2016.

[25] L. J. Wu, et al. Targeted cytoplasmic irradiation with alpha particles induces mutations in mammalian cells. *Proceedings of the National Academy of Sciences of the United States of America*, 96(9):4959–4964, 1999. 10.1073/pnas.96.9.4959.

[26] R. De Bont and N. van Larebeke. Endogenous DNA damage in humans: A review of quantitative data. *Mutagenesis*, 19(3):169–185, 2004. 10.1093/mutage/geh025.

[27] K. W. Ledingham, P. R. Bolton, N. Shikazono, and C. M. Ma. Towards laser driven hadron cancer radiotherapy: A review of progress. *Applied Sciences (Switzerland)*, 4(3):402–443, 2014. 10.3390/app4030402.

[28] E. Sage and N. Shikazono. Radiation-induced clustered DNA lesions: Repair and mutagenesis. *Free Radical Biology and Medicine*, 107:125–135, 2017. 10.1016/j.freeradbiomed.2016.12.008.

[29] K. Magnander and K. Elmroth. Biological consequences of formation and repair of complex DNA damage. *Cancer Letters*, 327(1-2):90–96, 2012. 10.1016/j.canlet.2012.02.013.

[30] A. G. Georgakilas, P. O'Neill, and R. D. Stewart. Induction and Repair of Clustered DNA Lesions: What Do We Know So Far? *Radiation Research*, 180(1):100–109, 2013. 10.1667/rr3041.1.

[31] J. F. Ward. Radiation Mutagenesis : The Initial DNA Lesions Responsible. *Radiation Research*, 142(3):362–368, 1995. 10.2307/3579145.

[32] M. E. Lomax, L. K. Folkes, and P. O'Neill. Biological consequences of radiation-induced DNA damage: Relevance to radiotherapy. *Clinical Oncology*, 25(10):578–585, 2013. 10.1016/j.clon.2013.06.007.

[33] L. J. Eccles, P. O'Neill, and M. E. Lomax. Delayed repair of radiation induced clustered DNA damage: Friend or foe? *Mutation Research - Fundamental and Molecular Mechanisms of Mutagenesis*, 711(1-2):134–141, 2011. 10.1016/j.mrfmmm.2010.11.003.

[34] J. A. Nickoloff, N. Sharma, and L. Taylor. Clustered DNA double-strand breaks: Biological effects and relevance to cancer radiotherapy. *Genes*, 11(1), 2020. 10.3390/genes11010099.

Chapter 7

Monte Carlo simulations of radiation transport

Radiation transport codes based on the Monte Carlo (MC) method can be used to simulate radiation interactions with biological targets such as DNA. This chapter begins with an overview of the MC method and how it can be used to model radiation transport. Subsequently, overviews of both condensed-history Monte Carlo (CHMC) methods and track-structure Monte Carlo (TSMC) methods are provided. These discussions focus on the Geant4 and TOPAS CHMC codes as well as their TSMC extensions, Geant4-DNA and TOPAS-nBio. The chapter concludes with a review of MC investigations into the energy dependence of neutron RBE.

7.1 The Monte Carlo method

The MC method refers to a class of numerical techniques that use stochastic sampling to model the outcomes of probabilistic events. These techniques were developed by scientists working on thermonuclear weapons in Los Alamos during the 1940s [1]. A high-level description of the MC method was first provided by Metropolis and Ulam [2] who also coined the term Monte Carlo in reference to a casino in Monaco.

In the modern era, the MC method is implemented computationally using algorithms called random number generators (RNGs). Because computers are inherently deterministic and thus cannot generate truly random numbers, an RNG generates "pseudorandom" numbers [3]. A well-designed RNG is able to produce sequences of pseudorandom numbers that appear

uncorrelated to any statistical test. In the context of MC, a pseudorandom number ξ, generated by an RNG, is used to generate a random quantity of interest x via its underlying probability distribution function (PDF) $f(x)$. Further details of this method are presented in the next section.

7.2 Radiation transport with Monte Carlo

The challenge of modeling radiation transport in matter is well suited for application of the MC method because radiation interactions are governed by probability distributions. As an illustrative example, consider the below problem of determining the distance between subsequent interactions by a photon traversing an arbitrary absorbing medium.

7.2.1 Example Monte Carlo exercise: Determining the distance between photon interactions

The probability distribution function governing the distance x between photon interactions in an absorbing material is described by the following exponential distribution [1]:

$$f(x) = \mu e^{-\mu x} \tag{7.1}$$

where μ is the energy-dependent linear attenuation coefficient for the material being traversed, with units of inverse distance. This total linear attenuation coefficient is related to the cross sections for the photon interactions that were described in Chapter 2 via the following equation [4]:

$$\mu = N(\sigma_{\mathrm{RS}} + \sigma_{\mathrm{PE}} + \sigma_{\mathrm{CS}} + \sigma_{\mathrm{PP}} + \sigma_{\mathrm{TP}} + \sigma_{\mathrm{PN}}) \tag{7.2}$$

where N is the density of atoms in the material and the subscripts on the cross sections σ correspond to the various photon interactions (i.e. RS = Rayleigh scattering, PE = photoelectric effect, CS = Compton scattering, PP = pair production, TP = triplet production, and PN = photonuclear reactions).

A pseudorandom estimate of x is obtained by way of the cumulative probability distribution function (CPD), which in this case is described as follows [1]:

$$F(x) = \int_{x_{\min}}^{x} f(x')\,\mathrm{d}x' = \int_{0}^{x} \mu e^{-\mu x'}\,\mathrm{d}x' = 1 - e^{-\mu x} \tag{7.3}$$

For a normalized PDF, the corresponding CPD is a monotonically increasing function of x with a minimum value of 0 and a maximum value of 1. Thus, a random estimate of x can be obtained via a pseudorandom number ξ that has a value between 0 and 1 by simply inverting the CPD. For sampling the distance between photon interactions this inversion results in the following relationship between x and ξ:

$$x = -\frac{1}{\mu}\ln(1-\xi) \tag{7.4}$$

7.2.2 Overview of simulating radiation transport

MC modeling of radiation transport involves the simulation of one or more initial (primary) particles in a geometric region of interest. A primary particle track and all of the secondary particle tracks it produces via physical interactions are collectively referred to as an event. Every particle track is treated as a set of discrete steps where each step encapsulates a single interaction and a distance travelled. Multiple pseudorandom numbers are required per step in order to describe:

1. The distance travelled by the particle between subsequent interactions (i.e. the step size).
2. The type of interaction.
3. The energy deposited by the interaction.
4. The energy distribution among the interaction products.
5. The angular orientation (i.e. direction) of the interaction products.

Each of these parameters has an associated PDF, as was shown above for the step size of a photon track.

All secondary particles that are generated while simulating the current particle track are added to a running queue that records the particle type, position, energy, and direction. Simulation of the current particle track is terminated when an end condition is satisfied. End conditions are typically one of the following: (i) the particle leaves the geometric region of interest, (ii) the particle is absorbed by an interaction such as the photoelectric effect, or (iii) the particle energy falls below a minimum energy threshold, at which point it is considered to have been absorbed locally by the medium. A flow diagram that demonstrates the simulation of a photon track is shown in Figure 7.1.

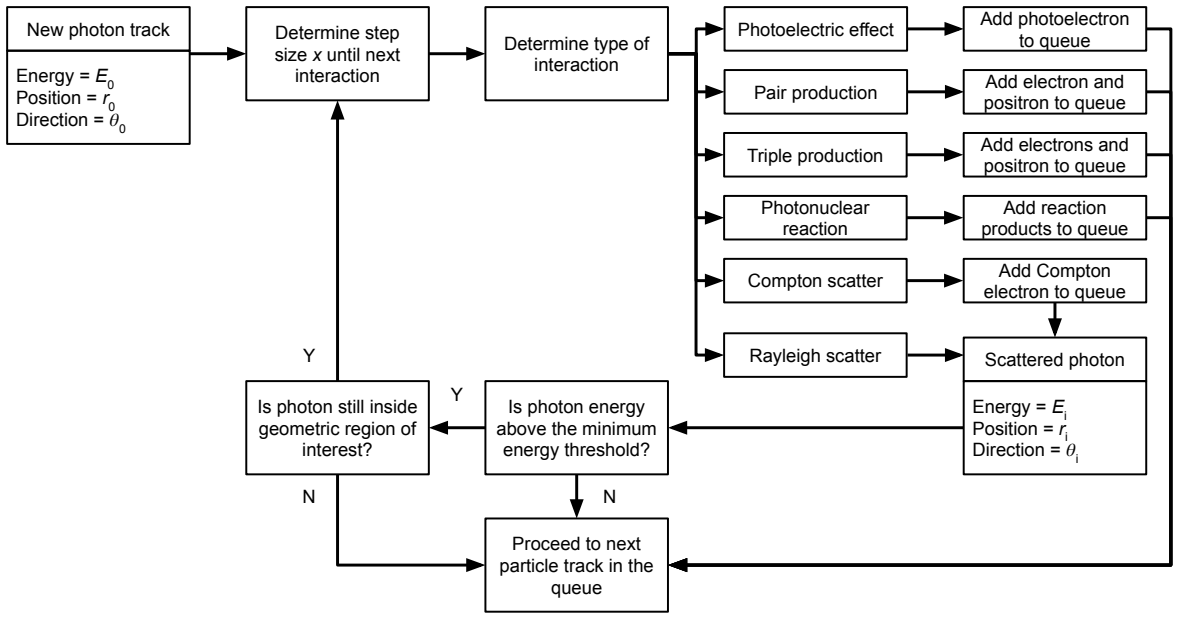

Figure 7.1 Flow diagram that demonstrates the simulation of a photon track in an absorbing medium using the MC method. Figure adapted from Andreo et al. [1].

This simulation process is repeated for every particle in the queue until the queue is empty. Typically one or more quantities of interest are recorded (i.e. scored) throughout the duration of the simulation, such as the total energy deposited in a particular geometric volume.

Although MC simulations are the gold standard for modeling radiation transport, they have historically been quite slow compared to other analytical methods [1]. The magnitude of this issue has been drastically reduced in recent years with modern computer architecture. Nevertheless, faster simulation speeds may be required in some circumstances, such as when modeling infrequent events, when attempting to quantify a low-magnitude effect, or in time-sensitive situations like the generation of radiation therapy treatment plan. One "brute force" approach to improving simulation speed is to parallelize the processing of particle tracks in the queue by using multiple CPUs or by running multiple simulations across multiple processing threads on the same CPU (i.e. multithreading).

Another optimization approach is to incorporate one or more variance reduction techniques (VRTs) in the simulation. VRTs are a class of statistical methods that use approximations to improve simulation efficiency with the requirements that they do not reduce simulation accuracy or introduce bias [1]. VRTs must be carefully designed to meet these requirements and typically the approximations underlying a particular VRT are only valid in a particular set of

circumstances. The most important VRT for the context of this thesis is the "condensed-history" transport of charged particles, which is the subject of the next section.

7.2.3 Condensed-history Monte Carlo

The simulation process outlined in the previous section is computationally undemanding for the transport of neutral particles like photons and neutrons because the average step size between interactions is approximately the same order of magnitude as the simulation geometry [3]. This is not true, however, for charged particles where the step size is often many orders of magnitude smaller than the size of the geometry. As described in Chapter 2, charged particle transport is dominated by many soft Coulomb collisions that increase MC computation time considerably. Thus, the explicit simulation of all charged particle interactions is a major bottleneck in MC and is more pronounced for low energy particles.

From a modeling perspective, it is fortunate that these soft collisions typically involve only small angular deflections with little or no energy transfer to the medium. Thus, as first described by Berger [5], many soft collisions can be approximated as one larger, "condensed-history" step using multiple scattering models. Such CHMC methods must be carefully designed to offer meaningful improvements in computational efficiency while maintaining a sufficient number of steps to ensure simulation accuracy. A schematic comparison of a realistic "event-by-event" electron track and a condensed-history electron track is shown in Figure 7.2.

7.3 General-purpose Monte Carlo codes

General-purpose MC codes are radiation transport toolkits that utilize condensed-history techniques for a wide range of applications, usually in the keV to GeV or TeV range [8]. There are many general-purpose MC codes, which are often developed and maintained by large research institutions or research collaborations [1]. A review of many of these codes was recently conducted by Andreo et al. [1]. Additional "user codes" can be built upon these general-purpose codes to modify or extend their functionality. This section provides an overview of the following two codes, a general-purpose code and a user code, that were used in the study described in the next chapter:

1. The general-purpose **Ge**ometry **an**d **T**racking version **4** (Geant4) toolkit [9–11].

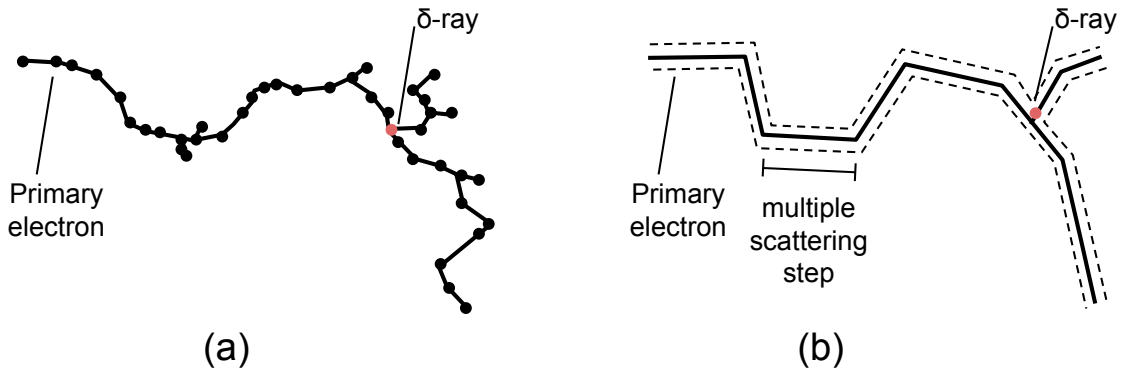

Figure 7.2 Schematic comparison of (a) a realistic electron track and (b) a condensed-history electron track. The realistic electron track includes many soft collisions represented as black circles and a single hard collision represented as a red circle. The condensed-history track approximates many soft collisions using a smaller number of multiple scattering steps. Notice that the hard collision resulting in a δ-ray is preserved in the condensed-history approach. Dotted lines around the condensed-history track represent the approximate region of energy deposition around the primary track in the realistic scenario, which is not accounted for in condensed-history. Figure adapted from Nahum [6] and Rogers and Bielajew [7].

2. The **To**ol for **Pa**rticle **S**imulation (TOPAS) software project; a user code built using Geant4 [12, 13].

7.3.1 Geant4

The Geant4 toolkit is a CHMC code that was developed by the international Geant4 collaboration, which has roots at the European Organization for Nuclear Research (CERN) [9]. Geant4 was developed using the object-oriented C++ programming language and is provided to users under an open-source license. Geant4 was first released in 1998 and is currently on version 10.7.p2.

Geant4 facilitates MC transport of many particle species over a wide range of energies, spanning from keV to PeV [11, 14]. Geant4 has therefore been widely adopted in many fields, including high energy physics, space science, and medical physics. Among the most notable features of Geant4 is its offering of an extensive variety of models to describe various physics processes [9]. A physics process is essentially defined as an interaction between a particle and an absorber with an energy-dependent cross section (as described in Chapter 2). On the other hand, a model describes the characteristics of the products of a particular interaction. In many

cases Geant4 offers multiple models of the same physics process that may span different energy ranges (complementary models), or that may span the same energy range but offer a trade-off between accuracy and speed (competing models).

Geant4 is well-suited to users that want to develop their own MC applications. To create a new application, the user must define the following aspects of the simulation using custom C++ classes [9]:

- The physics processes to be considered and the models used to describe each process. Geant4 provides many curated lists of physics processes and models that are known as physics constructors.
- The physical geometry and material compositions of all components in the irradiated region of interest. Within Geant4, any geometry component can be made "sensitive" such that it records a physical quantity of interest.
- A source of particles with which to irradiate the specified geometric region of interest.

Other notable features of Geant4 include the functionality to (i) visualize both the geometry and particle tracks of a simulation in real-time, (ii) optimize the simulation of many primary particles via multithreading, and (iii) allow replication of identical geometry components in complex setups in order to drastically reduce memory consumption [9, 11].

Overall, Geant4 is an extremely powerful and robust simulation code. Its main drawbacks are the requirement for application developers to know the C++ programming language and the steep learning curve associated with the Geant4-specific syntax.

7.3.2 TOPAS

TOPAS is a user code that was developed by Perl et al. [12], which wraps and extends Geant4. In the context of TOPAS, wrapping refers to the fact that when a TOPAS MC application is run, it is actually run using Geant4 in the background. However, TOPAS is structured in a unique way and provides a distinct user interface. Indeed, TOPAS was originally developed to simplify the user complexity associated with Geant4 and thereby lower the barrier to entry for clinical medical physicists and researchers wishing to perform MC simulations in the context of proton therapy. However, the scope of TOPAS has broadened to other forms of radiation therapy and research since the initial public release in 2015 [13]. TOPAS is currently on release

version 3.6.p1 and is freely available to researchers who work in association with non-profit organizations.

The fundamental paradigm change that makes TOPAS more user-friendly than Geant4 is the capability to develop and run MC applications without requiring any C++ programming. This feat is achieved via a parameter control system that enables users to specify simulation parameters within a text-based parameter file that is written in a structured ASCII format [12]. An example parameter file and visualization of the corresponding MC application are shown in Figure 7.3.

Expert users of TOPAS with C++ programming knowledge can make use of the TOPAS Extensions Framework [13]. The TOPAS Extensions Framework allows users to develop their own geometry components, physics lists, particle sources, and scorers. These extensions are developed as C++ classes with a custom TOPAS style that borrows heavily from Geant4 syntax but includes a variety of extra helper functions to streamline development.

A major advantage of TOPAS relative to Geant4 is the ease by which custom-developed MC applications can be shared. For example, a parameter file and possibly a few extension files are all that is required to share and run a TOPAS application.

7.4 Track-structure Monte Carlo codes

TSMC codes facilitate the simulation of secondary electrons down to the low energies at which excitations and ionizations take place. Most of the available TSMC codes only include physics models for interactions in liquid water or water vapor, which have an excitation threshold around 10 eV. The application of condensed-history techniques to these low energy electrons is not recommended because of the associated loss in spatial accuracy [15], as illustrated in Figure 7.2. Thus, track-structure simulations model charged particle transport in a fully “analogue” manner to emulate real particle tracks as closely as possible. By overlaying these realistic particle tracks on cellular (μm) and subcellular (nm) geometries, one can simulate radiation-induced biological damage. Although TSMC simulations are inherently more computationally intensive than CHMC simulations, they are necessary when simulating biological effects like DNA damage.

When using TSMC methods, there are generally two approaches to simulate radiation-induced direct DNA damage [14]:

```
#-----------------------------------------------------
# Geometry
#-----------------------------------------------------
# World
d:Ge/World/HLX=50. cm
d:Ge/World/HLY=50. cm
d:Ge/World/HLZ=80. cm
s:Ge/World/Material = "Vacuum"

# Phantom
s:Ge/Phantom/Type="TsBox"
s:Ge/Phantom/Parent="World"
d:Ge/Phantom/HLX=20. cm
d:Ge/Phantom/HLY=20. cm
d:Ge/Phantom/HLZ=20. cm
s:Ge/Phantom/Material = "G4_WATER"
```

(a)

```
#-----------------------------------------------------
# Physics
#-----------------------------------------------------
sv:Ph/Default/Modules = 1 "g4em-standard_opt0"

#-----------------------------------------------------
# Particle source
#-----------------------------------------------------
s:So/Beam/Type = "Beam"
s:So/Beam/Component = "BeamPosition"
sc:So/Beam/BeamParticle = "gamma"
dc:So/Beam/BeamEnergy = 500 keV
s:So/Beam/BeamPositionDistribution = "Flat"
s:So/Beam/BeamPositionCutoffShape = "Rectangle"
d:So/Beam/BeamPositionCutoffX = 20. cm
d:So/Beam/BeamPositionCutoffY = 20. cm
i:So/Beam/NumberOfHistoriesInRun = 10
```

(b)

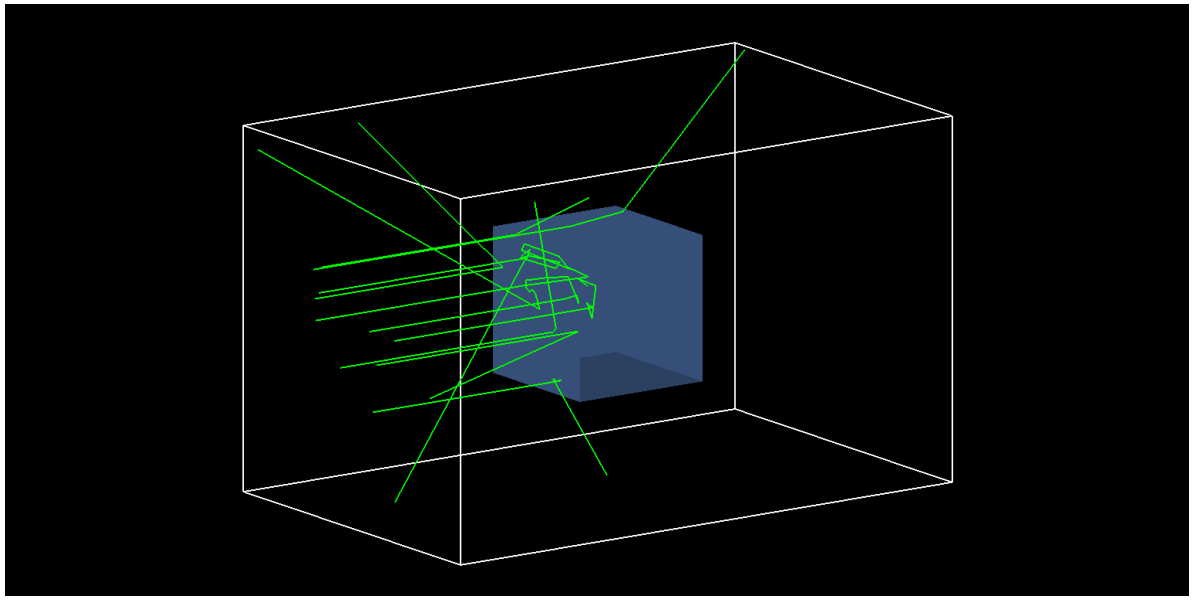

(c)

Figure 7.3 A trivial MC application designed using TOPAS to irradiate a water phantom with ten 500 keV photons. Screenshots of the entirety of the parameter file that specifies this simulation are shown in (a) and (b). Parameters are defined using the format: `Parameter_type : Parameter_name = Parameter_value`. A graphical representation of the resulting simulation is shown in (c).

1. Irradiate a homogeneous volume containing water and use microdosimetry to analyze spatial patterns in energy depositions along radiation tracks in the absence of a geometric DNA model.

2. Irradiate a geometric DNA model, record all energy depositions in the sensitive volumes of interest, and empirically convert the energy depositions to DNA damage.

The first approach has the benefit and feature that it does not require modeling the structure of DNA, which is a highly dynamic molecule that requires many assumptions to model. The second approach is required to quantify DNA damage in absolute terms but relies on many assumptions about DNA structure and the nature of how radiation energy deposition leads to DNA damage. Thus, a major aspect of the development of TSMC codes is the development of geometric models of biological structures such as nuclear DNA.

Relatively few of the TSMC codes that have been developed have been made publicly available [8]. Two notable exceptions, available under open-source licenses, are the low-energy extensions of Geant4 and TOPAS. These codes are called Geant4-DNA [8, 16–18] and TOPAS-nBio [19], respectively.

7.4.1 Geant4-DNA

Geant4-DNA is included with the public Geant4 release but is developed and maintained by a distinct group called The Geant4-DNA Collaboration [16]. The design and syntax used in Geant4-DNA is the same as Geant4, and thus the same advantages and drawbacks are shared between these codes. The main feature of Geant4-DNA is the inclusion of a variety of physics models for the analogue transport of electrons, protons, and alpha particles [8]. Also included with Geant4-DNA are a variety of biological targets implemented as geometric volumes [14].

Since its release, the functionality of Geant4-DNA has expanded to enable simulations of water radiolysis resulting from irradiation [14, 20]. These simulations include models for (i) generating free radical species, (ii) free radical diffusion, and (iii) a variety of chemical reactions. By implementing this functionality into a MC application one can simulate indirect DNA damage.

7.4.2 TOPAS-nBio

Similar to the relationship between TOPAS and Geant4, TOPAS-nBio was developed to wrap and extend the track-structure and radiation chemistry functionality provided in Geant4-DNA [19]. As described by McNamara et al. [21], TOPAS-nBio offers a greater variety of geometric models of biological targets that Geant4-DNA. Among these biological target models are various chromatin fibre models that can be used when developing MC applications to assess radiation-induced DNA damage.

An ongoing objective of the TOPAS-nBio group is to develop and incorporate tools to model biological response following radiation damage. Indeed, the following two mechanistic models of DNA repair were included in the most recent public release of TOPAS-nBio (version 1.0, released in May 2021): The DNA Mechanistic Repair Simulator (DaMaRiS) [22] and the Mechanistic DNA Repair and Survival model (MEDRAS) [23].

7.5 Monte Carlo studies to model neutron RBE

TSMC methods offer a compelling avenue to investigate the mechanisms underlying the energy dependence of neutron RBE for stochastic effects. Baiocco et al. [24] were the first to conduct such a study, which was undertaken as one component of the international ANDANTE project [25, 26] that ran from 2012 to 2016 [26]. The ANDANTE project had a broader objective to assess neutron RBE via (i) physical simulations (ii) radiobiological experiments with stem cells, and (iii) a prospective epidemiological study of second cancer rates caused by neutrons produced during paediatric proton therapy treatments.

Baiocco et al. [24] used MC simulations to develop two distinct models of neutron RBE. In the initial step of their method, the CHMC code PHITS [27] was used to determine the spectra of secondary particles produced by 10 eV–1 GeV neutrons and a reference x-ray spectrum in a human tissue phantom. Specifically, the ICRU sphere [28] was used as the tissue phantom and particle spectra were recorded in three scoring volumes at increasing depth, as shown in Figure 7.4.

For the first model, they used the microdosimetric function of PHITS [29] to approximate particle tracks with energies that were randomly sampled from the secondary particle spectra. A microdosimetric quantity called dose-mean lineal energy $\bar{y}_{\mathrm{D}}$ was calculated for all tracks, which essentially characterizes the spatial clustering of energy depositions within each track.

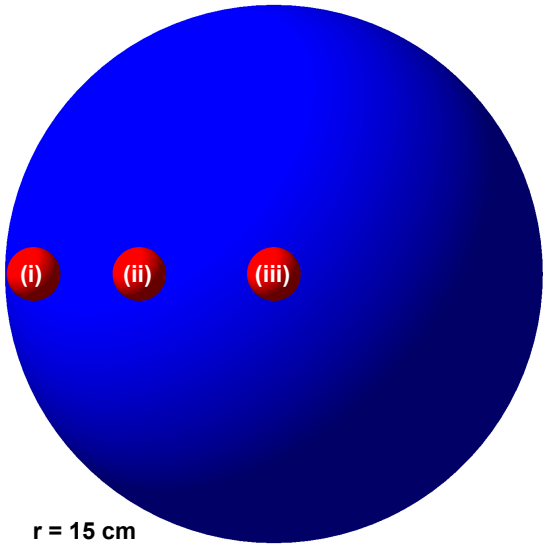

Figure 7.4 The ICRU sphere [28], containing three red scoring volumes at increasing depth: (i) outer scoring volume, (ii) intermediate scoring volume, (iii) inner scoring volume.

An estimate of neutron RBE was obtained by dividing the $\bar{y}_D$ obtained for initial neutrons by the $\bar{y}_D$ obtained for an initial 220 kV x-ray spectrum for every initial neutron energy and each scoring volume (i.e. each depth). Baiocco et al.'s [24] results that were obtained in the outer scoring volume of the ICRU sphere are shown in Figure 7.5(a).

For the second model, Baiocco et al. [24] used the TSMC code PARTRAC [33] to explicitly generate particle tracks with energies sampled from the secondary particle spectra and used these tracks to irradiate a DNA model. As a result of these irradiations, the authors scored the yield of clusters of DNA damage that contained two or more DNA DSBs within 25 bp (sometimes labeled as DSB++ lesions [33]). Similar to the first model, the authors divided the cluster yield obtained for initial neutrons by the photon-induced result to estimate neutron RBE. Estimates of neutron RBE were obtained for every initial neutron energy and for all three scoring volumes. Baiocco et al.'s [24] results for the outer scoring volume are shown in Figure 7.5(b).

The results obtained using both models exhibited similar energy dependence as the neutron weighting factors and the neutron quality factors. Thus, the work of Baiocco et al. [24] was a major milestone to link the energy dependence of neutron RBE for stochastic effects to fundamental biophysical mechanisms. However, there were two notable drawbacks to their study:

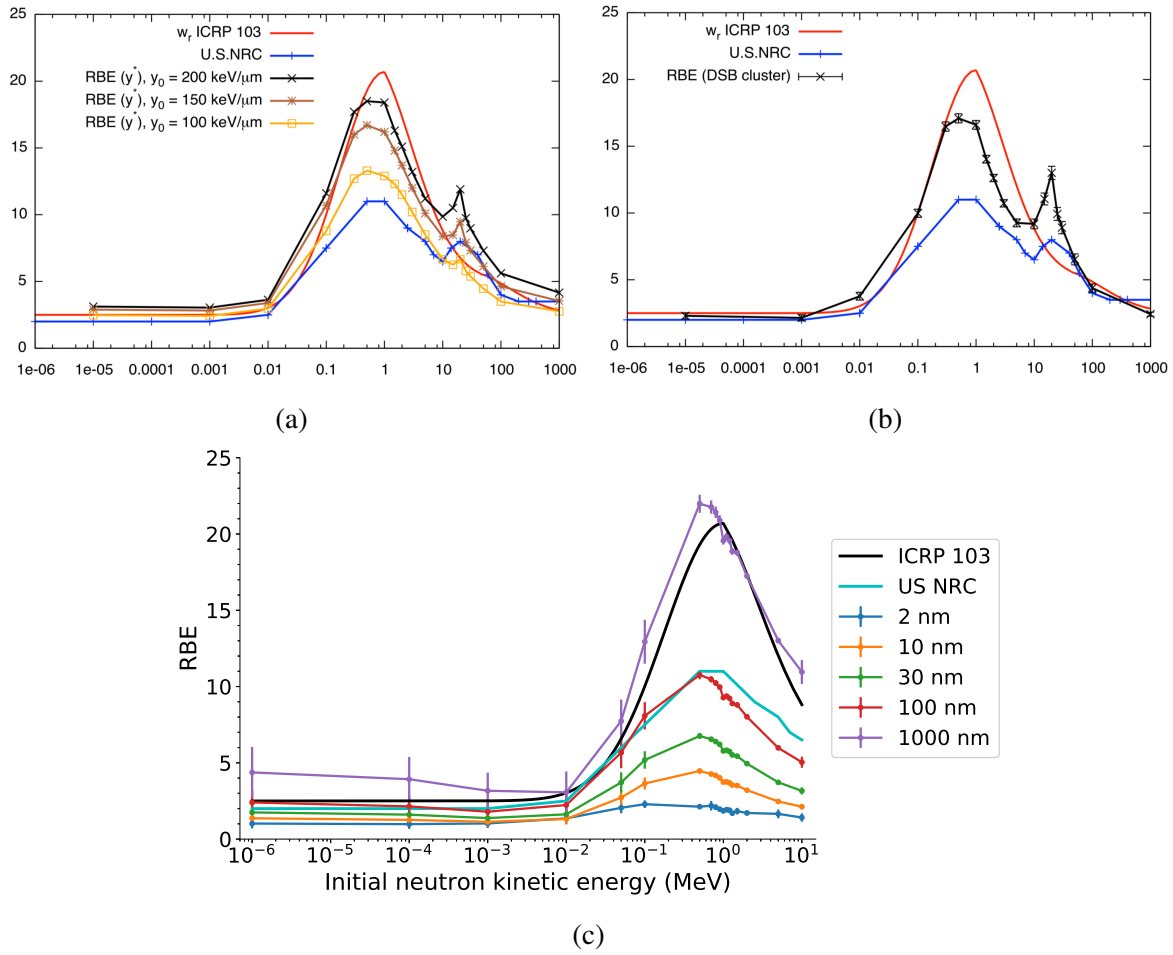

Figure 7.5 Neutron RBE plotted as a function of energy for various MC models. Results for each model are plotted alongside the ICRP neutron weighting factors [30] and the US NRC neutron quality factors [31]. (a) Neutron RBE for the microdosimetric endpoint dose-mean lineal energy, as determined by Baiocco et al. [24]. The three curves represent distinct choices of an empirical tuning parameter used when calculating $\bar{y}_{\mathrm{D}}$. (b) Neutron RBE for inducing clusters of DNA lesions that contain two or more DSBs (i.e. DSB++), as obtained by Baiocco et al. [24]. (c) Neutron RBE for the microdosimetric endpoint dose-mean lineal energy, as determined by Lund et al. [32]. Each curve represents a different scale over which clusters of energy deposition were considered when calculating $\bar{y}_{\mathrm{D}}$.

1. The use of the closed-source MC codes PHITS and PARTRAC. It is difficult to fully gauge the robustness of Baiocco et al.'s [24] methodology and results because the details of the microdosimetric PHITS function and their DNA model in PARTRAC are not readily available. Additionally, the use of closed-source code means that independent researchers wishing to expand on their work must start from scratch.

2. The consideration of a single type of clustered DNA lesion, namely those that contain at least two DSBs. As discussed in the previous chapter, a wide variety of clustered lesions are believed to have potential mutagenic consequences. Additional cluster parameters, like the distance between lesions in a cluster, are also believed to impact DNA repair and thus the mutagenic effects of clustered damage [34].

Our research group sought to address the first drawback in Baiocco et al.'s [24] study in a recent publication by Lund et al. [32]. In our study, we developed a similar model to Baiocco et al.'s [24] first model by developing a MC application with the open-source Geant4 and Geant4-DNA toolkits. In our work we explicitly simulated particle tracks in a homogeneous water phantom and used a weighted track sampling algorithm [35] to calculate $\bar{y}_{\mathrm{D}}$ values. This algorithm allowed us to assess the clustering of energy depositions on varying scales between 1 nm–1 μm and allowed us to gauge how neutron RBE may vary for different scales of biological damage (e.g. considering damage at the scale of a DNA base pair vs. at the scale of a chromosome). Our results obtained in the outer scoring volume are shown in Figure 7.5(c).

As yet, we have not publicly released our MC application for this study for various reasons, including the relative difficulty in developing user-friendly Geant4 code. Additionally, an assessment of neutron RBE for inducing a broader range of clustered DNA lesions was still outstanding when our study was published.

References

[1] P. Andreo, D. T. Burns, A. E. Nahum, J. Seuntjens, and F. H. Attix. *Fundamentals of ionizing radiation dosimetry*. John Wiley and Sons Incorporated, Weinheim, Germany, 2017.

[2] N. Metropolis and S. Ulam. The Monte Carlo Method. *Journal of the American Statistical Association*, 44(247):335–341, 1949. 10.1080/01621459.1949.10483310.

[3] M. Fippel. Basics of Monte Carlo Simulations. In J. Seco and F. Verhaegan, editors, *Monte Carlo Techniques in Radiation Therapy*, chapter 2, pages 17–28. Taylor & Francis Group, Boca Raton, 2013.

[4] E. B. Podgoršak. *Radiation Physics for Medical Physicists*. Springer International Publishing Switzerland, Swizterland, third edition, 2016.

[5] M. Berger. Monte Carlo calculation of the penetration and diffusion of fast charged particles. In B. J. Alder, S. Fernbach, and M. Rotenberg, editors, *Methods in Computational Physics, Volume 1*, pages 135–215. Academic Press Inc., New York, 1963.

[6] A. E. Nahum. Condensed-history Monte-Carlo simulation for charged particles: What can it do for us? *Radiation and Environmental Biophysics*, 38(3):163–173, 1999. 10.1007/s004110050152.

[7] D. W. O. Rogers and A. F. Bielajew. Monte Carlo techniques of electron and photon transport for radiation dosimetry. In K. R. Kase, B. E. Bjarngard, and F. H. Attix, editors, *The Dosimetry of Ionizing Radiation*, chapter 5, pages 427–539. Academic Press, San Diego, 1990.

[8] S. Incerti, et al. Geant4-DNA example applications for track structure simulations in liquid water: A report from the Geant4-DNA Project. *Medical Physics*, 45(8):e722–e739, 8 2018. 10.1002/mp.13048.

[9] S. Agostinelli, et al. GEANT4 - A simulation toolkit. *Nuclear Instruments and Methods in Physics Research, Section A: Accelerators, Spectrometers, Detectors and Associated Equipment*, 506(3):250–303, 2003. 10.1016/S0168-9002(03)01368-8.

[10] J. Allison, et al. Geant4 developments and applications. *IEEE Transactions on Nuclear Science*, 53(1):270–278, 2006. 10.1109/TNS.2006.869826.

[11] J. Allison, et al. Recent developments in GEANT4. *Nuclear Instruments and Methods in Physics Research, Section A: Accelerators, Spectrometers, Detectors and Associated Equipment*, 835:186–225, 2016. 10.1016/j.nima.2016.06.125.

[12] J. Perl, J. Shin, J. Schümann, B. Faddegon, and H. Paganetti. TOPAS: An innovative proton Monte Carlo platform for research and clinical applications. *Medical Physics*, 39 (11):6818–6837, 2012. 10.1118/1.4758060.

[13] B. Faddegon, et al. The TOPAS tool for particle simulation, a Monte Carlo simulation tool for physics, biology and clinical research. *Physica Medica*, 72:114–121, 2020. 10.1016/j.ejmp.2020.03.019.

[14] S. Incerti, M. Douglass, S. Penfold, S. Guatelli, and E. Bezak. Review of Geant4-DNA applications for micro and nanoscale simulations. *Physica Medica*, 32(10):1187–1200, 10 2016. 10.1016/j.ejmp.2016.09.007.

[15] I. Kyriakou, et al. Influence of track structure and condensed history physics models of Geant4 to nanoscale electron transport in liquid water. *Physica Medica*, 58:149–154, 2 2019. 10.1016/j.ejmp.2019.01.001.

[16] S. Incerti, et al. The Geant4-DNA project. *International Journal of Modeling, Simulation, and Scientific Computing*, 1(2):157, 2010.

[17] S. Incerti, et al. Comparison of GEANT4 very low energy cross section models with experimental data in water. *Medical Physics*, 37(9):4692–4708, 2010. 10.1118/1.3476457.

[18] M. A. Bernal, et al. The influence of DNA configuration on the direct strand break yield. *Computational and Mathematical Methods in Medicine*, page 417501, 2015. 10.1155/2015/417501.

[19] J. Schuemann, et al. A New Standard DNA Damage (SDD) Data Format. *Radiation Research*, 191(1):76–92, 2019. 10.1667/rr15209.1.

[20] M. Karamitros, et al. Modeling Radiation Chemistry in the Geant4 Toolkit. *Progress in Nuclear Science and Technology*, 2:503–508, 2011. 10.15669/pnst.2.503.

[21] A. L. McNamara, et al. Geometrical structures for radiation biology research as implemented in the TOPAS-nBio toolkit. *Physics in Medicine and Biology*, 63(17):175018, 9 2018. 10.1088/1361-6560/aad8eb.

[22] J. W. Warmenhoven, et al. Insights into the non-homologous end joining pathway and double strand break end mobility provided by mechanistic in silico modelling. *DNA Repair*, 85:102743, 2020. 10.1016/j.dnarep.2019.102743.

[23] S. J. McMahon, J. Schuemann, H. Paganetti, and K. M. Prise. Mechanistic Modelling of DNA Repair and Cellular Survival Following Radiation-Induced DNA Damage. *Scientific Reports*, 6:1–14, 2016. 10.1038/srep33290.

[24] G. Baiocco, et al. The origin of neutron biological effectiveness as a function of energy. *Scientific Reports*, 6:34033, 2016. 10.1038/srep34033.

[25] A. Ottolenghi, V. Smyth, and K. R. Trott. Assessment of cancer risk from neutron exposure - The ANDANTE project. *Radiation Measurements*, 57:68–73, 2013. 10.1016/j.radmeas.2012.10.017.

[26] A. Ottolenghi, G. Baiocco, V. Smyth, and K. Trott. The ANDANTE project: A multidisciplinary approach to neutron RBE. *Radiation Protection Dosimetry*, 166(1-4):311–315, 2015. 10.1093/rpd/ncv158.

[27] T. Sato, et al. Particle and heavy ion transport code system, PHITS, version 2.52. *Journal of Nuclear Science and Technology*, 50(9), 2013. 10.1080/00223131.2013.814553.

[28] D. R. White, J. Booz, R. V. Griffith, J. J. Spokas, and I. J. Wilson. Report 44. *Journal of the International Commission on Radiation Units and Measurements*, os23(1), 1989. 10.1093/jicru/os23.1.report44.

[29] T. Sato, R. Watanabe, L. Sihver, and K. Niita. Applications of the microdosimetric function implemented in the macroscopic particle transport simulation code PHITS. *International Journal of Radiation Biology*, 88(1-2):143–150, 2012. 10.3109/09553002.2011.611216.

[30] ICRP. ICRP 103: The 2007 Recommendations of the ICRP. *Annals of the ICRP*, 37(2-4), 2007.

[31] US NRC. Units of Radiation Dose. *Code of Federal Regulations*, 10(20.1004):298–300, 2021.

[32] C. M. Lund, G. Famulari, L. Montgomery, and J. Kildea. A microdosimetric analysis of the interactions of mono-energetic neutrons with human tissue. *Physica Medica*, 73: 29–42, 2020. 10.1016/j.ejmp.2020.04.001.

[33] W. Friedland, M. Dingfelder, P. Kundrát, and P. Jacob. Track structures, DNA targets and radiation effects in the biophysical Monte Carlo simulation code PARTRAC. *Mutation Research - Fundamental and Molecular Mechanisms of Mutagenesis*, 711(1-2):28–40, 2011. 10.1016/j.mrfmmm.2011.01.003.

[34] E. Sage and N. Shikazono. Radiation-induced clustered DNA lesions: Repair and mutagenesis. *Free Radical Biology and Medicine*, 107:125–135, 2017. 10.1016/j.freeradbiomed.2016.12.008.

[35] G. Famulari, P. Pater, and S. A. Enger. Microdosimetry calculations for monoenergetic electrons using Geant4-DNA combined with a weighted track sampling algorithm. *Physics in Medicine and Biology*, 62(13):5495–5508, 2017. 10.1088/1361-6560/aa71f6.

Chapter 8

Towards the characterization of neutron carcinogenesis through direct action simulations of clustered DNA damage

Logan Montgomery, Christopher M Lund, Anthony Landry, John Kildea

Article submitted to: *Physics in Medicine & Biology, July 2021*

8.1 Preface

With the manuscript presented in this chapter, we aimed to address the drawbacks of the previously published studies that used TSMC methods to model the energy dependence of neutron RBE for stochastic effects. Specifically, we aimed to assess neutron RBE for inducing all types of clustered DNA damage, thereby expanding on the analysis of DSB++ lesions by Baiocco et al. [1]. Additionally, we aimed to conduct this study in a fully open-source manner. To achieve these aims, we developed a novel TSMC application to score neutron-induced clustered DNA damage in a model of nuclear DNA using the highly-shareable framework of TOPAS and TOPAS-nBio. Both the development of this application and our results are presented below.

8.2 Abstract

Neutron exposure poses a unique radiation protection concern because neutrons have a large, energy-dependent relative biological effectiveness (RBE) for stochastic effects. Recent computational studies on the microdosimetric properties of neutron dose deposition have implicated clustered DNA damage as a likely contributor to this marked energy dependence. So far, publications have focused solely on neutron RBE for inducing clusters of DNA damage containing two or more DNA double strand breaks (DSBs). In this study, we have conducted a novel assessment of neutron RBE for inducing all types of clustered DNA damage that contain two or more lesions, stratified by whether the clusters contain DSBs (complex DSB clusters) or not (non-DSB clusters). This assessment was conducted for eighteen initial neutron energies between 1 eV and 10 MeV as well as a reference radiation of 250 keV x-rays. We also examined the energy dependence of cluster length and cluster complexity because these factors are believed to impact the DNA repair process. To carry out our investigation, we developed a user-friendly TOPAS-nBio application that includes a custom nuclear DNA model and a novel algorithm for recording clustered DNA damage. We found that neutron RBE for inducing complex DSB clusters exhibited similar energy dependence to the canonical neutron RBE for stochastic radiobiological effects, at multiple depths in human tissue. Qualitatively similar results were obtained for non-DSB clusters, although the quantitative agreement was lower. Additionally we identified a significant neutron energy dependence in the average length and complexity of clustered lesions. These results support the idea that many types of clustered DNA damage contribute to the energy dependence of neutron RBE for stochastic radiobiological effects and imply that the size and constituent lesions of individual clusters should be taken into account when modeling DNA repair. Our results were qualitatively consistent for (i) multiple radiation doses (including a low dose 0.1 Gy irradiation), (ii) variations in the maximal lesion separation distance used to define a cluster, and (iii) two distinct collections of physics models used to govern particle transport. Our complete TOPAS-nBio application has been released under an open source license to enable others to independently validate our work and to expand upon it.

8.3 Introduction

Reducing the long-term stochastic risk of radiation carcinogenesis is one of the primary objectives of radiation protection. Of particular concern are radiation scenarios involving neutron exposure, which include high-energy ($\gtrsim 8$ MeV) radiation therapy [2, 3], nuclear incidents [4], and space travel [5, 6]. Neutron exposure must be assessed separately from exposure to other forms of radiation because neutrons have a comparatively high and energy-dependent relative biological effectiveness (RBE) for stochastic effects. This energy dependence is encapsulated in the neutron weighting factors (w_{R}) promulgated by the International Commission on Radiological Protection [7] and the neutron quality factors (Q) published by the United States Nuclear Regulatory Commission [8]. Both sets of factors convey a marked energy dependence of neutron RBE with a peak value occurring around 1 MeV. Accordingly, radiation therapy scenarios warrant particular attention because the fluence spectrum of secondary neutrons that is generated in such environments has a fast neutron peak around 1 MeV [2, 3], coincident with maximal neutron RBE. While the secondary neutron absorbed dose associated with radiation therapy is low compared to the therapeutic dose [9], it is generally believed that stochastic radiobiological effects can occur at any dose.

Although the w_{R} and Q factors exhibit qualitatively similar energy dependences, their magnitudes are highly discrepant. This follows from the considerable variety of neutron RBE values reported by the epidemiological investigations and radiobiological experiments on which these factors are based [7, 8]. In light of these discrepancies, it is desirable to trace the origin of neutron RBE to fundamental biophysical principles, as recently asserted by Baiocco et al. [1]. To this end, consideration must be given to the mechanisms by which ionizing radiation is generally believed to cause cancer.

The somatic mutation theory of carcinogenesis [10–12] posits that genomic mutations can lead to carcinogenesis and is perhaps the most longstanding mechanistic theory of carcinogenesis. Nowadays, it is generally believed that radiation can induce mutagenesis via several pathways, including both nuclear DNA damage and non-targeted effects [13, 14]. Thus, it is of interest to characterize direct radiation-induced DNA damage as one piece of the larger puzzle of radiation-induced carcinogenesis.

The propensity of radiation to induce clusters of DNA damage, which are difficult to repair and rarely occur endogenously, has been widely theorized as the primary mechanism by which

radiation induces mutagenesis [15–19]. Therefore, one approach to evaluate the mutagenic potential of neutrons is to model their relative ability to induce clustered DNA damage.

Track-structure Monte Carlo (TSMC) techniques that utilize low-energy physics models to simulate event-by-event particle interactions can be used to model radiation-induced damage on the nanoscopic level [20, 21]. Our group recently used the open-source Geant4-DNA toolkit [22–25] to analyze neutron RBE for the microdosimetric endpoint dose-mean lineal energy at various depths in human tissue [26]. The methodology we employed was similar to an earlier study by Baiocco et al. [1] who used PHITS [27] and PARTRAC [28]. The energy dependence of the microdosimetric neutron RBE values obtained in both studies was qualitatively similar to the ICRP's w_R factors and the US NRC's Q factors. While these microdosimetric studies provide information on the spatially-clustered nature of energy deposition by neutrons and their secondary particles, they do not explicitly provide information on clustered DNA damage. To do so, a geometric model of nuclear DNA must be incorporated.

In a parallel study, Baiocco et al. [1] incorporated a geometric DNA model and evaluated neutron RBE for the direct induction of clusters of DNA lesions containing at least two double strand breaks (DSBs) within 25 bp (sometimes labeled DSB++ [28]). These results also exhibited similar qualitative energy dependence to the neutron w_R and Q factors. However, DSB++ lesions represent only a small subset of an infinite variety of clustered DNA damage lesions, each of which may have mutagenic potential. Recent experimental review papers [17–19] have discussed the mutagenic potential of clustered lesions both with and without DSBs (i.e. complex-DSB clusters and non-DSB clusters). These papers also highlighted how DNA repair is heavily influenced by the specific types and number of lesions comprising a cluster as well as the number of base pairs between them.

In this work we performed a novel assessment of neutron RBE for stochastic effects by simulating neutron RBE for the direct induction of both complex DSB clusters and non-DSB clusters. This manuscript describes how we used the TOPAS-nBio framework [29] to create a new open-source Monte Carlo application that includes a custom nuclear DNA model and a novel algorithm that records clustered DNA damage. We used our application to determine neutron RBE for inducing both types of clustered DNA damage as a function of neutron energy at multiple depths in human tissue. We also analyzed the length and number of lesions comprising each cluster in consideration of the variety of lesions encompassed by the complex DSB and non-DSB cluster types, as well as the possible variations in their mutagenic consequences.

Finally, we performed repeat simulations with variations in particular simulation parameters in order to assess the validity of key assumptions that we made.

8.4 Methods

8.4.1 Overview

Our overall methodology included four steps, which are summarized schematically in Figure 8.1.

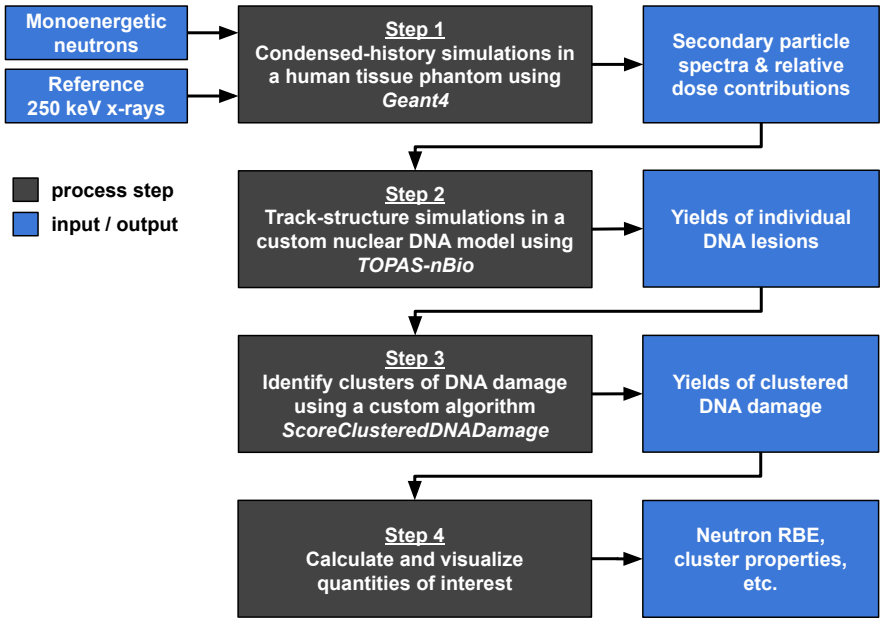

Figure 8.1 Schematic overview of our Monte Carlo simulation and analysis pipeline designed to determine direct neutron-induced DNA damage and compare with a reference radiation of 250 keV x-rays.

In step 1, condensed-history Monte Carlo simulations were used to determine the energy spectra and relative dose contributions of the secondary particles liberated in human tissue by uniform fluences of monoenergetic neutrons and a reference radiation of 250 keV x-rays. These simulations were performed in Geant4 v10.04.p02 and used the ICRU-4 sphere [30] as a human tissue phantom. Similar to the approach taken by Baiocco et al. [1], data were recorded in three scoring volumes of increasing depth. Step 1 was conducted in our previous work [26] and the resulting data were reused in this work.

In step 2, TSMC methods were used to determine the amount of DNA damage induced by the secondary particles identified in step 1. Particle tracks were stochastically sampled from the secondary particle energy spectra and used to irradiate a geometric model of nuclear DNA that we developed. Energy depositions that occurred in the sensitive nucleotide volumes were empirically converted to DNA damage lesions. These simulations were carried out using TOPAS v3.3.1 and the TOPAS-nBio 1.0 beta, which are both based on Geant4 v10.05.p01.

In step 3, the map of individual DNA lesions was processed using a novel clustering algorithm that we developed to aggregate lesions in close proximity. Clusters were then stratified according to whether at least one DSB was present (i.e. complex DSB clusters) or not (i.e. non-DSB clusters). The yields of both types of clustered DNA damage were recorded.

Finally, in step 4, we calculated neutron RBE for inducing both types of clustered DNA damage. In consideration of other cluster parameters that may impact DNA repair, we also analyzed the length, complexity, and density of each cluster.

8.4.2 Step 1: Condensed-history simulations

We have previously published our approach to condensed-history simulations [26]. In short, Geant4 was used to simulate the irradiation of the ICRU-4 soft tissue-equivalent sphere [30], which contained three sensitive scoring volumes at increasing depth, as shown in Figure 8.2(a). A separate irradiation was performed for (i) 18 different neutron energies ranging from 1 eV to 10 MeV (i.e. the energy range of interest in linac-based radiation therapy) and (ii) a reference radiation of 250 keV x-rays. Each irradiation consisted of a uniform fluence of 1×10^{10} primary particles.

For each scoring volume, we recorded the energy spectra and relative dose contributions of all secondary particle species liberated by each initial particle energy. Representative results obtained in the intermediate scoring volume are shown in Figure 8.2.

In general, all secondary particle species that were generated in a scoring volume were immediately killed and recorded to the appropriate secondary particle spectra and relative dose contribution. However, special consideration was given to electrons generated above 1 MeV since Geant4-DNA does not currently handle their transport [25, 26]. Instead of being killed, these electrons were allowed to propagate further and were tracked down to 1 MeV. The resulting 1 MeV electron and all other higher-order electron tracks produced during the slowing down process were recorded as independent tracks. Additionally, in step 2, we

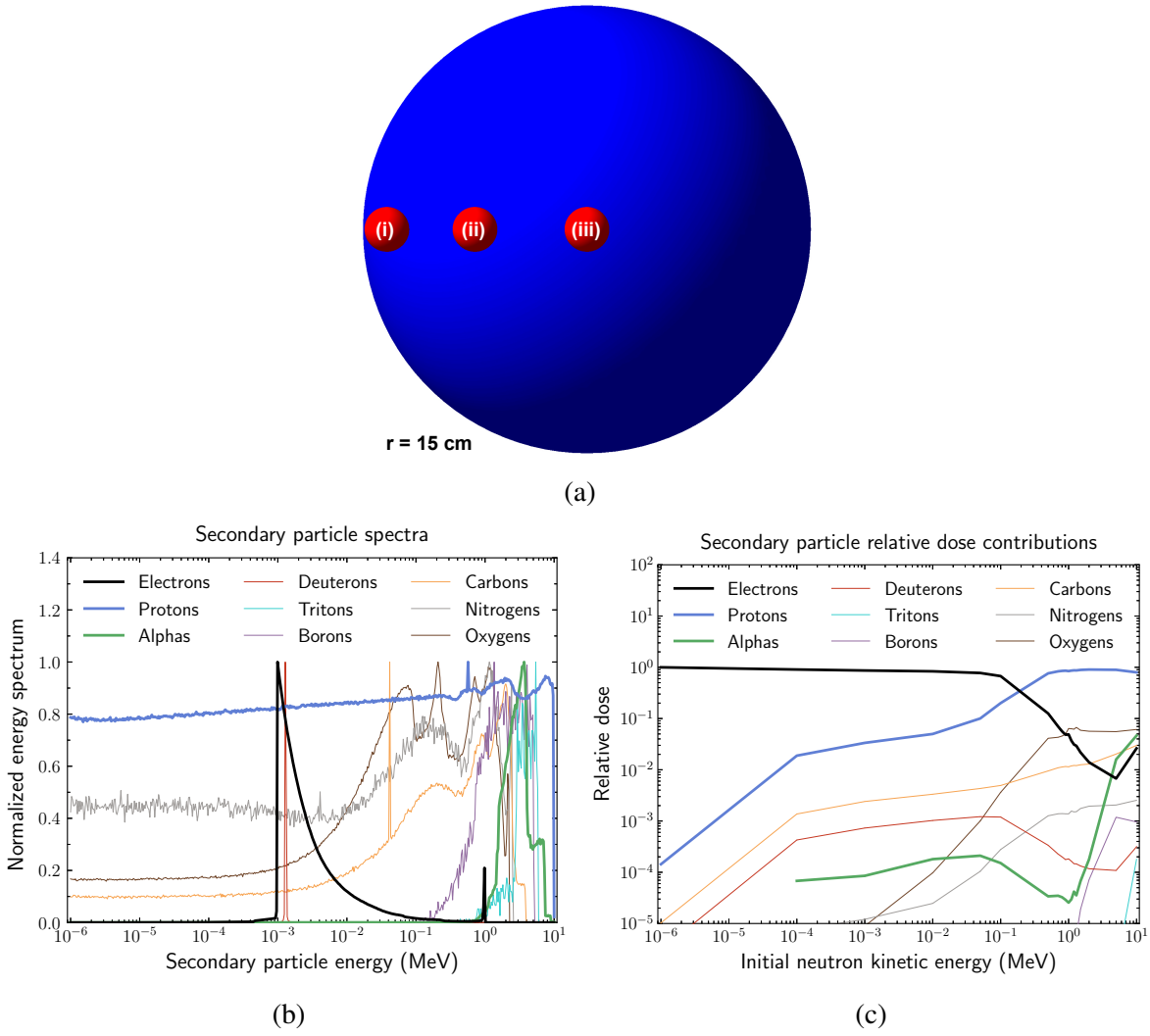

Figure 8.2 Irradiation geometry and representative results from the condensed-history Monte Carlo simulations performed in our previous work [26]. (a) Our irradiation target, the ICRU-4 soft tissue phantom [30] and three scoring volumes shown in red: (i) outer, (ii) intermediate, and (iii) inner. (b) Normalized secondary particle energy spectra produced by initial 10 MeV neutrons in the intermediate scoring volume. (c) Relative dose contribution of secondary particles in the intermediate scoring volume as a function of initial neutron energy. Particle species represented with thicker lines (i.e. electrons, protons, and alpha particles) were the only species considered in this work.

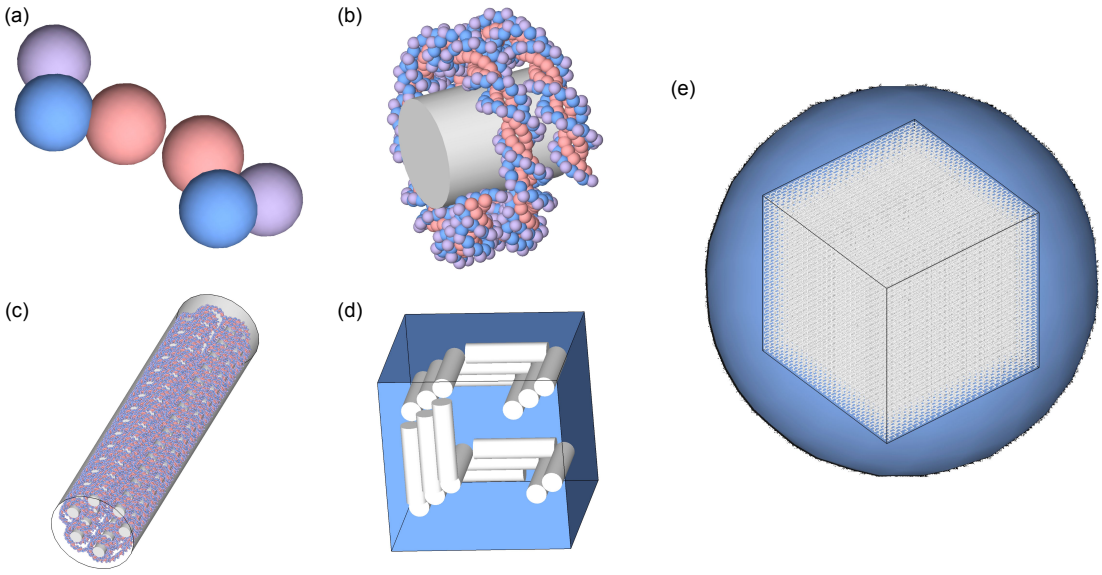

Figure 8.3 Our nuclear DNA model. (a) Nucleotide base pair containing two nitrogenous bases (red), two deoxyribose molecules (blue) and two phosphate groups (purple). (b) Nucleosome containing 154 base pairs arranged in a double helix and wrapped around a cylindrical volume representing a histone protein complex. (c) Chromatin fibre containing 90 nucleosomes arranged in a helical pattern and each connected via 46 base pairs of linker DNA. (d) Voxel containing 20 chromatin fibres arranged in a fractal pattern. (e) Cubic human fibroblast nucleus containing 6.3 Gbp of DNA, enclosed in a spherical cell volume.

considered only three secondary charged particle species: (i) electrons, (ii) protons, and (iii) alpha particles, because Geant4-DNA does not currently include complete physics models to handle the transport of heavier ions at the energies of interest [31].

8.4.3 Step 2: Track-structure simulations

Nuclear DNA model

Despite an abundance of nuclear DNA models that are described in the literature [28, 32–37], there were no complete open-source models available at the time of this study. Thus, we constructed a custom nuclear DNA model using the TOPAS extensions framework. A graphical overview of our DNA model is presented in Figure 8.3 and a summary of the geometric parameters describing it is provided in Table 8.1.

Table 8.1 Parameters describing our geometric model of nuclear DNA.

Component	Parameter	Value
DNA base pair	Nitrogenous base radius	0.30 nm
	Deoxyribose radius	0.29 nm
	Phosphate group radius	0.27 nm
Nucleosome	Histone complex dimensions	2.4 nm radius, 5.72 nm height
	Number of bp per nucleosome	154 bp (+ 46 bp of linker DNA)
Chromatin fibre	DNA content per chromatin fibre	90 nucleosomes (18 000 bp)
	Chromatin fibre radius	17 nm
	Chromatin fibre length	136 nm
Voxel	Number of fibres per voxel	20 fibres
	Voxel dimensions	0.3 μm × 0.3 μm × 0.3 μm
Nucleus	Number of voxels	17 576 voxels (26 × 26 × 26 grid)
	Volume	475 μm^3
	Number of base pairs	6.3 Gbp
	Density of DNA	13.3 Mbp/μm^3
Cell	Volume	2000 μm^3

Our chromatin fibre model is a re-implementation of a model that was developed by Villagrasa et al. [38], the source code of which was included in the TOPAS-nBio beta release [39, 40]. We ported this source code from Geant4 to TOPAS format to allow parameters to be read in from a TOPAS parameter file. In our model, nucleotide base pairs were created using six spheres to represent two nitrogenous bases, two deoxyribose molecules, and two phosphate groups (Figure 8.3(a)). These spheres were cut in some locations to prevent geometric overlap. Nucleosomes were formed by wrapping a cylindrical histone complex with 154 nucleotide base pairs arranged in a double helix (Figure 8.3(b)). Ninety nucleosomes were then linked together in helical fashion to fill out a cylindrical chromatin fibre (Figure 8.3(c)).

We constructed a nuclear model by creating multiple copies of our chromatin fibre model using a voxelized approach, similar to the method described by Zhu et al. [36]. Each voxel was filled with 20 chromatin fibres that were arranged in the fractal pattern shown in Figure 8.3(d). Using a fractal arrangement of chromatin fibres is justified by experimental evidence on the nature of chromatin folding reported by Lieberman-Aiden et al. [41] and is now commonplace

in DNA modeling [33, 36, 37, 39]. Identical voxels were placed on a cubic grid using Geant4 replica volumes. This was a simple and computationally-efficient way to create a nucleus-sized volume with 6.3 Gbp of DNA at a density of 13.3 Mbp/μm^3, consistent with human nuclei [36, 42].

The resulting 475 μm^3 nucleus model was placed in a 2000 μm^3 spherical cell volume to simulate a fibroblast in G_0/G_1 phase (Figure 8.3(e)), consistent with the fibroblast dimensions described by Seaman et al. [43]. The majority of recently published Monte Carlo investigations of radiation-induced DNA damage have used fibroblast models [1, 32, 36, 37]. Fibroblasts are an appealing choice of cell to model because they are proliferative, are found throughout the human body, and are not overly specialized like a neuron or a red blood cell.

The entire cellular volume was treated as liquid water with a density of 1 g·cm^{-3} except in the nucleotide volumes where a density of 1.407 g·cm^{-3} was used [36, 44]. In order to allow subsequent identification of clustered DNA damage, unique ID numbers were used to identify each: (i) voxel, (ii) chromatin fibre, (iii) DNA strand, (iv) nucleotide, and (v) molecule within each nucleotide.

To benchmark our DNA model against previously published results, we irradiated it with monoenergetic protons (500 keV, 1 MeV, and 10 MeV) and recorded the resulting direct DNA single strand breaks (SSBs) and double strand breaks (DSBs), as defined in Section 8.4.4. The total number of strand breaks (SBs) was calculated as the number of SSBs plus twice the number of DSBs (two strand breaks per DSB) to enable comparison with the literature. We compared our direct SB and DSB yields with analogous results obtained by Zhu et al. [36], Meylan et al. [32], and Sakata et al. [37], each of whom used their own nuclear DNA model. Although the irradiation conditions varied between authors, this exercise allowed us to assess the consistency of our results with published data. Our setup most closely emulated the setup of Zhu et al. [36] by placing the initial protons at random locations on the nuclear surface with a random inward orientation and by using the G4EmDNAPhysics_option2 physics constructor [25] to govern particle transport.

Physics settings

In Geant4-DNA (and thus TOPAS-nBio), there are a variety of competing physics models that describe the physical processes governing electron transport in liquid water [25]. These processes include ionization, electronic excitation, vibrational excitation, elastic scattering, molecular attachment, and Auger electron emission. Geant4-DNA offers a variety of physics

constructors, i.e. collections of physics models, from which users can choose. Among these are the G4EmDNAPhysics_option2 (opt2) and the G4EmDNAPhysics_option4 (opt4) constructors. The physics models included in the opt4 constructor are more recent and sophisticated than the models included in opt2. However, the opt4 physics models can only be used for electrons between 10 eV and 10 keV. On the other hand, the physics models included in opt2 can be used from 10 eV up to 1 MeV.

In our previous work [26], we developed a custom Geant4-DNA physics constructor, labeled G4EmDNAPhysics_hybrid2and4, in order to extract the best features of the opt2 and opt4 constructors. Our hybrid constructor uses the physics models from opt4 up to 10 keV and the models from opt2 at higher energies up to 1 MeV. In this work, we imported G4EmDNAPhysics_hybrid2and4 into TOPAS-nBio as a custom physics module and used it in our simulations. Consistent with recommendations by the TOPAS collaboration [45], electron tracks with kinetic energy less than 10 eV were killed and their energy was deposited locally.

Only a single set of physics models is provided for protons and for alpha particles in Geant4-DNA [25] and thus there is no variation across physics constructors, including our hybrid constructor.

Irradiation setup

As indicated schematically in Figure 8.1, source particle energies for our track-structure simulations were obtained by stochastically sampling the neutron secondary particle spectra described in Section 8.4.2. Particles were placed randomly throughout the cell volume (including the nucleus) with random orientation. This approach was chosen to emulate the manner in which secondary particles were generated and recorded in the upstream condensed-history simulations and is consistent with the work of Baiocco et al. [1].

For each scoring volume k and initial neutron or x-ray energy E, particles were simulated until 1 Gy of dose was delivered to the nucleus. A target dose D_0 of 1 Gy was chosen for consistency with recent literature [1, 34–36]. Additional simulations were performed with alternative D_0 values to assess dose dependence, as described in Section 8.4.6. A delivered dose equal to D_0 was achieved by running three distinct simulations, one for each secondary particle species i and a corresponding species-specific target dose $[D_i(E)]_k$. This species-specfic target dose was set as D_0 scaled by the relative dose contribution for a particular species i, at a particular neutron energy E, and in a particular scoring volume k. Each simulation was terminated once the species-specific target dose was delivered, but only after complete

processing of the current event (i.e. the current source particle track and any secondary tracks). Thus, the target dose $[D_i(E)]_k$ was slightly exceeded in every simulation and accounted for by recording the actual delivered dose $[d_i(E)]_k$.

Every simulated irradiation was repeated 100 times using pseudorandom seed values to obtain statistically independent results. Simulations were performed on our internal computer cluster that contains 212 threads across 106 cores. While the specifics varied between configurations, each simulation required no more than a few thousand source particles and ten minutes of simulation time.

8.4.4 Step 3: DNA damage clustering algorithm

Energy depositions in the sensitive DNA volumes (i.e. the nitrogenous bases, deoxyribose molecules, and phosphates) were recorded for each irradiation described in Section 8.4.3. A custom TOPAS scorer was developed to process these energy depositions and to record five types of DNA damage:

1. Single strand breaks (SSBs)
2. Base lesions
3. Double strand breaks (DSBs)
4. Complex DSB clusters
5. Non-DSB clusters

Schematic examples of each of these damage types are shown in Figure 8.4. The definition of each type of damage and the associated rationale is described in the remainder of this section.

An SSB was recorded when the cumulative energy deposited in the sugar-phosphate molecules of a nucleotide (i.e. the backbone) exceeded 17.5 eV. This energy threshold is based on the findings of Charlton and Humm [46] who modeled the experimental work of Martin and Haseltine [47] to analyze SSB induction by Auger electrons emitted by iodine-125. Use of this threshold is standard in the field [32, 33, 36, 48–50].

A base lesion was recorded when the cumulative energy deposited in a nitrogenous base exceeded 17.5 eV. Compared to SSBs, fewer simulation studies have considered base damage and there is no consensus as to which interactions lead to a base damage or the optimal energy

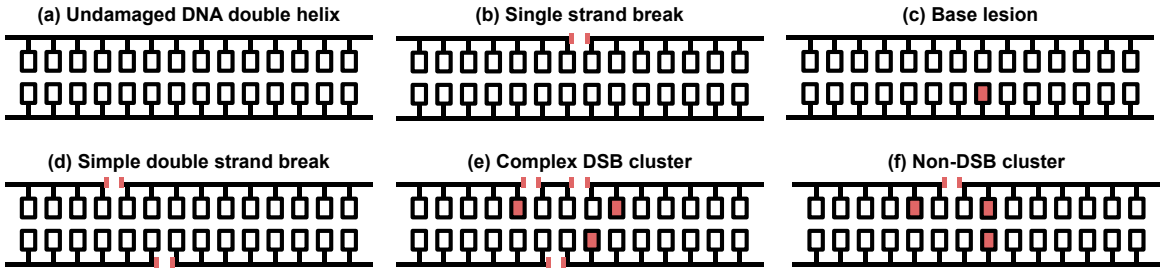

Figure 8.4 Schematics examples of the types of DNA damage considered in our simulations. (a) An undamaged DNA double helix wherein each square represents a nitrogenous base attached to the sugar-phosphate backbone. (b) A single strand break (SSB) depicted as a red separation in the backbone. (c) A generic base lesion depicted as a red base. (d) A double strand break (DSB) containing two SSBs on opposing strands within 10 base pairs of each other. (e) A complex DSB cluster containing two or more damage sites, including at least one DSB, each within 40 base pairs of each other. (f) A non-DSB cluster containing two or more SSBs or base lesions, each within 40 base pairs of each other.

threshold at which it occurs [32]. Indeed, radiation-induced base damage encompasses a diverse array of lesions including apurinic sites, apyrimidic sites, and oxidized bases [19]. Despite the lack of consensus, there is precedent for generically scoring base lesions and applying the same threshold as used for SSBs [48, 49, 51].

A DSB was recorded when two SSBs occurred within 10 bp of each other on opposing strands of the DNA double helix (i.e. within approximately one turn of the DNA double helix), as is standard in the field [32, 33, 36, 37, 48–50]. This maximum separation distance is based on experimental evidence by Van der Schans [52] who evaluated the maximum SSB separation above which DSBs would not occur in bacteriophage DNA.

Complex DSB clusters and non-DSB clusters were identified by using our custom DNA damage clustering algorithm to process the list of recorded SSBs, base lesions, and DSBs. Any two or more lesions were included in a cluster if they occurred within 40 bp of each other, i.e. within a few turns of the DNA double helix and close enough to impact DNA repair [17–19]. If the resulting cluster contained one or more DSBs we labeled it as a complex DSB cluster, otherwise we labeled it as a non-DSB cluster.

A summary of our “default” simulation parameters is provided Table 8.2. Since all research involving modeling requires a variety of assumptions that can impact the results, we designed our code such that the simulation parameters can be readily modified by the user using a TOPAS-style parameter file. We used this functionality to perform additional simulations with

variations in some of these parameters in order to assess their impact on our results, as described in Section 8.4.6.

8.4.5 Step 4: Quantities of interest

DNA damage yields

DNA damage yields $[Y_i^j(E)]_k$ were recorded for all five types of DNA damage j, and for each particle species i, initial neutron energy E, and scoring volume k (i.e. penetration depth).

The species-specific damage yields were combined via a weighted sum to get the total neutron-induced yield for a particular type of DNA damage, initial neutron energy, and scoring volume as follows:

$$[Y_N^j(E)]_k = \sum_{i=1}^{I} \frac{[Y_i^j(E)]_k [D_i(E)]_k}{[d_i(E)]_k}$$

Dose weighting was necessary to normalize the yields to the same target dose D_0, which facilitated unbiased comparison with the reference 250 keV x-rays.

A similar calculation was performed for the reference x-ray radiation, however in this case there was only one secondary particle species (electrons, denoted as e) and one initial energy, 250 keV.

$$[Y_X^j]_k = \frac{[Y_e^j]_k [D_e(E)]_k}{[d_e(E)]_k}$$

The mean neutron-induced and x-ray-induced yield for each simulation configuration was obtained by averaging 100 statistically independent simulations. The standard deviation of the mean yield (sometimes called the standard error of the mean) [53] was determined by dividing the corresponding standard deviation by the square root of the number of simulations.

Relative biological effectiveness (RBE)

Neutron RBE for inducing each type of DNA damage j was calculated as a function of neutron energy E by dividing the mean neutron-induced yield by the corresponding mean x-ray-induced yield, in each scoring volume k, as follows:

$$[\mathrm{RBE}^j(E)]_k = \frac{[Y_N^j(E)]_k}{[Y_X^j]_k}$$

Table 8.2 Default simulation parameters.

Parameter	Value
Target geometry	Nuclear DNA Model described in Table 8.1.
Target material	Liquid water Density = 1.407 g·cm^{-3} in the sensitive DNA volumes, 1 g·cm^{-3} elsewhere.
Physics Module	G4EmDNAPhysics_hybrid2and4 Custom physics constructor that uses physics models from G4EmDNAPhysics_option2 between 10 eV–10 keV and physics models from G4EmDNAPhysics_option2 between 10 keV–1 MeV.
Source particles	Electrons, protons, or alpha particles. Energies stochastically sampled from neutron and x-ray secondary particle spectra.
Simulation cutoff	1 Gy Scaled by the relative dose contribution of the source particle species being simulated (1 Gy total across all species for each initial neutron or x-ray energy in each scoring volume).
Number of histories	Variable Between 1–10 000 histories per simulation.
Number of repeated simulations	100
Induction of SSB	17.5 eV Cumulative energy deposit in the sugar-phosphate molecules comprising a nucleotide.
Induction of base lesion	17.5 eV Cumulative energy deposit in a nitrogenous base.
Induction of DSB	Two SSBs within 10 bp on opposing strands.
Induction of clustered DNA damage	Aggregation of individual DNA lesions within 40 bp of each other. If cluster contains a DSB, labeled as a complex DSB cluster. If not, labeled as a non-DSB cluster.

This metric is technically a radiation effects ratio (RER), as described by Shuryak et al. [54]. An RER compares the effects of two radiation qualities at the same dose, while RBE compares the radiation dose required by two radiation qualities to achieve the same effect. However, as in our previous study, we opted to use the more familiar RBE nomenclature for consistency with the literature [1, 26, 35]. The uncertainty in RBE was obtained by propagating the standard deviation of the mean neutron-induced and x-ray-induced yields using conventional uncertainty propagation rules.

Cluster length

The length of every recorded DNA damage cluster was obtained by calculating the number of base pairs separating the damage lesions at either end of the cluster (including the endpoints). The mean cluster length was calculated separately for complex DSB clusters and non-DSB clusters in all three scoring volumes and for each initial neutron or x-ray energy. The corresponding standard deviation of the mean was calculated accordingly.

Cluster complexity

The complexity of every recorded DNA damage cluster was calculated as the number of individual lesions (SSBs or base lesions) within each cluster. A DSB was simply interpreted as two SSBs for the purpose of this analysis. The mean cluster complexity was calculated separately for complex DSB clusters and non-DSB clusters in all three scoring volumes and for each initial neutron or x-ray energy. The corresponding standard deviation of the mean was calculated accordingly.

Cluster density

The density of every recorded DNA damage cluster was calculated as the cluster complexity divided by the cluster length. The mean cluster density was calculated separately for complex DSB clusters and non-DSB clusters in all three scoring volume and for each initial neutron or x-ray energy. The corresponding standard deviation of the mean was calculated accordingly.

8.4.6 Dose and parameter sensitivity analysis

Motivated by previous investigations by Pater et al. [55] and Zhu et al. [56], we conducted a dose and parameter sensitivity analysis to evaluate the impact of various assumptions that we made in our simulations. We identified the target dose D_0, the DNA damage clustering distance, and the physics constructor as the parameters that were the most crucial in interpreting our results and that had not been investigated previously. We repeated our full set of simulations with variations in these parameters in order to gain further insight into our results and to assess their robustness.

Dose

Because a primary motivation for this work lies in understanding radiation-induced effects leading to carcinogenesis at low doses, it was necessary to repeat our analysis in the low-dose regime (in addition to the standard 1 Gy used for consistency with the literature). While a precise definition of the low-dose regime is lacking, its upper limit is often set at approximately 0.1 Gy [7, 57–59]. Therefore we performed another set of simulations with the target dose D_0 set at 0.1 Gy. To get a sense of the linearity of our results with respect to dose, we also performed a set of simulations with a D_0 of 2 Gy.

DNA damage clustering distance

We identified a range of DNA damage clustering distances that were utilized in published Monte Carlo studies that considered clustered DNA damage in some capacity [1, 33, 34, 48, 49]. The minimum and maximum values of this range were 10 bp and 100 bp, respectively. Our default 40 bp clustering distance represented an intermediate value in this range and was consistent with the general belief that adjacent lesions within a few turns of the DNA double helix can impact the DNA repair process [17–19]. To assess the sensitivity of our results to this choice, we repeated our simulations using the 10 bp minimum and 100 bp maximum clustering distances obtained from our literature review.

Physics constructor

Finally, we evaluated the impact of our choice to use the opt4 physics models at low electron energies (below 10 keV) instead of the opt2 physics models. We did so by simply repeating our

simulations with the opt2 constructor instead of our hybrid constructor. Note that we did not compare with the opt4 constructor alone because it does not handle inelastic interactions over the full range of electron energies that we considered.

8.5 Results and discussion

In this section we present and discuss a representative subset of the results obtained in our simulations. The results that we felt did not offer additional insight are provided in the supplementary materials for completeness.

8.5.1 Benchmarking our nuclear DNA model

Total SB ($Y^{\mathrm{SSB}} + 2Y^{\mathrm{DSB}}$) and DSB yields induced by monoenergetic protons via direct effects are plotted alongside other published results in Figure 8.5. We have only compared DSB yields with Zhu et al. [36] because the other studies did not explicitly distinguish directly-induced DSBs from indirectly-induced DSBs. Although every study used a different nuclear DNA model and different irradiation conditions, all the results are of the same order of magnitude and do not vary significantly with energy. The differences in magnitude are consistent with model variations in both the size of the sensitive DNA volumes and the overall density of DNA in the nucleus. For example, both Zhu et al. [36] and Meylan et al. [32] modeled a hydration shell [60] around their nucleotide base pairs, in which energy depositions were accumulated with those in the molecules. This resulted in a larger effective volume of their sugar-phosphate backbone, and corresponded to higher SB yields. Additionally, the model used by Zhu et al. [36] had the highest DNA density of 14.4 $\mathrm{Mbp}/\mu\mathrm{m}^3$ while the model used by Sakata et al. [37] had the lowest DNA density of 12 $\mathrm{Mbp}/\mu\mathrm{m}^3$. Overall, our results are in reasonable agreement with published work, which serves to benchmark our nuclear DNA model.

8.5.2 DNA damage yields

Yields of all five types of DNA damage obtained in the intermediate scoring volume are plotted as a function of initial neutron energy in Figure 8.6(a). Without consideration of indirect effects, we cannot compare absolute damage yields with results obtained from radiobiological experiments. Nevertheless, the relative difference in yields of each type of DNA damage can

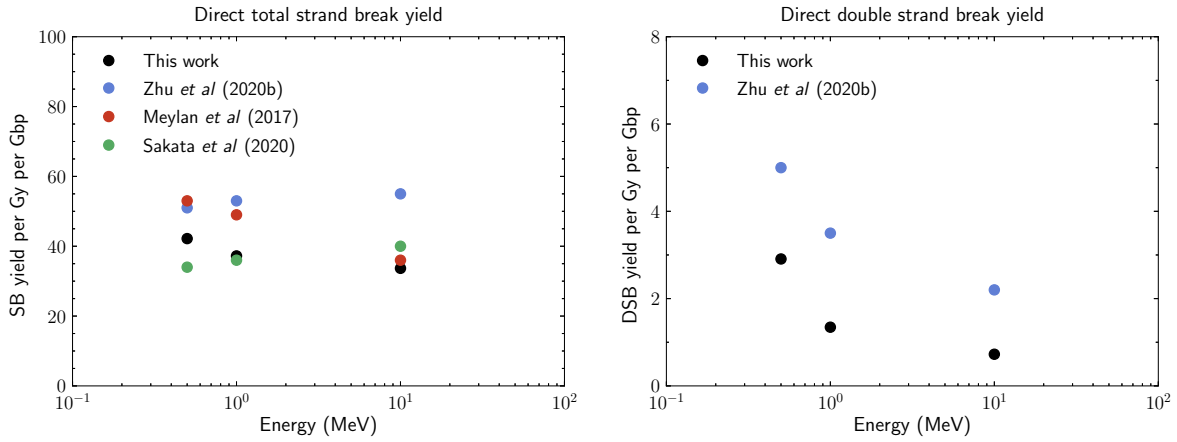

(a) (b)

Figure 8.5 Comparison of proton-induced DNA damage yields obtained using our nuclear DNA model with published results obtained using other nuclear DNA models. (a) Total strand break yield. (b) Double strand break yield.

be assessed. Approximately two times more SSBs were induced than base lesions, which is accounted for by the fact that the combined volume of the sugar-phosphate backbone is approximately twice that of the nucleotide bases in our model. We observed an increase in aggregate damage yields (DSBs, complex DSB clusters, and non-DSB clusters) beginning around 100 keV and a corresponding decrease in the yield of isolated lesions (SSBs and base lesions). As described in microdosimetric terms in our previous work [26], this trend occurs due to a change in dominance of the relative dose contribution from electrons to protons around 100 keV (intersection of the black and blue curves in Figure 8.2(c)). The yield of non-DSB clusters was several times greater than the yield of complex DSB clusters, which agrees well with predictions by Magnander and Elmroth [17] and Nikitaki et al. [61].

Figure 8.6(b) and Figure 8.6(c) demonstrate the depth dependence of clustered DNA damage yields by comparing the results obtained in each scoring volume. The peak height was relatively consistent across all scoring volume depths for both types of clustered DNA damage likely due to the fact that the shape of the secondary particle spectra did not drastically change with depth [26]. However, we observed that this peak began at higher initial neutron energies with increasing depth. This shift coincided with a shift in the neutron energy at which the relative dose contribution becomes dominated by protons with increasing depth [26]. Ultimately, this result can be traced back to increased neutron moderation with increased penetration depth in human tissue.

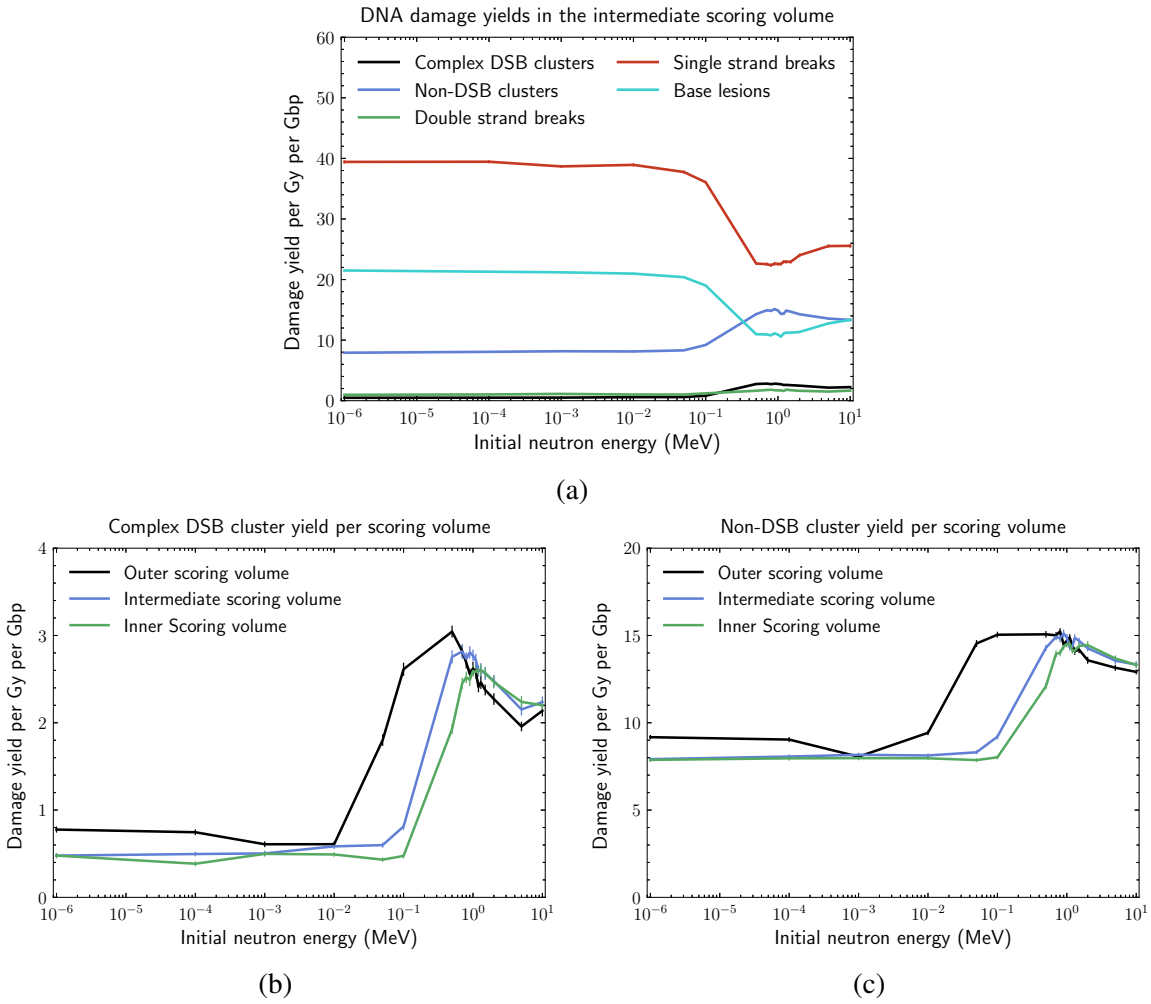

Figure 8.6 DNA damage yields per Gy of dose delivered per Gbp as a function of initial neutron energy. (a) DNA damage yield for all five types of DNA damage in the intermediate scoring volume. (b) Complex DSB cluster yield in each of the three scoring volumes. (c) Non-DSB cluster yield in each of the three scoring volumes. Plotted values are the mean values obtained over 100 statistically independent simulations. Error bars represent the standard deviation of the mean and are too small to be seen in some cases.

8.5.3 Neutron relative biological effectiveness (RBE)

Neutron RBE values for inducing all five types of DNA damage in the intermediate scoring volume are plotted as a function of initial neutron energy in Figure 8.7(a). We observed that neutron RBE for inducing complex DSB clusters exhibited a sharp increase around 100 keV with a peak value of 8.0 ± 0.6 at 700 keV. Neutron RBE for inducing non-DSB clusters and simple DSBs similarly exhibited an increase around 100 keV but with smaller peak values of 2.28 ± 0.05 and 2.2 ± 0.1 respectively. Associated with the increase in neutron RBE for aggregate damage lesions was a decrease in neutron RBE for isolated SSBs and base lesions. These trends follow logically from the observed trends in DNA damage yield (Section 8.5.2).

Figure 8.7(b) shows how neutron RBE for inducing complex DSB clusters varied with scoring depth. As with the complex DSB cluster yields shown in Figure 8.6(b), we saw that the characteristic increase in neutron RBE began at higher neutron energies with increasing depth. The peak neutron RBE value was relatively consistent across all depths within the allotted uncertainties, having a maximum value of 8.1 ± 0.6 in the outer scoring and a minimum value of 6.9 ± 0.5 in the inner scoring volume. These findings are qualitatively consistent with our previous microdosimetric results [26]. Figure 8.7(c) shows the analogous results obtained for non-DSB clusters for which a comparable depth dependence was observed. While the peak values are significantly lower than for complex DSB clusters, they exhibit similar energy dependence and have an RBE value significantly larger than 1.

In Figure 8.7(b) we also compared our results for inducing complex DSB clusters with the more specific DSB++ result obtained by Baiocco et al. [1], as well as the ICRP w_R [7] and US NRC Q factors [8]. This comparison was not explicitly included on the non-DSB cluster plot (Figure 8.7(c)) so that the axes could be magnified and the depth dependence more clearly seen. The comparison with Baiocco et al. [1] highlights the fact that neutrons have variable propensity for inducing specific types of clustered lesions relative to x-rays. One could review the literature to identify other clustered lesions of interest that are believed to have high mutagenic potential, and isolate their results from the broader classifications that we employed here. However, overall we observed good qualitative agreement between our results, the results of Baiocco et al. [1], and the reference w_R and Q factors. We thus conclude that the propensity of neutrons to induce a variety of direct clustered DNA damage lesions, both with and without DSBs, is a promising mechanism to explain the energy dependence of neutron RBE for stochastic radiobiological effects. Quantitative agreement was not expected at this

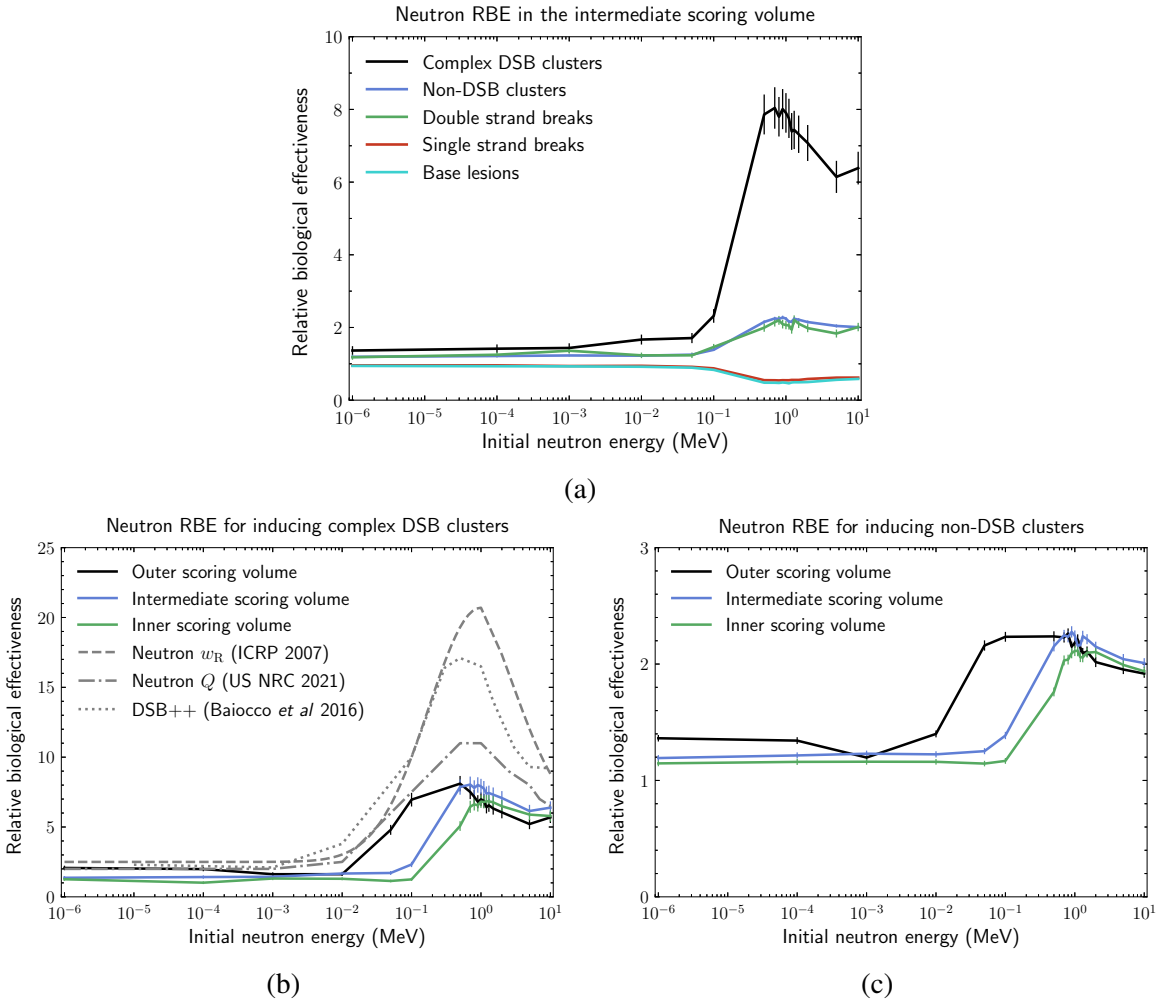

Figure 8.7 Neutron RBE for inducing DNA damage, as a function of initial neutron energy. (a) Neutron RBE for inducing five types of DNA damage in the intermediate scoring volume. (b) Neutron RBE for inducing complex DSB clusters in three scoring volumes of increasing depth. Results are compared with the ICRP neutron weighting factors [7], the US NRC neutron quality factors [8], and neutron RBE for DSB++ induction as obtained by Baiocco et al. [1]. (c) Neutron RBE for inducing non-DSB clusters in three scoring volumes of increasing depth. Plotted values are the mean values obtained over 100 statistically independent simulations. Error bars represent the standard deviation of the mean.

stage because we have not considered the indirect effects of radiation, subsequent DNA repair, or other carcinogenic pathways (like non-targeted effects).

8.5.4 Cluster length, complexity, and density

In addition to overall damage yields, we considered cluster length, cluster complexity, and cluster density as factors that may impact the DNA repair process and thus relate to stochastic effects. Figure 8.8 demonstrates the dependence of these quantities on neutron energy and compares them with the results obtained using the reference 250 keV x-ray radiation. Again, only results obtained in the intermediate scoring volume are shown here, as we found no significant depth dependence.

At low neutron energies below about 100 keV, there was no significant difference in the average complex DSB cluster length between neutrons and the reference x-rays. However, the average cluster length increased by about 30–50%, from 8 bp at 1 eV to a maximum of $\sim$12 bp at 10 MeV. Similarly, the average complex DSB cluster complexity increased by about 30% from $\sim$3.5 lesions per cluster at 1 eV to a maximum of $\sim$4.5 lesions per cluster at 5 MeV. These findings were anticipated because of the onset of the dominance of proton relative dose contributions for neutrons above 100 keV and their higher LET than electrons. Given that the results for cluster length and complexity exhibited similar energy dependence, the lack of significant trend in average damage density per complex DSB was expected.

On average, complex DSB clusters were 30–50% longer than non-DSB clusters across all neutron energies. Similarly, complex DSB clusters contained 40–70% more lesions than non-DSB clusters on average. This result was expected and can largely be explained by considering that complex DSB clusters had by definition a minimum of three lesions whereas non-DSB clusters had a minimum of two. Non-DSB clusters were approximately 25% more dense than complex DSB clusters, which follows from the relative trends in cluster length and complexity.

In summary, although neutrons above 100 keV tend to produce more clusters, longer clusters, and more complex clusters than the reference x-ray radiation, they do not produce clusters with a higher density of lesions. There is a clear neutron energy dependence in cluster length and complexity relative to x-rays, even though the trend does not precisely match the characteristic energy dependence of neutron RBE for stochastic effects. These parameters should thus be investigated further when modeling the repair of clustered DNA lesions.

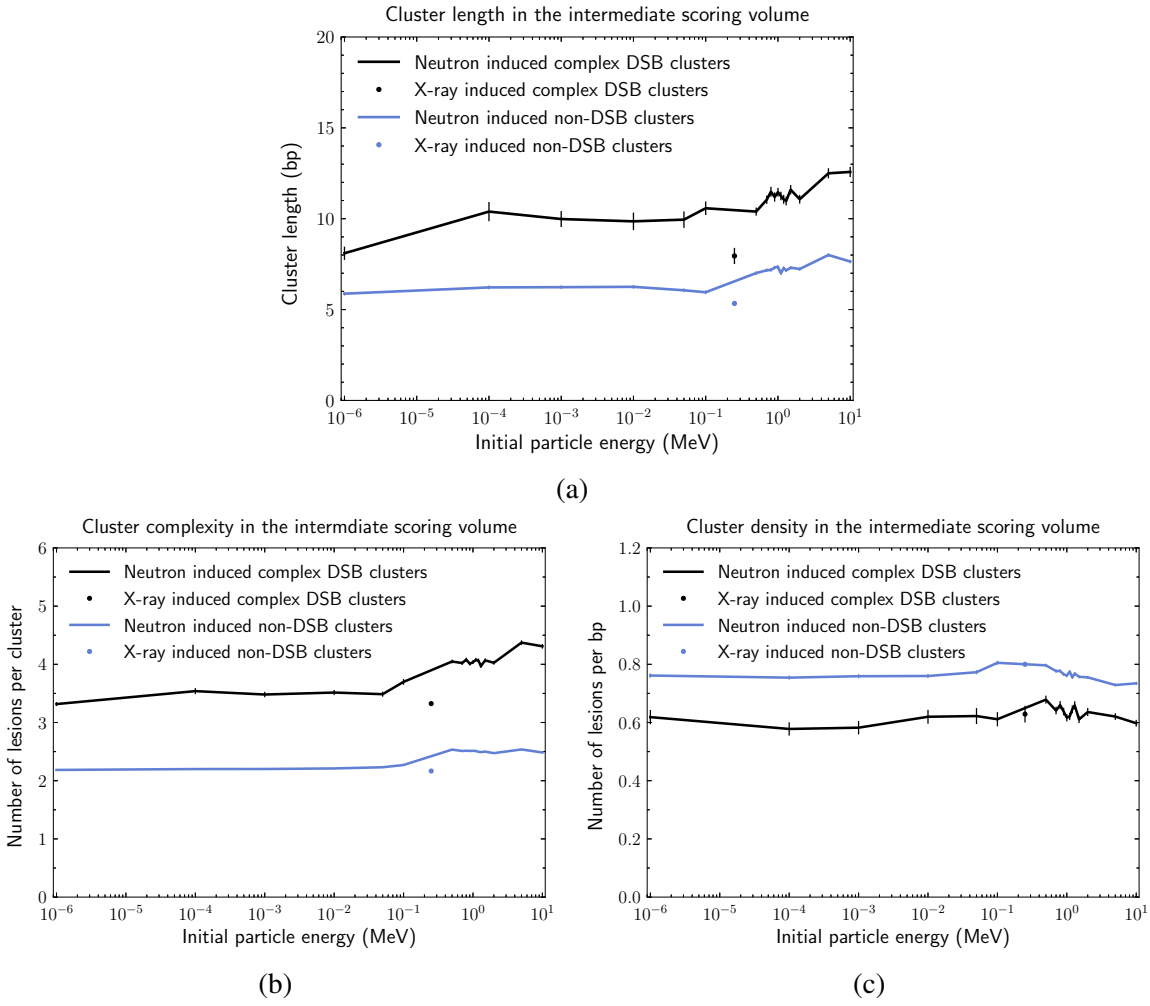

Figure 8.8 Clustered DNA damage properties of interest as a function of initial particle energy in the intermediate scoring volume: (a) cluster length, (b) cluster complexity, and (c) damage density per cluster. Plotted values are the mean values obtained over 100 statistically-independent simulations. Results for 18 initial neutron energies are plotted as a line alongside the individual result for the reference 250 keV x-ray radiation. Results for complex DSB clusters are plotted in black, while results for non-DSB clusters are plotted in blue. Error bars represent the standard deviation of the mean.

8.5.5 Dose and parameter sensitivity analysis

Dose

The impact of varying the target delivered dose D_0 on the results obtained for complex DSB clusters in the intermediate scoring volume is shown in Figure 8.9. The yield of neutron-induced complex DSB clusters was found to increase linearly with dose, as evidenced by the overlap of the dose-normalized curves in Figure 8.9(a). Correspondingly, there was no dose dependence in neutron RBE for inducing complex DSB clusters.

These findings indicate that a given cluster of DNA damage is typically caused by single-event action (i.e. a single primary track and its secondary tracks) within this dose range. Thus, our results should hold qualitatively in the low-dose regime because single event action scales linearly with dose. Our results at 0.1 Gy, nominally the upper limit of the low-dose regime, are demonstrative of this expectation.

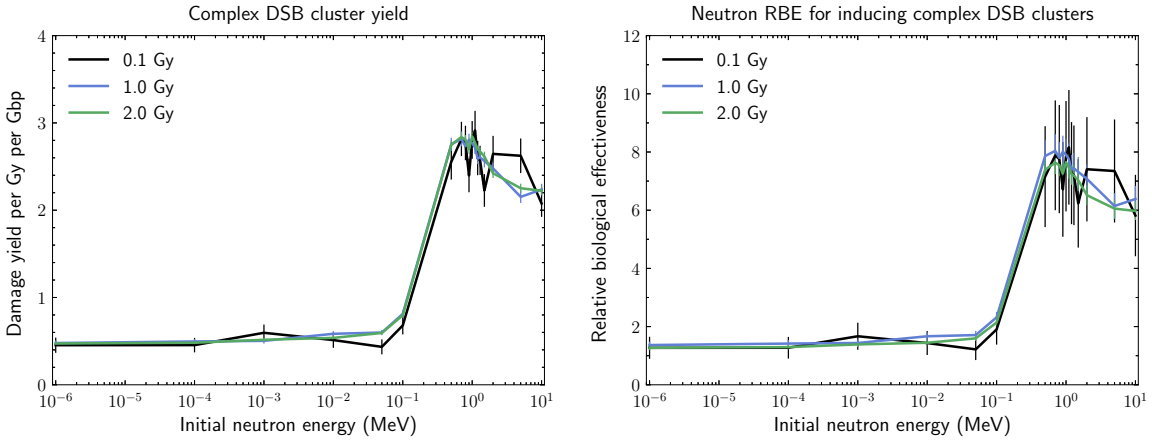

(a) (b)

Figure 8.9 Impact of varying the total delivered dose D_0 on (a) neutron-induced complex DSB cluster yield and (b) neutron RBE for inducing complex DSB clusters. Plotted values are the mean values obtained over 100 statistically independent simulations. Error bars represent the standard deviation of the mean.

Clustering distance

The impact of varying the clustering distance on the results for complex DSB clusters in the intermediate scoring volume is shown in Figure 8.10.

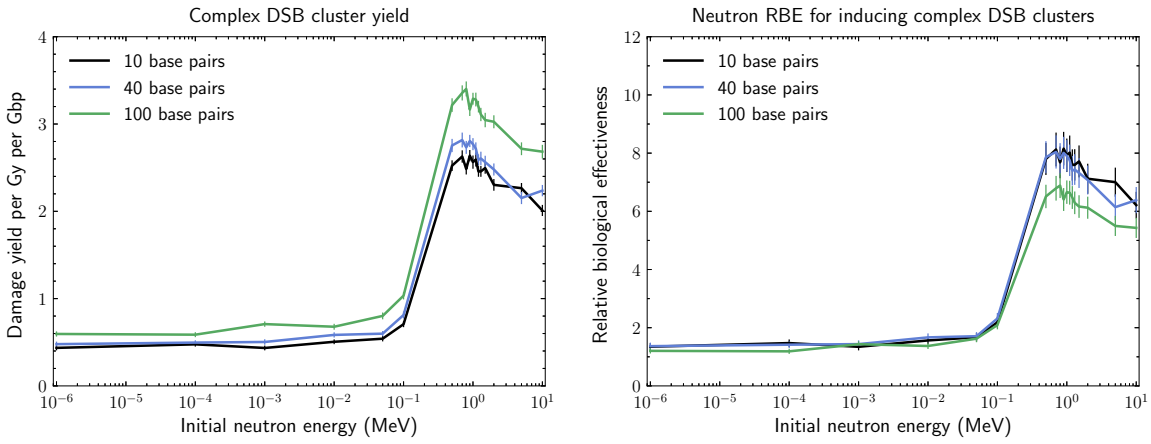

(a) (b)

Figure 8.10 Impact of varying the DNA damage clustering distance on (a) neutron-induced complex DSB cluster yield and (a) neutron RBE for inducing complex DSB clusters. Plotted values are the mean values obtained over 100 statistically independent simulations. Error bars represent the standard deviation of the mean.

Comparison of the DNA damage yields in Figure 8.10(a) revealed no significant difference for clustering distances of 10 and 40 bp. This was expected, given that the average complex DSB cluster length was found to be in the vicinity of 10 bp for all neutron energies (Figure 8.8(a)). A small but noticeable increase in yield was obtained by increasing the clustering distance to 100 bp. There are two competing effects to consider when increasing the clustering distance:

1. Formation of new clusters by combining lesions that would otherwise be treated as isolated lesions.

2. Merging of adjacent clusters that would otherwise be treated as independent clusters.

Given that the clustered damage yields increased, the predominant effect must be the former.

Comparison of neutron RBE in Figure 8.10(b) revealed that RBE decreased by increasing the clustering distance. This result may be explained by the relative LET properties of neutrons and x-rays. X-rays and their secondary electrons are low LET particles, which tend to produce isolated lesions. Meanwhile, neutrons are higher LET particles that tend to produce clusters of lesions. Thus, the previous observation that increasing the clustering distance tended to preferentially combine isolated lesions rather than adjacent clusters would result in relatively more x-ray-induced clusters than neutron-induced clusters. The net result is a decrease in neutron RBE, as we have observed in this work.

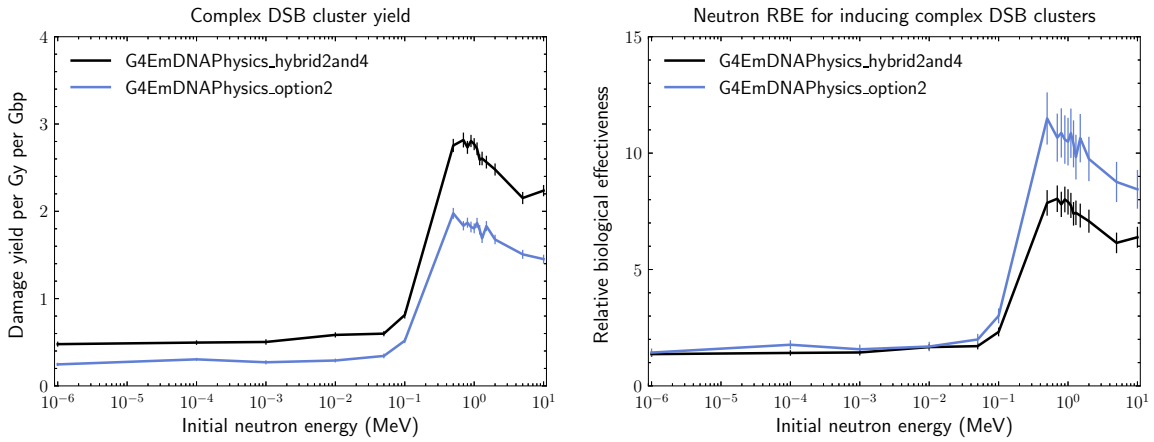

(a) (b)

Figure 8.11 Impact of varying the simulation physics constructor, and thus the underlying physics models, on (a) neutron-induced complex DSB cluster yields and (b) neutron RBE for inducing complex DSB clusters. Plotted values are the mean values obtained over 100 statistically independent simulations. Error bars represent the standard deviation of the mean.

Overall, our results were found to be qualitatively robust over the range of DNA damage clustering distances identified in our literature review.

Physics constructor

The impact of varying the physics models that govern sub-10 keV electron transport is shown for complex DSB clusters in the intermediate scoring volume in Figure 8.11. The yield was significantly larger using our hybrid constructor compared to the opt2 constructor for all neutron energies. This can be explained by expanding upon previous discussions by Kyriakou et al. [62], Bordes et al. [63], and Zhu et al. [56]. The physics models in opt2 are known to result in longer, more diffusive electron tracks than expected physically. This behaviour was "corrected" in the newer physics models included in the opt4 constructor [62] and our hybrid constructor. Thus, we expected a higher yield of clustered DNA damage induced by electrons modeled with opt4 compared to opt2, which is exactly what we observed using our hybrid constructor.

Comparison of neutron RBE in Figure 8.11(b) revealed that the peak in RBE was higher for the opt2 constructor compared to our hybrid constructor. The underlying x-ray-induced complex DSB yields per Gy per Gbp for our hybrid constructor and opt2 were 0.37 ± 0.02 and

0.18 ± 0.02, respectively. The relative difference in neutron-induced and x-ray-induced yields was larger for opt2 than our hybrid constructor, which resulted in the larger peak RBE.

Overall, this comparison of physics constructors indicated that the physics models used in the simulations have an impact on the quantitative accuracy of the results but not on the qualitative trends.

8.5.6 Limitations and future work

In this section we discuss some of the limitations of this work and, where appropriate, how they will be handled in future work.

Limitations of our nuclear DNA model

We have developed a new nuclear DNA model in a field where many models already exist and there is a lack of standardization [29]. However, we attempted to atone for this by releasing our code under an open-source license.

Additionally, our nuclear model is cubic in shape, which does not align with the generally ellipsoidal shape of fibroblast nuclei [43]. However, we believe our cubic geometry was justified given that the most important factors pertaining to DNA damage yields are (i) the overall density of DNA base pairs in the model and (ii) the size of the sensitive DNA volumes [33]. Moreover, a cubic shape was the most computationally efficient to generate and the simplest to code. Ultimately, our benchmarking analysis indicated that our model was able to produce DNA damage yields that were consistent with previous studies.

Finally, the chromatin fibres in our model were not connected to each other, which limited our ability to combine lesions in adjacent fibres into a cluster. However, we assert that the impact of this limitation was small given that:

1. Clusters were, on average, approximately 10 bp in length.
2. Only a few thousand DNA damage lesions were induced per Gy over the entire genome of $\sim$6 Gbp. (Figure 8.6(a)).

Limitations in physical modeling

Our inability to simulate secondary particle tracks heavier than alpha particles was a shortcoming of this work. Although previous studies have shown success in ignoring the effects of heavy ions

for incident neutrons with energies up to 14 MeV [35], we found that heavy ions contributed up to 14% of the dose for 10 MeV neutrons in the outer scoring volume [26]. Nevertheless, we have already calculated the energy spectra and relative dose contributions of these particles in our previous work [26]. Our methodology described in this manuscript is robust enough to handle their inclusion once physical models that describe their transport have been incorporated into the Geant4-DNA and TOPAS-nBio frameworks.

Other physical factors that may have impacted our results include:

- The treatment of electrons with energies greater than 1 MeV as uncorrelated lower energy electron tracks.
- The treatment of the entire simulation volume as liquid water.

The impact of these assumptions is difficult to predict. However, our methodology and code can facilitate rapid reassessment of these assumptions as new features become available in Geant4-DNA and TOPAS-nBio.

Limitations in modeling radiation-induced biological effects

In this study we only considered the initial landscape of direct DNA damage induced by radiation. Our research group is currently developing an update to our custom TOPAS-nBio application that incorporates the indirect effects of radiation action and will conduct a follow-up study using these updates. It is also of interest to consider how DNA repair might affect our results in order to bridge the gap between DNA damage and mutagenesis. Other groups have made great strides in modeling such DNA repair, particularly the repair of SSBs and DSBs [36, 64, 65]. We aim to to expand on our work by applying repair models such as these to our simulated DNA damage and analyzing the impact on the resulting neutron RBE.

8.5.7 Open-source code release

Our complete Monte Carlo application was developed as a TOPAS extension [66, 67] for use with TOPAS-nBio [40] and we have released it under an open-source license [68]. The following features are included:

- A nuclear DNA model implemented as a custom TOPAS geometry component.
- A physics constructor implemented as a custom TOPAS physics module.

- An algorithm for calculating clustered DNA damage yields implemented as a custom TOPAS scorer.
- A TOPAS-style parameter file to control the simulation.
- Our neutron and x-ray secondary particle energy spectra in TOPAS parameter file format.
- Our neutron and x-ray secondary particle relative dose contributions in TOPAS parameter file format.

Simulations may be readily run and configured by the user via the included parameter file. The custom components written in C++ have been extensively documented to improve readability and may be adopted or modified by users as needed. Installation requirements and instructions are provided with the code.

8.6 Conclusion

We have investigated the biophysical mechanisms underlying the energy dependence of neutron RBE for stochastic effects by simulating neutron-induced direct clustered DNA damage in a geometric DNA model. We found that neutron RBE for inducing clusters of DNA damage, both with and without DSBs, exhibited similar energy dependence to the ICRP's neutron radiation weighting factors and the US NRC's neutron quality factors. Our results support the hypothesis that a variety of clustered DNA damage lesions give rise to the energy dependence of neutron RBE for stochastic effects. We also identified an energy dependence in the average length and complexity of DNA damage clusters, indicating that these parameters should be considered when modeling mutagenic effects. Repeated simulations with variations in key parameters demonstrated the robustness of both our methodology and results, including their applicability to the low-dose regime. Our custom TOPAS-nBio application has been released under an open source license to enable others to independently validate our work and expand on it. In the future our aim is to incorporate indirect DNA damage effects and DNA repair models into our application.

8.7 Acknowledgements

This work was supported by the Natural Sciences and Engineering Research Council of Canada (Alexander Graham Bell Canada Graduate Scholarship-Doctoral: L. Montgomery, Discovery Grant: J. Kildea). Additional funding was provided to L. Montgomery from the McGill Faculty of Medicine to J. Kildea's lab from the Canada Foundation for Innovation John R. Evans Leaders Fund. We acknowledge the support of the Canadian Space Agency (CSA) (19FAMCGB25). Logistical support provided by the Prince Edward Island Cancer Treatment Centre and the Medical Physics Department at the McGill University Health Centre was invaluable for this work.

The authors would like to thank Joseph Perl for providing early access to the TOPAS source code, which informed various decisions when designing our code. We would also like to thank Nathanael Lampe for insightful discussion into the construction of complex geometry using Geant4.

All of the plots presented in this manuscript were generated using the open-source Matplotlib Python library [69].

8.8 Supplementary Material

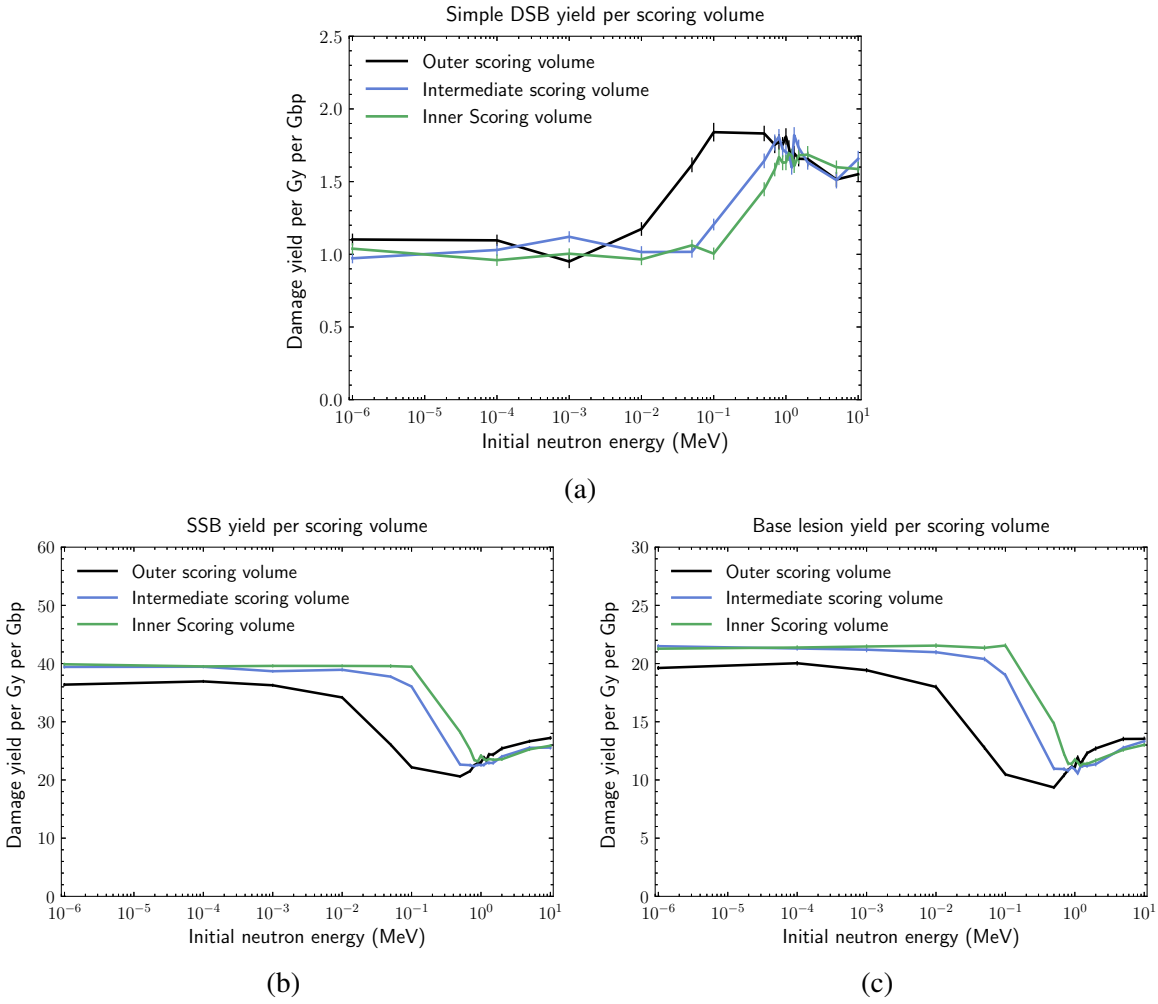

Figure 8.12 DNA damage yields per Gy of dose delivered per Gbp of DNA, as a function of initial neutron energy. (a) Simple DSB yield obtained in each of the three scoring volumes. (b) SSB yield obtained in each of the three scoring volumes. (c) Base lesion yield obtained in each of the three scoring volumes. Plotted values are the mean values obtained over 100 statistically independent simulations. Error bars represent the standard deviation of the mean and are too small to be seen in some cases.

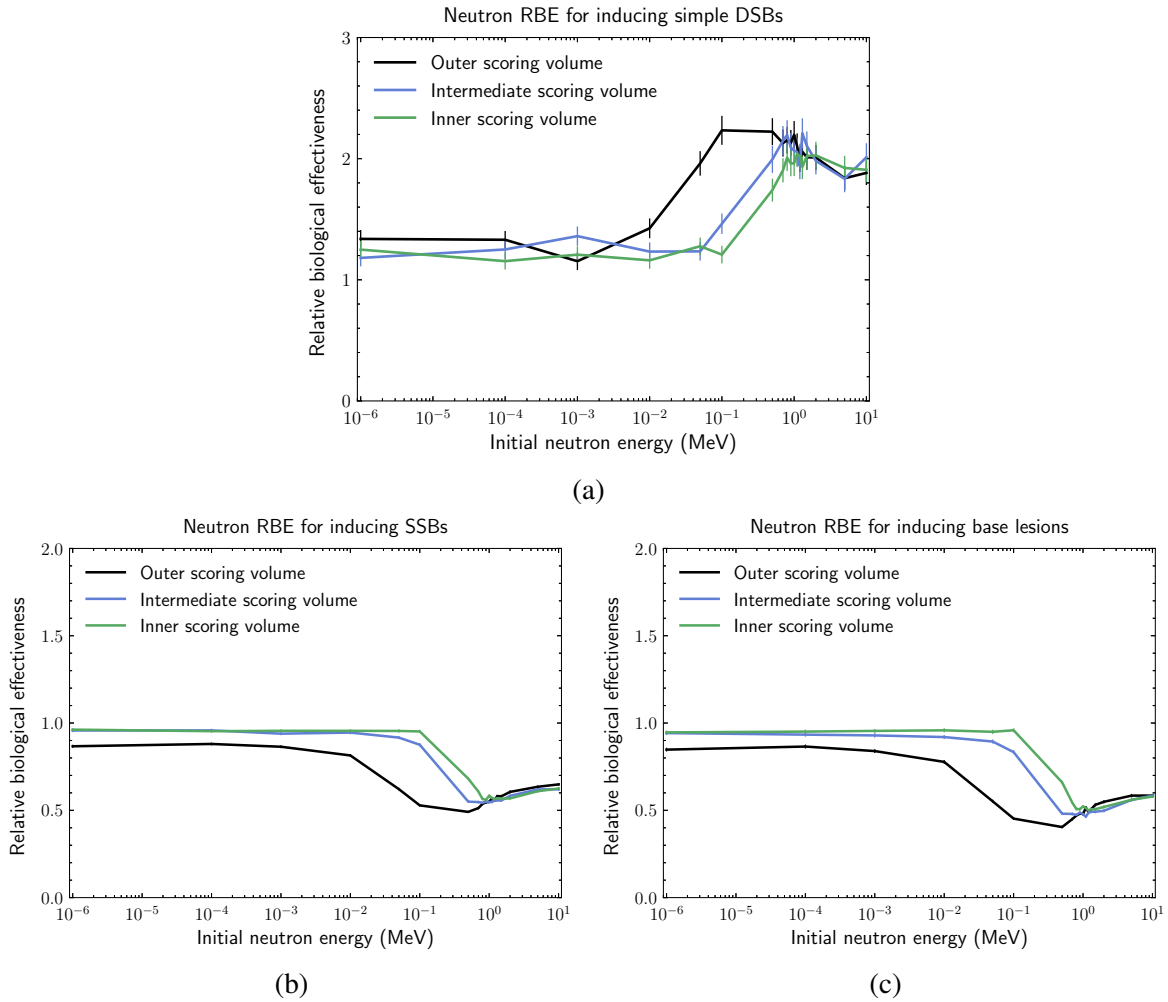

Figure 8.13 Neutron RBE for inducing DNA damage, as a function of initial neutron energy, in each of the scoring volumes. (a) Neutron RBE for inducing simple DSBs. (b) Neutron RBE for inducing SSBs. (c) Neutron RBE for inducing base lesions. Plotted values are the mean values obtained over 100 statistically independent simulations. Error bars represent the standard deviation of the mean.

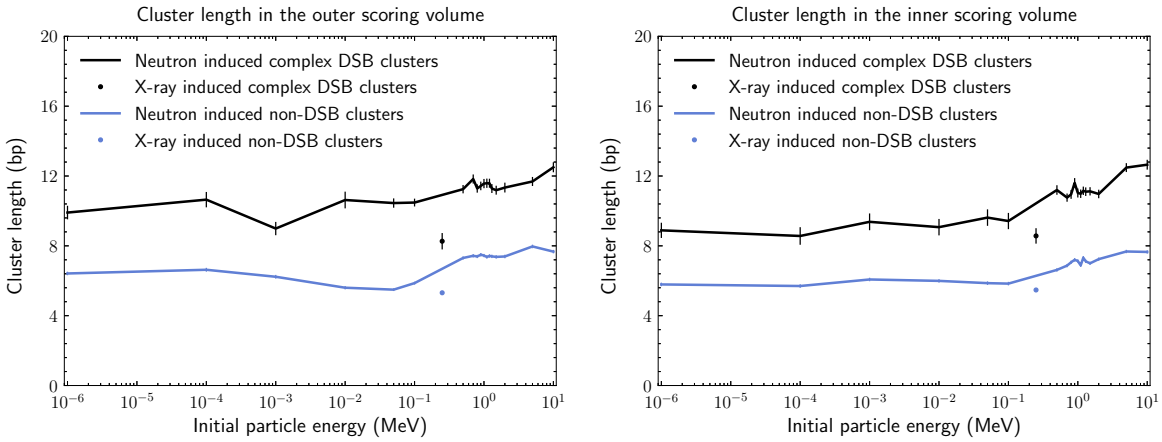

(a) (b)

Figure 8.14 Clustered DNA damage length as a function of initial particle energy. (a) Outer scoring volume. (b) Inner scoring volume. Plotted values are the mean values obtained over 100 statistically-independent simulations. Results for 18 initial neutron energies are plotted as a line alongside the result for a reference x-ray radiation, for both types of clustered damage. Results for complex DSB clusters are plotted in black, while results for non-DSB clusters are plotted in blue. Error bars represent the standard deviation of the mean.

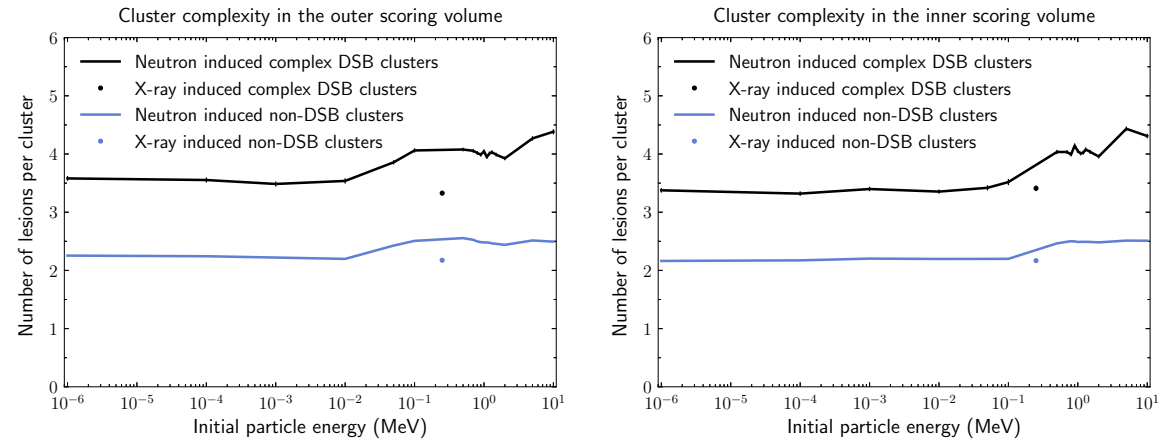

(a) (b)

Figure 8.15 Clustered DNA damage complexity as a function of initial particle energy. (a) Outer scoring volume. (b) Inner scoring volume. Plotted values are the mean values obtained over 100 statistically-independent simulations. Results for 18 initial neutron energies are plotted as a line alongside the result for a reference x-ray radiation, for both types of clustered damage. Results for complex DSB clusters are plotted in black, while results for non-DSB clusters are plotted in blue. Error bars represent the standard deviation of the mean.

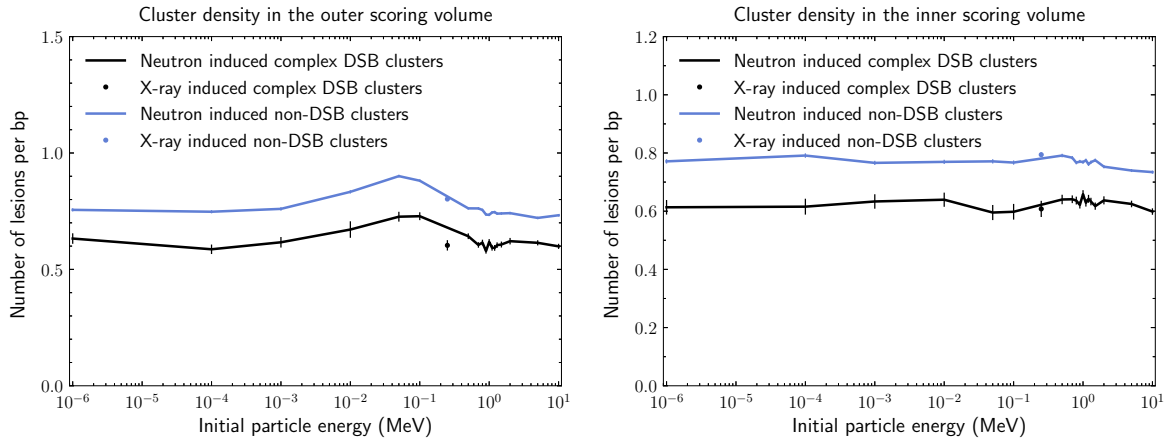

(a) (b)

Figure 8.16 Clustered DNA damage density as a function of initial particle energy. (a) Outer scoring volume. (b) Inner scoring volume. Plotted values are the mean values obtained over 100 statistically-independent simulations. Results for 18 initial neutron energies are plotted as a line alongside the result for a reference x-ray radiation, for both types of clustered damage. Results for complex DSB clusters are plotted in black, while results for non-DSB clusters are plotted in blue. Error bars represent the standard deviation of the mean.

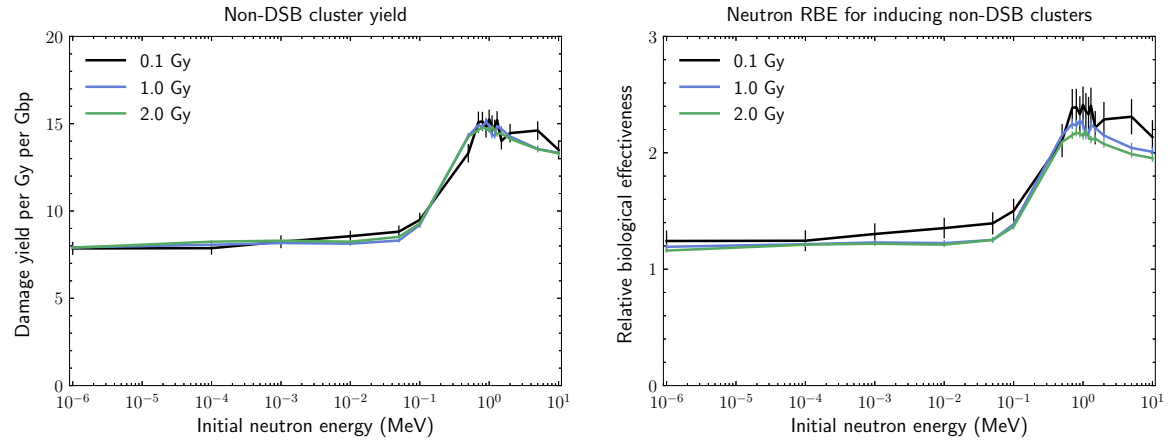

(a) (b)

Figure 8.17 Impact of varying the total delivered dose D_0 on (a) neutron-induced non-DSB cluster yield and (b) neutron RBE for inducing non-DSB clusters, in the intermediate scoring volume. Plotted values are the mean values obtained over 100 statistically independent simulations. Error bars represent the standard deviation of the mean.

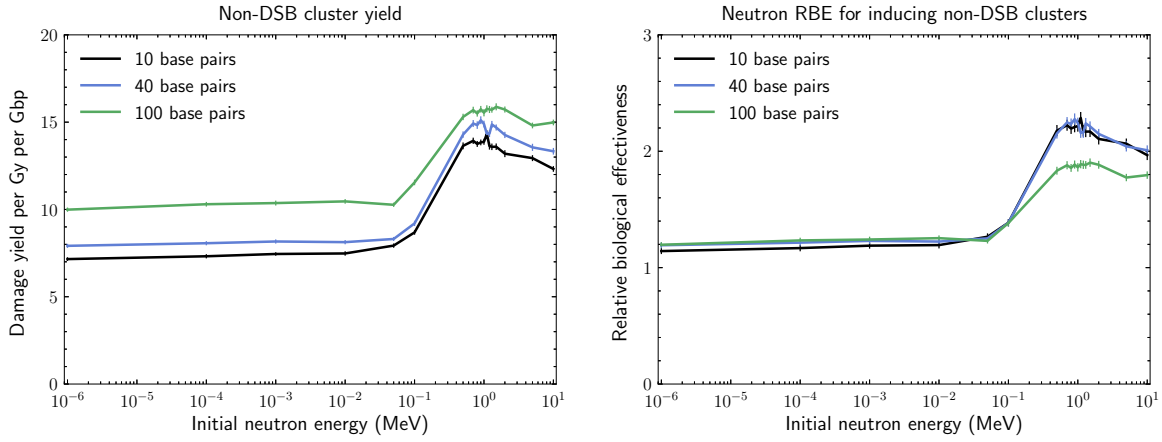

(a) (b)

Figure 8.18 Impact of varying the DNA damage clustering distance on (a) neutron-induced non-DSB cluster yield and (a) neutron RBE for inducing non-DSB clusters, in the intermediate scoring volume. Plotted values are the mean values obtained over 100 statistically independent simulations. Error bars represent the standard deviation of the mean.

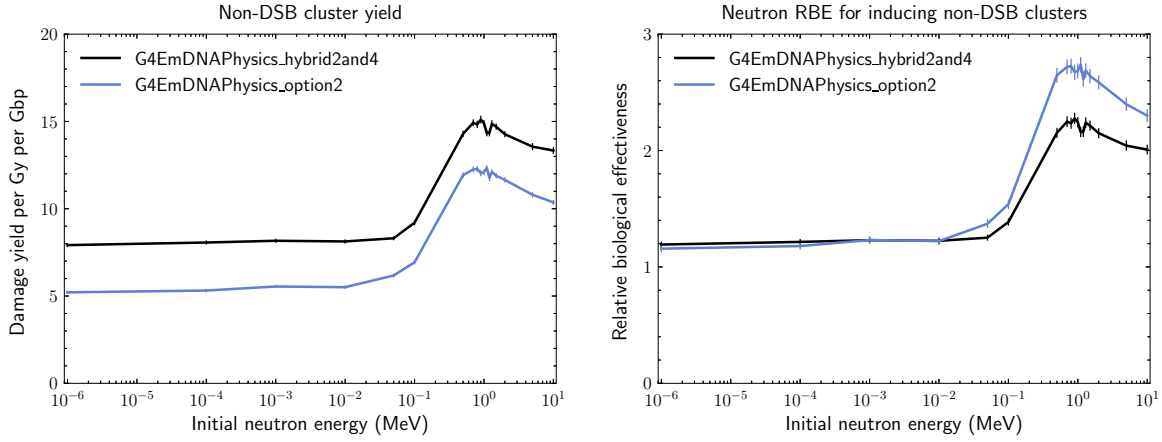

(a) (b)

Figure 8.19 Impact of varying the simulation physics constructor, and thus the underlying physics models, on (a) neutron-induced non-DSB cluster yields and (b) neutron RBE for inducing non-DSB clusters. Plotted values are the mean values obtained over 100 statistically independent simulations. Error bars represent the standard deviation of the mean.

References

[1] G. Baiocco, et al. The origin of neutron biological effectiveness as a function of energy. *Scientific Reports*, 6:34033, 2016. 10.1038/srep34033.

[2] R. M. Howell, N. E. Hertel, Z. Wang, J. Hutchinson, and G. D. Fullerton. Calculation of effective dose from measurements of secondary neutron spectra and scattered photon dose from dynamic MLC IMRT for 6 MV, 15 MV, and 18 MV beam energies. *Medical Physics*, 33(2):360–368, 2006. 10.1118/1.2140119.

[3] R. Maglieri, A. Licea, M. Evans, J. Seuntjens, and J. Kildea. Measuring neutron spectra in radiotherapy using the nested neutron spectrometer. *Medical Physics*, 42(11):6162–6169, 2015. 10.1118/1.4931963.

[4] I. Shuryak, et al. A High Throughput Approach to Reconstruct Partial-Body and Neutron Radiation Exposures on an Individual Basis. *Scientific Reports*, 10(1):1–14, 2020. 10.1038/s41598-020-59695-9.

[5] E. R. Benton, E. V. Benton, and A. L. Frank. Neutron dosimetry in low-earth orbit using passive detectors. *Radiation Measurements*, 33(3):255–263, 2001. 10.1016/S1350-4487(01)00047-6.

[6] H. Koshiishi, H. Matsumoto, A. Chishiki, T. Goka, and T. Omodaka. Evaluation of the neutron radiation environment inside the International Space Station based on the Bonner Ball Neutron Detector experiment. *Radiation Measurements*, 42(9):1510–1520, 2007. 10.1016/j.radmeas.2007.02.072.

[7] ICRP. ICRP 103: The 2007 Recommendations of the ICRP. *Annals of the ICRP*, 37(2-4), 2007.

[8] US NRC. Units of Radiation Dose. *Code of Federal Regulations*, 10(20.1004):298–300, 2021.

[9] S. F. Kry, et al. AAPM TG 158: Measurement and calculation of doses outside the treated volume from external-beam radiation therapy. *Medical Physics*, 44(10):e391–e429, 2017. 10.1002/mp.12462.

[10] D. L. Vaux. In defense of the somatic mutation theory of cancer. *BioEssays*, 33(5): 341–343, 2011. 10.1002/bies.201100022.

[11] D. Hanahan and R. A. Weinberg. The Hallmarks of Cancer. *Cell*, 100:57–70, 2000. 10.1016/S0092-8674(00)81683-9.

[12] D. Hanahan and R. A. Weinberg. Hallmarks of cancer: The next generation. *Cell*, 144(5): 646–674, 2011. 10.1016/j.cell.2011.02.013.

[13] J. B. Little. Radiation carcinogenesis. *Carcinogenesis*, 21(3):397–404, 2000. 10.1093/carcin/21.3.397.

[14] R. Iyer and B. E. Lehnert. Effects of ionizing radiation in targeted and nontargeted cells. *Archives of Biochemistry and Biophysics*, 376(1):14–25, 2000. 10.1006/abbi.1999.1684.

[15] D. T. Goodhead. Initial events in the cellular effects of ionizing radiations: Clustered damage in DNA. *International Journal of Radiation Biology*, 65(1):7–17, 1994. 10.1080/09553009414550021.

[16] J. F. Ward. Radiation Mutagenesis : The Initial DNA Lesions Responsible. *Radiation Research*, 142(3):362–368, 1995. 10.2307/3579145.

[17] K. Magnander and K. Elmroth. Biological consequences of formation and repair of complex DNA damage. *Cancer Letters*, 327(1-2):90–96, 2012. 10.1016/j.canlet.2012.02.013.

[18] A. G. Georgakilas, P. O'Neill, and R. D. Stewart. Induction and Repair of Clustered DNA Lesions: What Do We Know So Far? *Radiation Research*, 180(1):100–109, 2013. 10.1667/rr3041.1.

[19] E. Sage and N. Shikazono. Radiation-induced clustered DNA lesions: Repair and mutagenesis. *Free Radical Biology and Medicine*, 107:125–135, 2017. 10.1016/j.freeradbiomed.2016.12.008.

[20] H. Nikjoo, S. Uehara, W. E. Wilson, M. Hoshi, and D. T. Goodhead. Track structure in radiation biology: theory and applications. *International Journal of Radiation Biology*, 73 (4):355–364, 1998.

[21] M. A. Tajik-Mansoury, H. Rajabi, and H. Mozdarani. A comparison between track-structure, condensed-history Monte Carlo simulations and MIRD cellular S-values. *Physics in Medicine and Biology*, 62(5):N90–N106, 2017. 10.1088/1361-6560/62/5/N90.

[22] S. Incerti, et al. The Geant4-DNA project. *International Journal of Modeling, Simulation, and Scientific Computing*, 1(2):157, 2010.

[23] S. Incerti, et al. Comparison of GEANT4 very low energy cross section models with experimental data in water. *Medical Physics*, 37(9):4692–4708, 2010. 10.1118/1.3476457.

[24] M. A. Bernal, et al. The influence of DNA configuration on the direct strand break yield. *Computational and Mathematical Methods in Medicine*, page 417501, 2015. 10.1155/2015/417501.

[25] S. Incerti, et al. Geant4-DNA example applications for track structure simulations in liquid water: A report from the Geant4-DNA Project. *Medical Physics*, 45(8):e722–e739, 8 2018. 10.1002/mp.13048.

[26] C. M. Lund, G. Famulari, L. Montgomery, and J. Kildea. A microdosimetric analysis of the interactions of mono-energetic neutrons with human tissue. *Physica Medica*, 73: 29–42, 2020. 10.1016/j.ejmp.2020.04.001.

[27] T. Sato, et al. Particle and heavy ion transport code system, PHITS, version 2.52. *Journal of Nuclear Science and Technology*, 50(9), 2013. 10.1080/00223131.2013.814553.

[28] W. Friedland, M. Dingfelder, P. Kundrát, and P. Jacob. Track structures, DNA targets and radiation effects in the biophysical Monte Carlo simulation code PARTRAC. *Mutation Research - Fundamental and Molecular Mechanisms of Mutagenesis*, 711(1-2):28–40, 2011. 10.1016/j.mrfmmm.2011.01.003.

[29] J. Schuemann, et al. TOPAS-nBio: An Extension to the TOPAS Simulation Toolkit for Cellular and Sub-cellular Radiobiology. *Radiation Research*, 191(2):125–138, 1 2019. 10.1667/rr15226.1.

[30] D. R. White, J. Booz, R. V. Griffith, J. J. Spokas, and I. J. Wilson. Report 44. *Journal of the International Commission on Radiation Units and Measurements*, os23(1), 1989. 10.1093/jicru/os23.1.report44.

[31] S. Incerti, M. Douglass, S. Penfold, S. Guatelli, and E. Bezak. Review of Geant4-DNA applications for micro and nanoscale simulations. *Physica Medica*, 32(10):1187–1200, 10 2016. 10.1016/j.ejmp.2016.09.007.

[32] S. Meylan, et al. Simulation of early DNA damage after the irradiation of a fibroblast cell nucleus using Geant4-DNA. *Scientific Reports*, 7:11923, 12 2017. 10.1038/s41598-017-11851-4.

[33] N. Lampe, et al. Mechanistic DNA damage simulations in Geant4-DNA Part 2: Electron and proton damage in a bacterial cell. *Physica Medica*, 48:146–155, 2018. 10.1016/j.ejmp.2017.12.008.

[34] N. Tang, et al. Influence of chromatin compaction on simulated early radiation-induced DNA damage using Geant4-DNA. *Medical Physics*, 46(3):1501–1511, 2019. 10.1002/mp.13405.

[35] A. Zabihi, et al. Determination of fast neutron RBE using a fully mechanistic computational model. *Applied Radiation and Isotopes*, 156:108952, 2020. 10.1016/j.apradiso.2019.108952.

[36] H. Zhu, et al. Cellular Response to Proton Irradiation: A Simulation Study with TOPAS-nBio. *Radiation Research*, 194(1):9–21, 2020. 10.1667/rr15531.1.

[37] D. Sakata, et al. Fully integrated Monte Carlo simulation for evaluating radiation induced DNA damage and subsequent repair using Geant4-DNA. *Scientific Reports*, 10(1):1–13, 2020. 10.1038/s41598-020-75982-x.

[38] C. Villagrasa, et al. Geant4-DNA simulation of DNA damage caused by direct and indirect radiation effects and comparison with biological data. *EPJ Web of Conferences*, 153:1–6, 2017. 10.1051/epjconf/201715304019.

[39] A. L. McNamara, et al. Geometrical structures for radiation biology research as implemented in the TOPAS-nBio toolkit. *Physics in Medicine and Biology*, 63(17):175018, 9 2018. 10.1088/1361-6560/aad8eb.

[40] J. Schuemann, et al. A New Standard DNA Damage (SDD) Data Format. *Radiation Research*, 191(1):76–92, 2019. 10.1667/rr15209.1.

[41] E. Lieberman-Aiden, et al. Comprehensive Mapping of Long-Range Interactions Reveals Folding Principles of the Human Genome. *Science*, 326(5850):289–293, 2009.

[42] S. K. Ghosh and D. Jost. How epigenome drives chromatin folding and dynamics, insights from efficient coarse-grained models of chromosomes. *PLoS Computational Biology*, 14 (5):1–26, 2018. 10.1371/journal.pcbi.1006159.

[43] L. Seaman, W. Meixner, J. Snyder, and I. Rajapakse. Periodicity of nuclear morphology in human fibroblasts. *Nucleus*, 6(5):408–416, 2015. 10.1080/19491034.2015.1095432.

[44] M. A. Śmiałek, N. C. Jones, S. V. Hoffmann, and N. J. Mason. Measuring the density of DNA films using ultraviolet-visible interferometry. *Physical Review E - Statistical, Nonlinear, and Soft Matter Physics*, 87(6):1–4, 2013. 10.1103/PhysRevE.87.060701.

[45] J. Perl, D. Hall, J. Shin, J. Schuemann, and J. Ramos-Méndez. Modular Physics Lists, 2016. https://topas.readthedocs.io/en/latest/parameters/physics/modular.html.

[46] D. E. Charlton and J. L. Humm. A method of calculating initial DNA Strand breakage following the decay of incorporated 125i. *International Journal of Radiation Biology*, 53 (3):353–365, 1988. 10.1080/09553008814552501.

[47] R. F. Martin and W. A. Haseltine. Range of Radiochemical Damage to DNA with Decay of Iodine-125. *Science*, 213(4510):896–898, 1981. 10.1126/science.7256283.

[48] H. Nikjoo, P. O'Neill, D. T. Goodhead, and M. Terrissol. Computational modelling of low-energy electron-induced DNA damage by early physical and chemical events. *International Journal of Radiation Biology*, 71(5):467–483, 1997.

[49] R. Watanabe, S. Rahmanian, and H. Nikjoo. Spectrum of Radiation-Induced Clustered Non-DSB Damage – A Monte Carlo Track Structure Modeling and Calculations. *Radiation Research*, 183(5):525–540, 2015. 10.1667/rr13902.1.

[50] M. Mokari, H. Moeini, M. Soleimani, and E. Fereidouni. Calculation and comparison of the direct and indirect DNA damage induced by low energy electrons using default and CPA100 cross section models within Geant4-DNA. *Nuclear Instruments and Methods in Physics Research, Section B: Beam Interactions with Materials and Atoms*, 480:56–66, 2020. 10.1016/j.nimb.2020.08.011.

[51] H. Nikjoo, P. O'Neill, W. E. Wilson, and D. T. Goodhead. Computational approach for determining the spectrum of DNA damage induced by ionizing radiation. *Radiation Research*, 156:577–583, 2001. 10.1667/0033-7587(2001)156[0577:cafdts]2.0.co;2.

[52] G. P. Van der Schans. Gamma-ray induced double-Strand breaks in DNA resulting from randomly-inflicted single-strand breaks: Temporal local denaturation, a new radiation phenomenon? *International Journal of Radiation Biology*, 33(2):105–120, 1978. 10.1080/09553007814550011.

[53] Joint Committee for Guides in Metrology. JCGM 100: Evaluation of measurement data — Guide to the expression of uncertainty in measurement. Technical report, Working Group 1 of the Joint Committee for Guides in Metrology, 2008.

[54] I. Shuryak, et al. Scaling human cancer risks from low LET to high LET when dose-effect relationships are complex. *Radiation Research*, 187(4):476–482, 2017. 10.1667/RR009CC.1.

[55] P. Pater, J. Seuntjens, I. El Naqa, and M. A. Bernal. On the consistency of Monte Carlo track structure DNA damage simulations. *Medical Physics*, 41(12):1–9, 2014. 10.1118/1.4901555.

[56] H. Zhu, et al. A parameter sensitivity study for simulating DNA damage after proton irradiation using TOPAS-nBio. *Physics in medicine and biology*, 65(8):085015, 2020. 10.1088/1361-6560/ab7a6b.

[57] L. Mullenders, M. Atkinson, H. Paretzke, L. Sabatier, and S. Bouffler. Assessing cancer risks of low-dose radiation. *Nature Reviews Cancer*, 9(8):596–604, 2009. 10.1038/nrc2677.

[58] R. W. Harbron. Cancer risks from low dose exposure to ionising radiation - Is the linear no-threshold model still relevant? *Radiography*, 18(1):28–33, 2012. 10.1016/j.radi.2011.07.003.

[59] W. F. Morgan and W. J. Bair. Issues in Low Dose Radiation Biology: The Controversy Continues. A Perspective. *Radiation Research*, 179(5):501–510, 2013. 10.1667/rr3306.1.

[60] S. G. Swarts, M. D. Sevilla, D. Becker, C. J. Tokar, and K. T. Wheeler. Radiation-Induced DNA Damage as a Function of Hydration. I. Release of Unaltered bases. *Radiation Research*, 129(3):333–344, 1992.

[61] Z. Nikitaki, et al. Non-DSB clustered DNA lesions. Does theory colocalize with the experiment? *Radiation Physics and Chemistry*, 128:26–35, 2016. 10.1016/j.radphyschem.2016.06.020.

[62] I. Kyriakou, S. Incerti, and Z. Francis. Technical note: Improvements in geant 4 energy-loss model and the effect on low-energy electron transport in liquid water. *Medical Physics*, 42(7):3870–3876, 2015. 10.1118/1.4921613.

[63] J. Bordes, S. Incerti, N. Lampe, M. Bardiès, and M. C. Bordage. Low-energy electron dose-point kernel simulations using new physics models implemented in Geant4-DNA. *Nuclear Instruments and Methods in Physics Research, Section B: Beam Interactions with Materials and Atoms*, 398:13–20, 2017. 10.1016/j.nimb.2017.02.044.

[64] W. Friedland, P. Jacob, and P. Kundrát. Stochastic simulation of DNA double-strand break repair by non-homologous end joining based on track structure calculations. *Radiation Research*, 173(5):677–688, 2010. 10.1667/RR1965.1.

[65] S. J. McMahon, J. Schuemann, H. Paganetti, and K. M. Prise. Mechanistic Modelling of DNA Repair and Cellular Survival Following Radiation-Induced DNA Damage. *Scientific Reports*, 6:1–14, 2016. 10.1038/srep33290.

[66] J. Perl, J. Shin, J. Schümann, B. Faddegon, and H. Paganetti. TOPAS: An innovative proton Monte Carlo platform for research and clinical applications. *Medical Physics*, 39 (11):6818–6837, 2012. 10.1118/1.4758060.

[67] B. Faddegon, et al. The TOPAS tool for particle simulation, a Monte Carlo simulation tool for physics, biology and clinical research. *Physica Medica*, 72:114–121, 2020. 10.1016/j.ejmp.2020.03.019.

[68] L. Montgomery, C. M. Lund, J. Manalad, A. Landry, and J. Kildea. TOPAS Clustered DNA Damage, 2021. https://doi.org/10.5281/zenodo.5090104.

[69] J. D. Hunter. Matplotlib: A 2D graphics environment. *Computing in Science and Engineering*, 9(3):90–95, 2007. 10.1109/MCSE.2007.55.

Chapter 9

Summary, conclusion, and future work

9.1 Summary

The secondary neutrons produced during high-energy ($\gtrsim 8$ MeV) radiation therapy pose a risk to cancer patients for the induction of an iatrogenic second cancer. This carcinogenic risk is becoming increasingly relevant as the long-term survival rates of cancer patients continue to improve due to advancements in both the diagnosis and the treatment of cancer. The carcinogenic risk associated with neutrons is known to be highly-energy dependent, as evidenced by radiation protection quantities such as the ICRP's neutron weighting factors [1] and the US NRC's neutron quality factors [2]. However, a fundamental biophysical model of the cause of this energy dependence has previously been lacking. A recent publication by Baiocco et al. [3] made important contributions towards explaining this energy dependence by using TSMC methods to analyze neutron-induced DNA damage. However, there were limitations in the scope and transparency of their method that warranted follow-up investigation.

In consideration of the above discussion, advancement in our understanding of the carcinogenic risk posed to radiation therapy patients by secondary neutrons requires the following:

1. An efficient and accurate method to measure the spectrum of secondary neutrons in order to assess spectral changes due to variations in radiation treatment parameters.

2. An understanding of the biophysical mechanisms that give rise to the energy dependence of neutron RBE for stochastic effects.

The goal of this thesis was thus to advance our understanding of the carcinogenic risk that is posed to radiation therapy patients by secondary neutrons through the measurement of neutron

spectra and the development of a model to explain the energy dependence of their carcinogenic effects.

9.1.1 Advancements in the measurement of neutron spectra

Part I of this thesis covered a variety of topics pertaining to the measurement of neutron spectra in radiation therapy. Chapter 2 provided a summary of the radiation interaction mechanisms, physical quantities, and dosimetric concepts that were relevant to the scope of this thesis. In Chapter 3, an overview of neutron detectors was presented with a focus on the BSS [4] and NNS [5] neutron spectrometers and their applications in radiation therapy. The NNS is a user-friendly, efficient, and active neutron spectrometer that was previously validated for use in radiation therapy by our research group [6, 7]. In this thesis, we sought to demonstrate the ability to use the NNS in a clinically-relevant study and to reduce subjective user-input when unfolding NNS measurements.

Chapter 4 contained our published manuscript that described how we used the NNS to measure and compare the neutron spectra produced by the clinically-commissioned 10 MV FFF and 10 MV beams of a Varian TrueBeam linac. Previously published studies that used passive BSS systems [8, 9] identified that photoneutron production for higher energy beams could be reduced by up to $\sim$70% when the flattening filter was experimentally removed. However, the current trend in EBRT is to use lower energy beams and, prior to our publication, there was a lack of data on photoneutron production at 10 MV using a clinical-commissioned FFF beam. We determined that a 30–40% reduction in photoneutron fluence per MU could be obtained by using the 10 MV FFF beam compared to the 10 MV beam. While treatment plans using 10 MV FFF beams tend to involve on the order of 10% more MUs than those using 10 MV beams [10], our results show that a net reduction in photoneutron exposure to the patient can be achieved with 10 MV FFF beams. Additionally, we found it instructive to analyze neutron production per electron striking the bremsstrahlung target of the linac. This analysis allowed us to assess the primary cause of the reduction in photoneutron production per MU for FFF beams. We found that the primary cause of the reduction was a large decrease in the number of source electrons required per MU rather than the removal of a source of neutrons in the flattening filter itself.

Chapter 5 contained another of our published manuscripts. This manuscript described a novel stopping criterion that we developed for our iterative MLEM algorithm that we use to

unfold NNS measurements. In our previous studies with the NNS, we identified the lack of an objective stopping criterion for our MLEM algorithm as an important source of subjectivity in the unfolding process. To address this issue, we developed a novel stopping criterion that terminates the unfolding process at an optimal number of iterations after sufficient solution convergence but prior to notable accumulation of noise in the spectrum without requiring user input. We validated our stopping criterion by using it to unfold neutron spectra produced by radiation therapy beams of varying energies and particle types and comparing the results with spectra obtained using empirical upper and lower limits on the number of MLEM iterations. Overall, this study led to an increased confidence in the neutron spectra that we can measure with the NNS by eliminating intra-user and inter-user variations. This stopping criterion has been used in two subsequent publications by our research group [7, 11]

9.1.2 Advancements in modeling the energy dependence of neutron carcinogenic risk

In Part II of this thesis, the focus of our work shifted from neutron spectral measurements to modeling the energy dependence of neutron-induced carcinogenic effects. Chapter 6 contained an overview of key biological and radiobiological concepts, such as the structure of human nuclear DNA, the mechanisms of carcinogenesis, and the pathways of radiation-induced carcinogenesis. The chapter concluded with a discussion of clustered DNA damage lesions, which are widely believed to be the primary initiating event for radiation-induced mutagenesis and subsequent carcinogenesis. Chapter 7 summarized the MC method as applied to radiation transport with a focus on how TSMC techniques can be used to model radiobiological effects like DNA damage. Chapter 7 concluded with a review of recently published MC studies designed to model the energy dependence of neutron RBE.

Finally, Chapter 8 contained our submitted manuscript that describes our efforts to model the energy dependence of neutron RBE for stochastic effects by using TSMC simulations of clustered DNA damage. In this study, we developed a TSMC application using the TOPAS-nBio framework [12] that contained a custom nuclear DNA model as well as a novel algorithm for scoring both complex DSB clusters and non-DSB clusters. We used the spectra of secondary particles produced by neutrons and x-rays in human tissue (as determined in a previous study by our research group [13]) to irradiate our nuclear DNA model. We plotted the resulting neutron RBE for inducing both types of clustered DNA damage and found qualitative agreement with

both the neutron w_R and the neutron Q factors. Additionally, we identified a significant energy dependence in the average length and complexity of clustered DNA damage, thereby affirming that these parameters should be considered when modeling neutron-induced carcinogenic effects. As is necessitated for all Monte Carlo studies, this study involved a number of modeling assumptions. Therefore, we assessed the validity of these assumptions by repeating our simulations with variations in several key simulation parameters. We found that our results were qualitatively consistent in all cases and that quantitative differences could be explained from first principles. Overall, our study provided evidence to support the hypothesis that many types of clustered DNA damage contribute to the energy dependence of neutron RBE for stochastic effects.

9.2 Conclusion

The body of work described in this thesis represents advancements in our understanding of the carcinogenic risk posed by secondary neutrons to radiation therapy patients. We have demonstrated that the NNS and our MLEM unfolding methodology are both effective and reliable for measuring and comparing the neutron spectra produced in clinically-relevant radiation therapy scenarios. Additionally, we have developed a fundamental model using TSMC methods to explain the energy dependence of neutron RBE for stochastic effects. In achieving these deliverables, we have contributed our novel MLEM algorithm [14] and TSMC application [15] to the scientific community under open-source licenses. It is our hope that these contributions benefit other researchers aiming to expand this area of research or build on our work.

9.3 Future work

Our research group continues to use the NNS to analyze neutron spectra produced in clinical scenarios of interest. For example, we have recently used the NNS to conduct a thorough investigation of the impact of treatment parameter variation on the production of electroneutron spectra [11].

Our TSMC application [15] is currently being expanded to account for the indirect effects of radiation action on DNA. A follow-up manuscript to the one described in Chapter 8 is envisaged and we will assess the relative contributions of direct and and indirect effects to neutron RBE

for clustered DNA damage. Additionally, we intend to incorporate DNA repair modeling into our TSMC application in order to bridge the gap between DNA damage and mutagenic effects.

Finally, our research group is presently conducting experiments using single-cell whole-genome sequencing to assess the spectrum of mutations induced by radiation in human cell cultures. Eventually, we aim to use this technique to experimentally determine neutron RBE for mutagenic effects and compare with our computational results.

Overall, we hope that our past, present, and future research will enable clinicians and patients to better understand the carcinogenic risk associated with secondary neutrons when prescribing radiation treatment.

References

[1] ICRP. ICRP 103: The 2007 Recommendations of the ICRP. *Annals of the ICRP*, 37(2-4), 2007.

[2] US NRC. Units of Radiation Dose. *Code of Federal Regulations*, 10(20.1004):298–300, 2021.

[3] G. Baiocco, et al. The origin of neutron biological effectiveness as a function of energy. *Scientific Reports*, 6:34033, 2016. 10.1038/srep34033.

[4] R. L. Bramblett, R. I. Ewing, and T. W. Bonner. A new type of neutron spectrometer. *Nuclear Instruments and Methods*, 9(1):1–12, 1960. 10.1016/0029-554X(60)90043-4.

[5] J. Dubeau, S. S. Hakmana Witharana, J. Atanackovic, A. Yonkeu, and J. P. Archambault. A neutron spectrometer using nested moderators. *Radiation Protection Dosimetry*, 150(2): 217–222, 2012. 10.1093/rpd/ncr381.

[6] R. Maglieri, A. Licea, M. Evans, J. Seuntjens, and J. Kildea. Measuring neutron spectra in radiotherapy using the nested neutron spectrometer. *Medical Physics*, 42(11):6162–6169, 2015. 10.1118/1.4931963.

[7] F. Mathew, C. Chilian, L. Montgomery, and J. Kildea. Development of a passive gold-foil Nested Neutron Spectrometer to validate the active current-mode He-3 measurements in a high neutron fluence rate radiotherapy environment. *Nuclear Instruments and Methods*

in Physics Research, Section A: Accelerators, Spectrometers, Detectors and Associated Equipment, 985:164662, 2021. 10.1016/j.nima.2020.164662.

[8] S. F. Kry, et al. Reduced Neutron Production Through Use of a Flattening-Filter-Free Accelerator. *International Journal of Radiation Oncology Biology Physics*, 68(4):1260–1264, 2007. 10.1016/j.ijrobp.2007.04.002.

[9] S. F. Kry, et al. Energy spectra, sources, and shielding considerations for neutrons generated by a flattening filter-free Clinac. *Medical Physics*, 35(5):1906–1911, 2008. 10.1118/1.2905029.

[10] J. B. Chung, et al. Comparison of VMAT-SABR treatment plans with flattening filter (FF) and flattening filter-free (FFF) beam for localized prostate cancer. *Journal of Applied Clinical Medical Physics*, 16(6):302–313, 2015. 10.1120/jacmp.v16i6.5728.

[11] F. Mathew, G. A. Makdessi, L. Montgomery, M. Evans, and J. Kildea. The impact of treatment parameter variation on secondary neutron spectra in high-energy electron beam radiotherapy. *Physica Medica*, 80:125–133, 2020. 10.1016/j.ejmp.2020.10.016.

[12] J. Schuemann, et al. A New Standard DNA Damage (SDD) Data Format. *Radiation Research*, 191(1):76–92, 2019. 10.1667/rr15209.1.

[13] C. M. Lund, G. Famulari, L. Montgomery, and J. Kildea. A microdosimetric analysis of the interactions of mono-energetic neutrons with human tissue. *Physica Medica*, 73: 29–42, 2020. 10.1016/j.ejmp.2020.04.001.

[14] L. Montgomery, G. Al Makdessi, R. Maglieri, F. Mathew, and J. Kildea. Neutron Spectrometry, 2020. http://doi.org/10.5281/zenodo.3610493.

[15] L. Montgomery, C. M. Lund, J. Manalad, A. Landry, and J. Kildea. TOPAS Clustered DNA Damage, 2021. https://doi.org/10.5281/zenodo.5090104.